

UNCLASSIFIED

AD 274 159

*Reproduced
by the*

ARMED SERVICES TECHNICAL INFORMATION AGENCY
ARLINGTON HALL STATION
ARLINGTON 12, VIRGINIA



UNCLASSIFIED

NOTICE: When government or other drawings, specifications or other data are used for any purpose other than in connection with a definitely related government procurement operation, the U. S. Government thereby incurs no responsibility, nor any obligation whatsoever; and the fact that the Government may have formulated, furnished, or in any way supplied the said drawings, specifications, or other data is not to be regarded by implication or otherwise as in any manner licensing the holder or any other person or corporation, or conveying any rights or permission to manufacture, use or sell any patented invention that may in any way be related thereto.

CATALOGED BY ASTIA

AD NO.

274159

274 159

ASTIA
RECEIVED
APR 17 1962
TISA

KELLETT



Aircraft

CORPORATION

KELLETT

Aircraft
CORPORATION

ON THE
AERODYNAMIC DESIGN OF PROPELLERS
AND
DUCT SYSTEMS FOR GROUND EFFECT VEHICLES

DATE 1-15-1962 REPORT NO. 208A90-1

PREPARED

Richard R. Fruyn

Richard R. Fruyn

A. A. Perlmutter

A. A. Perlmutter

N. Miller

N. Miller

APPROVED

L. Goland

L. Goland

NO. OF PAGES

ABSTRACT

Analytical and experimental studies have been made to establish a method for the design of propellers and duct systems for annular jet ground effect machines. Propeller and inlet geometry and the effects of nozzle velocity distribution on annular jet performance were analyzed. Experimental investigations included tests of an axisymmetric duct and a curved duct at various ground board heights and inclinations. Overall and the detailed internal efficiencies were determined and are compared with the analysis.

FOREWORD

This is the final report of a research program to establish methods of aerodynamic design of propellers and duct systems for ground effect vehicles. The investigation was performed by Kellett Aircraft Corporation for the Princeton University Department of Aeronautical Engineering under Subcontract No. 1 of U. S. Army TRECOM Contract No. DA 44-177-TC-524. The Princeton Project Engineer was Mr. Mark Knowlton whose assistance is hereby gratefully acknowledged. The Kellett Project Engineer was Mr. Richard R. Fruyn, Head, Aerodynamics Section. The theoretical work was performed by Dr. A. A. Perlmutter, Manager of Research Engineering. Mr. Nelson Miller and Mr. Lawrence Butler, Aerodynamicists, were responsible for the successful completion of the test phase of the program.

The authors wish to thank Mr. Leonard Goland for technical guidance during the execution of this work.

TABLE OF CONTENTS

	Page
ABSTRACT	ii
FOREWORD	iii
TABLE OF CONTENTS	iv
LIST OF ILLUSTRATIONS	vii
LIST OF TABLES	xi
LIST OF SYMBOLS	xii
SUMMARY	xv
INTRODUCTION	1
1.0 PERFORMANCE ANALYSES	3
1.1 INTRODUCTION	3
1.2 DIMENSIONAL ANALYSES	3
1.3 DETERMINATION OF PROPELLER THRUST	5
1.4 DETERMINATION OF PROPELLER POWER	11
1.5 DUCT EFFICIENCY	12
1.6 EFFECT OF INLET RING	13
1.6.1 Operation in Ground Effect	13
1.6.2 Operation Out of Ground Effect	14
1.6.3 Analytical Determination of T_s/T_p Out of Ground Effect	14
1.7 DETERMINATION OF BASE PRESSURE	16
1.8 EFFECT OF NOZZLE VELOCITY DISTRIBUTION ON LIFT TO POWER RATIO	16
2.0 TEST RESULTS	

	Page
2.1 OVERALL PERFORMANCE	20
2.1.1 Performance as a Function of Height-Diameter Ratio	20
2.1.1.1 Straight Duct	20
2.1.1.2 Curved Duct	22
2.1.2 Effect of Detail Geometry Modifications on Performance	23
2.1.2.1 Inlet Geometry	23
2.1.2.2 Internal Modifications to Curved Duct	24
2.1.3 Performance with Pitch or Roll Inclination of Annular Jet	24
2.1.3.1 Straight Duct	24
2.1.3.2 Curved Duct	25
2.1.3.3 Control Plug in Curved Duct	25
2.1.4 Overall Internal Efficiency	25
2.2 PROPELLER DATA	26
2.2.1 Thrust	26
2.2.2 Power	26
2.2.3 Flow Conditions at the Propeller	27
2.2.4 Propeller Efficiency	29
2.3 DUCT PERFORMANCE	30
2.3.1 Flow Field Data	30
2.3.2 Duct Efficiency	31
2.3.2.1 Inlet Performance	33

	Page
2.4 ANNULAR JET PERFORMANCE	36
2.4.1 Base Pressure Recovery	36
2.4.2 Nozzle Pressure	37
2.4.3 Augmentation Ratio	37
3.0 CORRELATION OF ANALYTICAL METHODS WITH TEST RESULTS	38
3.1 PROPELLER PERFORMANCE	38
3.2 DUCT EFFICIENCY	39
3.2.1 Duct Losses	39
3.2.2 Inlet Ring Performance	40
4.0 METHOD OF DESIGN OF PROPELLER AND DUCT SYSTEMS	41
4.1 ANNULAR JET PARAMETERS	42
4.2 DUCT DESIGN	44
4.3 PROPELLER DESIGN	45
APPENDIX: THE TEST PROGRAM	47
REFERENCES	57
TABLES	59
FIGURES	66

LIST OF ILLUSTRATIONS

FIGURE		PAGE
1	Notation Used In the Analysis of the Annular Jet	66
2	Notation for Inlet Geometry	67
3	Notation for Nozzle Geometry	68
4	Definition of Velocity Notation	69
5	Lift Performance of an Annular Jet as Effected by Nozzle Velocity Distribution at Constant Power	70
6	Performance of Various Straight Duct Test Configurations at Constant Propeller Disc Loading	71
7	Performance of Straight Duct Test Unit With Comparative Calculated Performance	72
8	Performance of Curved Duct Configurations With Comparative Straight Duct Data and Data from Reference 7	73
9	Performance of Straight Duct Test Unit With Various Inlet Configurations	74
10	Performance of Curved Duct Test Unit With Various Internal Modifications	75
11	Performance of the Straight Duct When Inclined to the Ground	76
12	Performance of the Curved Duct When Inclined to Ground	77
13	Effect of Control Plug on Performance of Curved Duct	78
14	Change in Center of Pressure of the Annular Jet Due To A Control Plug in the Nozzle For the Curved Duct	79

FIGURE		PAGE
15	Overall Internal Efficiency of Various Straight and Curved Duct Configurations	80
16	Propeller Thrust Coefficient for Straight and Curved Duct Configurations	81
17	Propeller Power Coefficient for Straight and Curved Duct Configurations	82
18	Velocities Before and After the Propeller for the Straight Duct Out of Ground Effect	83
19	Comparison of the Velocity at the Propeller Indicated by Various Measurements	84
20	Typical Flow Swirl Data for Straight Duct Test Unit With 4.5 Inch Inlet Ring	85
21	Isolated Propeller Efficiency Based on Nozzle Pressure Measurements for Curved And Straight Duct Configurations	86
22	Inlet Flow Field For Straight Duct With 4.5 Inch Inlet Ring, Out of Ground Effect	87
23	Typical Flow Measurements for Short Straight Duct at Two Ground Board Heights with The 4.5 Inch Inlet Ring	88
24	Polar Plot of Total and Static Pressures at the Annular Jet Nozzle of the Curved Duct at an h/D of 0.161	89
25	Efficiency of the Duct System For The Curved and Straight Duct Configurations	90
26	Total Pressure Data at two Stations Behind the Propeller for the Curved and Straight Duct Configurations	91
27	Static Pressure on Inlet Ring With Straight Duct, Out of Ground Effect	92

FIGURE		PAGE
28	Static Pressure on Inlet Nose With Straight Duct, Out of Ground Effect	93
29	Static and Total Pressures at Mid Length of the Long Inlet on the Straight Duct	94
30	Inlet Ring Thrust As Affected By Inlet Ring Area Based on Data From Shrouded Propeller Literature With Theoretically Predicted Curve	95
31	Influence of Nozzle Height on Inlet Ring Thrust for Curved and Straight Duct Configurations	96
32	Static Pressure Distribution On a 4.5 Inch Inlet Ring With Curved Duct	97
33	Comparison of Base Pressure to Nozzle Total Pressure Ratio Test Data with Theoretical Prediction	98
34	Annular Jet Nozzle Static Pressure to Nozzle Total Pressure Ratio Data for the Curved and Straight Duct Configuration	99
35	Annular Jet Nozzle Static Pressure to Base Pressure Ratio for the Curved and Straight Duct Configurations	100
36	Augmentation Ratio Data with Comparative Referenced Data	101
37	Comparison of Theoretical and Experimental Propeller Thrust Data	102
38	Comparison of Theoretical and Experimental Propeller Power Data	103
39	Propeller Blade Tip Angle of Attack for the Curved and Straight Duct Configurations	104
40	Loss Factor, k_2 for the Curved and Straight Ducts	105
41	Calculated Internal Efficiency of the Curved and Straight Duct Test Units Based on Theory of Reference 6	106

FIGURE		PAGE
42	Extrapolation of Nozzle and Base Pressure Test Data to Show the Effect of Nozzle-Base Area Ratio on Annular Jet Performance	107
43	Short Straight Duct Configuration with 4.5 Inch Diameter Inlet Ring	108
44	Short Duct with Long Inlet, 4.5 Inch Inlet Ring	109
45	Short Duct with Nozzle Extension Duct, 4.5 Inch Inlet Ring	109
46	Curved Duct and Inlet Ring Geometry	110
47	Short Straight Duct with 1.5 Inch Inlet Ring	111
48	Short Straight Duct with 4.5 Inch Inlet Ring	112
49	Short Straight Duct with Quarter Elliptic Inlet Ring	113
50	Curved Duct with 4.5 Inch Inlet Ring	114
51	Definition of Curved Duct Geometric Parameters	115
52	Curved Duct with Guide Vane Installed	116
53	Curved Duct with Plenum Chamber, Inlet View	117
54	Curved Duct with Plenum Chamber and Ground Board, Base View	117
55	Probe Rake Calibration with Angle of Yaw For 6 Tube Rake	118
56	Variation of Indicated Dynamic Pressure With Actual Dynamic Pressure for 6 Tube Rake	119
57	Comparison of Summation of Individual Thrusts With Total Force vs h/D for the Curved and Straight Duct Configurations	120 121

LIST OF TABLES

TABLE		PAGE
1	Propeller Characteristics	59
2	Co-ordinates of the Quarter Elliptic Inlet Ring	60
3	Gem-Duct-Test Unit Geometric Parameters	61
4	Radius of Sections of the Outer Wall and the Centerbody of the Curved Duct	62
5	Co-ordinates of the Elliptical Center line of the Centerbody of the Curved Duct	63
6	Summary of Configurations and Tests Performed	64

LIST OF SYMBOLS

a	Slope of Lift Curve, Per Degree
A	Cross Sectional Area, Square Feet
A_s	Projected Frontal Area of Inlet Ring, Square Feet
AHP	Jet Air Horsepower
b	Number of Propeller Blades
C	Propeller Blade Chord, Feet
C_T	Propeller Thrust Coefficient = $\frac{T_P}{\pi R^2 \rho (\Omega R)^2}$
C_P	Propeller Power Coefficient = $\frac{P}{\pi R^2 \rho (\Omega R)^3}$
D	Planform Diameter, Feet
F	Volume Flow, Cubic Feet/Second
G_{eff}	Ground Effect Power Factor, $G_{eff} = \frac{P_i q_i}{L^{3/2} \sqrt{\rho S}}$
h	Nozzle Height Above the Ground Plane, feet
HP	Input Shaft Horsepower
k_2	Dynamic Pressure Duct Loss Factor
k_s	Inlet Ring Pressure Factor
l_D	Duct Length, Feet
L	Total Lift, Pounds
m	Mass Flow, Slugs/Second
P	Power, foot-pounds/second
P	Pressure, pound/square feet
Q	Propeller Torque, foot-pounds

q	Dynamic Pressure, pound/square feet, $q = \frac{1}{2} \rho V^2$
R	Propeller Radius, feet
r	Radial Distance From Center Line of Rotation, feet
r_s	Inlet Ring Radius, inches
R_j	Turning Radius of Jet, feet
S	Planform Area, square feet
t_e	Nozzle Thickness, feet
T_j	Momentum Thrust of Jet, pounds
T_p	Propeller Thrust, pounds
T_s	Inlet Ring Thrust, pounds
V	Velocity, feet/second
V_A	Constant Velocity Across Nozzle, feet/second
V_o	See Equation (1.8-3)
X	Radial Distance Parameter, r/R
X_H	Ratio of Propeller Hub Radius to Propeller Radius
y	Radial Distance From Duct Wall, feet
Z	Overall Power Factor
α_{tip}	Propeller Blade Tip Angle of Attack, degrees
$\delta_o, \delta_1, \delta_2$	Coefficients in Power Series Expressing Profile Drag as a Function of Angle of Attack
ϵ	Propeller Swirl Angle, degrees
η_o	Duct Efficiency, percent
η_i	Internal Efficiency, percent
η_p	Isolated Propeller Efficiency, percent

θ_p	Propeller Blade Pitch, degrees
θ_l	Propeller Linear Blade Twist, degrees
θ_n	Inlet Nose Angle, degrees
θ_s	Inlet Ring Angle, degrees
θ_d	Duct Turning Angle, degrees
ρ	Air Mass Density, slugs/cubic feet
ρ_0	Standard Air Density at Sea Level (= .002378), slugs/cubic feet
ψ	Azimuth Angle (See Figure 50), degrees
σ	Propeller Solidity,
ψ_{plug}	Control Plug Azimuth Position, degrees
Ω	Propeller Rotational Speed, radians/second

Subscript

t	Total Pressure
j	Jet in Nozzle
b	Base
①	Directly Behind Propeller Plane
i	Inlet (In Front of Propeller)
p	Propeller Plane

Note:

1. All pressure terms referring to total pressure contain the subscript, t , followed by a subscript defining where pressure was measured.
2. All pressure terms referring to static pressure contain a single subscript.

SUMMARY

An analytical and experimental investigation has been performed to establish design methods for propeller and duct systems operating in ground effect. Methods are formulated for the calculation of propeller-in-duct performance. A simple analysis is made of the effect of exit nozzle velocity distribution and it is found that a constant nozzle velocity results in a maximum lift to power ratio. A qualitative analysis is made also of the duct efficiency. The similarity parameters of ground effect machines are determined.

In the experimental program the effect of various geometric and operational parameters on the internal performance of propeller-duct systems in the proximity of the ground were studied. Maximum overall internal efficiencies of 78 percent for an axially symmetric ducting system and 68 percent for a curved duct system were obtained.

INTRODUCTION

The potential of Ground Effect Vehicles for various phases of transportation has resulted in increasing activity in the fields of research and development of these machines. Early expectations of large increases of gross weight to power ratios were somewhat disappointed, especially due to the poor internal efficiencies of the existing research vehicles. The present program was undertaken to study the parameters that affect the internal efficiency with a view of providing design methods for machines with improved performance characteristics.

The aerodynamics of Ground Effect Machines can be divided into four basic areas:

1. Air Intake
2. Air Propulsion
3. Internal Ducting
4. Air Exhaust and Base Pressure

The major analytical and experimental effort to date has been concentrated on the last area, and specifically on the determination of the base pressure. The present program, on the other hand, was designed to further the state of the art in the first three of the above areas. Both experimental and analytical work was performed and the results of this work are reported herein.

Two basic configurations were investigated:

1. A straight axially symmetric duct
2. A 90 degree curved duct

Because of its relative analytical simplicity the straight duct was the first subject of investigation. Both geometric and operating parameters were studied and methods for predicting the performance of a propeller-duct combination in ground effect were formulated. Next, the effect of duct curvature on the internal efficiency was determined and a number of interesting results were obtained.

Both duct configurations had large nozzle area to total base area ratios. The reason for this choice was dictated by the desire to simulate the duct system that should be used for GEMs designed to operate at large values of h/D .

This report is divided into four sections and has one appendix.

Section 1 presents the analytical methods formulated during this program.

Section 2 discusses the test results of the experimental part of this program.

In Section 3 the test data are correlated with the analytical methods. The next section deals with a method for the design of propellers and duct systems for annular jet GEMs.

The test program and a description of the instrumentation used as well as their accuracy is described in the appendix.

1.0 PERFORMANCE ANALYSES

1.1 INTRODUCTION

The performance analyses presently in existence deal mainly with the prediction of the vehicle base pressure based on known flow characteristics of the jet efflux. The required power of the entire vehicle is then obtained by multiplying the jet efflux air power by a loss factor. There is a dearth of data on the evaluation of this loss factor which depends on vehicle design, as well as operating parameters. The purpose of the present program was to increase the knowledge on the parameters affecting this loss factor by suitable tests and to formulate methods for the determination of the internal flow characteristics of annular jet GEMs. The resultant methods are shown to be capable of providing information on the propeller, inlet and ducting geometry requirements.

This section presents the results of the analytical endeavor of this program. The following items are presented:

- 1.2 Dimensional Analysis
- 1.3 Determination of Propeller Thrust
- 1.4 Determination of Propeller Power
- 1.5 Duct Efficiency
- 1.6 Effect of Inlet Ring
- 1.7 Determination of Base Pressure
- 1.8 Effect of Nozzle Velocity Distribution

1.2 DIMENSIONAL ANALYSIS

The formulation of generalized analytical methods of predicting the performance characteristics of annular jet ground effect vehicles requires that the significant non-dimensional parameters be isolated. The determination of these parameters is achieved by a standard dimensional analysis.

The physical parameters affecting performance are:

Duct Inlet

- a. Inlet ring radius, r_s , or projected planform area of the inlet ring, A_s

- b. Thrust, T_s

Propeller

- a. Area, A_p
 b. Thrust, T_p
 c. Rotational Speed, Ω
 d. Blade Pitch, θ_p
 e. Solidity, σ

Duct

- a. Length, l_D
 b. Total Pressure, P_{tj}
 c. Static Pressure, P_j
 d. Curvature, θ_D

Base

- a. Area, A_b
 b. Pressure, P_b

Air Curtain

- a. Curtain Area, $\pi D h$

The effects of the parameters, θ_p , Ω , and σ on the propeller performance will be substantially the same as on unducted propellers. These parameters also effect the nozzle velocity distribution which is the subject of an analysis in Section 1.8. The effects of the duct parameters, l_D , and θ_D are examined in Section 1.5. The exponents of the dimensions of all other parameters in terms of length, L , time, T , and force, F , are:

	P_b	A_s	A_p	T_p	A_j	P_{tj}	P_j	A_b	$\pi D h$	T_s
L	-2	2	2	0	2	-2	-2	2	2	0
T	0	0	0	0	0	0	0	0	0	0
F	1	0	0	1	0	1	1	0	0	1

The base pressure, P_b , is given by

$$P_b = A_s^{\alpha_1} A_p^{\alpha_2} T_p^{\alpha_3} A_j^{\alpha_4} P_{tj}^{\alpha_5} P_j^{\alpha_6} A_b^{\alpha_7} (\pi D h)^{\alpha_8} T_s^{\alpha_9} \quad (1.2-1)$$

Equating the exponents of the dimensions of the factors in equation (1.2-1), and solving the resulting equations, there results that

$$P_b = P_{tj} f \left[\frac{A_s}{A_p}, \frac{T_s}{T_p}, \frac{T_p}{P_{tj} A_j}, \frac{A_j}{A_p}, \frac{P_j}{P_{tj}}, \frac{A_j}{A_b}, \frac{\pi D h}{A_j} \right] \quad (1.2-2)$$

where $f[\]$ denotes a function of $\frac{A_s}{A_p}$, $\frac{T_s}{T_p}$, etc.

The non-dimensional similarity parameters that affect the base pressure are those given in the bracket of equation (1.2-2) as well as any combination of these parameters.

It should be noted that the parameter, $\pi D h / A_j$, is particularly important in GEM internal performance analysis. This parameter is the ratio of the vertical projected area over which the annular jet must provide a seal and the area of the annular jet nozzles. As will be shown in Section 2, this parameter provides for correlation of internal flow pressures, thrust and power data for significantly different configurations. For configurations which have t_e/R values which are small as compared with t_e/h , this parameter is equal to t_e/h .

1.3 DETERMINATION OF PROPELLER THRUST

Experience with rotary wing performance analysis has shown that the rather simple combined blade element-momentum method for determining the rotor thrust results in reasonably accurate predictions of the actual thrust. As will be shown in Section 3, a similar method is also applicable for the propeller-in-duct configuration when operating in or out of ground effect. This method, which is presented here, requires, however, some empirical inputs. Two analyses are presented, the first of which assumes the velocity at the

propeller is uniform and the second in which it is assumed that the velocity varies with radius.

Referring to Figure 1 and using the momentum relationship,

$$T_P + T_S = T_P \left(1 + \frac{T_S}{T_P}\right) = \int_{A_P} (P_\infty + 2q_\infty) dA_P \quad (1.3-1)$$

Solving equation (1.3-1) for q_∞ ,

$$\int_{A_P} q_\infty dA_P = \frac{1}{2} \left\{ T_P \left(1 + \frac{T_S}{T_P}\right) - \int_{A_P} P_\infty dA_P \right\} \quad (1.3-2)$$

First consider the case where the velocity is considered constant across the propeller area, equation (1.3-2) reduces to

$$V_P = \sqrt{\frac{2}{\rho} q_\infty} = \sqrt{\frac{T_P}{\rho A_P} \left(1 + \frac{T_S}{T_P} - \frac{P_\infty}{T_P} \frac{A_P}{A_P}\right)} \quad (1.3-3)$$

The propeller thrust coefficient is defined as

$$C_T = \frac{T_P}{\rho A_P (\Omega R)^2} \quad (1.3-4)$$

Introducing equation (1.3-4) into equation (1.3-3),

$$\frac{V_P}{\Omega R} = \sqrt{C_T \left(1 + \frac{T_S}{T_P} - \frac{P_\infty}{T_P} \frac{A_P}{A_P}\right)} \quad (1.3-5)$$

From blade element considerations,

$$\frac{2 C_T}{\sigma} = \frac{1}{1 - \chi_H^2} \int_{\chi_H}^1 \left(\theta_P x^2 - \frac{V_P}{\Omega R} x \right) dx \quad (1.3-6)$$

Integrating equation (1.3-6) and solving for C_T , there results

$$C_T = \left\{ -\frac{A}{2} + \sqrt{\left(\frac{A}{2}\right)^2 + B} \right\}^2 \quad (1.3-7)$$

where

$$\left. \begin{aligned} A &= \frac{a\sigma}{4} \left\{ 1 + \frac{T_s}{T_p} - \frac{P_0}{T_p} \frac{1}{A_p} \right\}^{1/2} \\ B &= \frac{\Theta_p (1 - X_H^3)}{\frac{6}{a\sigma} (1 - X_H^2)} \end{aligned} \right\} \quad (1.3-8)$$

The propeller thrust coefficient, C_T , can now be determined if the quantities T_s/T_p and $P_0/T_p \frac{1}{A_p}$ are known. As will be pointed out in Section 2, in the proximity of the ground the ground effect is more important for the determination of T_s/T_p than is the inlet ring geometry. It follows, that in ground effect it may be assumed that the inlet ring area and shape is such that the inlet ring thrust can also be predicted by use of a momentum relation. Out of ground effect, this assumption is not valid and the dependency of T_s/T_p on the inlet geometry must be determined in another manner. Thus, in ground effect,

$$T_s = P_i A_i + 2 \rho g_i A_i \quad (1.3-9)$$

$$\left. \begin{aligned} \text{Since } g_i &= g_0 = -P_i \\ T_p &= A_p(P_0 - P_i) \end{aligned} \right\} \quad (1.3-10)$$

it follows that

$$P_0 / \frac{T_p}{A_p} = 1 - \left(\frac{T_s}{T_p} \right) \left(\frac{A_p}{A_i} \right) \quad (1.3-11)$$

Introducing Equation (1.3-11) into the term A from Equation (1.3-8),

$$A = \frac{a\sigma}{4} \sqrt{\frac{T_s}{T_p} \left(1 + \frac{A_p}{A_i} \right)} \quad (1.3-12)$$

The determination of T_s/T_p is discussed in Section 1.6 and a comparison between the theory and experimental data is presented in Section 3.

Out of ground effect the thrust coefficient is given by Equation (1.3-7) with

$$A = \frac{a\sigma}{4} \sqrt{1 + \left(\frac{T_s}{T_p} \right)_\infty} \quad (1.3-13)$$

where the value of $\left(\frac{T_s}{T_p} \right)_\infty$ is obtained as discussed in Section 1.6.

For the case in which the radial velocity distribution across the propeller blade, as well as propeller twist and taper, are to be accounted for, the analysis proceeds as described in the following.

From annular momentum considerations

$$dT_s + dT_p = 2\pi R^2 \left[\rho V_p^2 + P_\infty \right] x dx \quad (1.3-14)$$

Assuming that $\frac{dT_s}{dT_p} = \frac{T_s}{T_p}$ and solving Equation (1.3-14) for V_p

$$V_p = \left\{ \frac{1}{\rho} \frac{\frac{dT_p}{dx}}{2\pi R^2 x} \left(1 + \frac{T_s}{T_p} - \frac{2\pi R^2 x}{\frac{dT_s}{dx}} P_\infty \right) \right\}^{\frac{1}{2}} \quad (1.3-15)$$

Similarly to the development of Equations (1.3-9) through (1.3-11) but with the additional assumption that A_i is equal to A_p

$$\frac{2\pi R^2 x}{\frac{dT_p}{dx}} P_\infty = 1 - \left(\frac{T_s}{T_p} \right) \quad (1.3-16)$$

It follows that

$$\frac{V_p}{\Omega R} = \left\{ \left(\frac{1 - X_H^2}{X} \right) \left(\frac{T_s}{T_p} \right) \left(\frac{dC_T}{dx} \right) \right\}^{\frac{1}{2}} \quad (1.3-17)$$

From blade - element analysis

$$\frac{dC_T}{dx} = \frac{a\sigma}{2(1-X_H^2)} \left[\theta x^2 - \frac{V_p}{\Omega R} x \right] \quad (1.3-18)$$

Substituting Equation (1.3-17) into Equation (1.3-18) and solving for $\frac{dC_T}{dX}$

$$\frac{dC_T}{dX} = \frac{\left(\frac{a\sigma}{4}\right)^2}{(1-X_H^2)} \frac{T_s}{T_P} \left\{ 2X + \frac{8\theta_P X^2}{a\sigma T_s/T_P} - 2X \sqrt{1 + \frac{8\theta_P X}{a\sigma T_s/T_P}} \right\} \quad (1.3-19)$$

With

$$\sigma = \sigma_0 + \sigma_1 X$$

$$\theta = \theta_0 + \theta_1 X$$

$$\begin{aligned} \frac{dC_T}{dX} = \frac{T_s}{T_P} \frac{\left(\frac{a}{4}\right)^2}{1-X_H^2} & \left\{ X(2\sigma_0^2) + X^2\left(4\sigma_0\sigma_1 + \frac{8\sigma_0\theta_0}{a T_s/T_P}\right) + X^3\left(2\sigma_1^2 + \frac{8\theta_0\sigma_1 + 8\theta_1\sigma_0}{a T_s/T_P}\right) \right. \\ & \left. + X^4\left(\frac{8\theta_1\sigma_1}{a T_s/T_P}\right) - 2\left(\sigma_0 X + \sigma_1 X^2\right) \sqrt{\sigma_0^2 + X\left(2\sigma_0\sigma_1 + \frac{8\sigma_0\theta_0}{a T_s/T_P}\right) + X^2\left(\sigma_1^2 + \frac{8[\sigma_0\theta_1 + \sigma_1\theta_0]}{a T_s/T_P}\right) + X^3\left(\frac{8\theta_1\sigma_1}{a T_s/T_P}\right)} \right\} \end{aligned} \quad (1.3-20)$$

The integration of Equation (1.3-20) gives the thrust coefficient with linear twist and taper.

For zero twist and taper, the thrust coefficient is given by,

$$\begin{aligned} C_T = \frac{\left(\frac{a\sigma}{4}\right)^2}{1-X_H^2} \frac{T_s}{T_P} & \left\{ 1 - X_H^2 + \frac{8\theta(1-X_H^3)}{3a\sigma T_s/T_P} - 2\left(\frac{a\sigma T_s/T_P}{8\theta}\right)^2 \left[\frac{2}{5} \left(1 + \frac{8\theta}{a\sigma T_s/T_P}\right)^{5/2} - \frac{2}{5} \left(1 + \frac{8\theta X_H}{a\sigma T_s/T_P}\right)^{5/2} \right. \right. \\ & \left. \left. - \frac{2}{3} \left(1 + \frac{8\theta}{a\sigma T_s/T_P}\right)^{3/2} + \frac{2}{3} \left(1 + \frac{8\theta X_H}{a\sigma T_s/T_P}\right)^{3/2} \right] \right\} \end{aligned} \quad (1.3-21)$$

Out of Ground Effect, Equation (1.3-15) becomes

$$\frac{V_p}{\Omega R} = \left\{ \frac{1-X_H^2}{2X} \frac{dC_T}{dX} \left(1 + \left(\frac{T_s}{T_p} \right)_\infty \right) \right\}^{1/2} \quad (1.3-22)$$

and C_T of Equation (1.3-19) is calculated replacing

$$\frac{T_s}{T_p} \quad \frac{1 + \left(\frac{T_s}{T_p} \right)_\infty}{2}$$

1.4. DETERMINATION OF PROPELLER POWER

The propeller power is given by

$$P = C_P \Omega^3 R^3 \pi R^2 (1 - X_H^2) \quad (1.4-1)$$

where

$$C_P = \frac{1}{1-X_H^2} \int_{X_H}^1 \frac{a\sigma}{2} \left[\left(\frac{\delta_2}{a} - 1 \right) \left(\frac{V_p}{\Omega R} \right)^2 X + \left\{ \theta \left(1 - \frac{2\delta_2}{a} \right) - \frac{\delta_1}{a} \right\} \frac{V_p}{\Omega R} X^2 + \left(\frac{\delta_0}{a} + \frac{\delta_1}{a} \theta + \frac{\delta_2}{a} \theta^2 \right) X^3 \right] dX \quad (1.4-2)$$

Assuming V_p to be constant and also zero twist and taper, the power coefficient becomes,

$$C_P = \frac{a\sigma}{2(1-X_H^2)} \left[\frac{1-X_H^2}{2} \left(\frac{V_1}{\Omega R} \right)^2 \left(\frac{\delta_2}{a} - 1 \right) + \frac{1-X_H^3}{3} \left(\frac{V_1}{\Omega R} \right)^3 \left\{ \theta \left(1 - \frac{2\delta_2}{a} \right) - \frac{\delta_1}{a} \right\} + \frac{1-X_H^4}{4} \left(\frac{\delta_0}{a} + \frac{\delta_1}{a} \theta + \frac{\delta_2}{a} \theta^2 \right) \right] \quad (1.4-3)$$

where

$$\frac{V_p}{\Omega R} = \sqrt{C_T \frac{T_s}{T_p} \left(1 + \frac{A_p}{A_i} \right)}$$

For varying V_p , the power coefficient is obtained similarly to the corresponding derivation for C_T in Section 1.3., and becomes

$$C_p = \frac{a\sigma}{2(1-X_H^2)} \left\{ \left(\frac{\delta_2}{a} - 1 \right) \left(\frac{a\sigma}{4} \right)^2 \left(\frac{T_s}{T_p} \right)^2 \left[1 - X_H^2 + \frac{m}{3} (1 - X_H^3) \right] + \left(\frac{\delta_0}{a} + \frac{\delta_1}{a} \theta + \frac{\delta_2}{a} \theta^2 \right) \frac{1 - X_H^4}{4} \right. \\ \left. - 2 \frac{(\frac{\delta_2}{a} - 1)}{m^2} \left(\frac{a\sigma}{4} \right)^2 \left(\frac{T_s}{T_p} \right)^2 \left[\frac{2}{5} (1+m)^{\frac{5}{2}} - \frac{2}{5} (1+mX_H)^{\frac{5}{2}} - \frac{2}{3} (1+mX_H^3)^{\frac{3}{2}} \right] \right\} \\ + \frac{a\sigma}{2} \frac{1}{1-X_H^2} \left[\theta \left(1 - \frac{2\delta_2}{a} \right) - \frac{\delta_1}{a} \right] \int_{\frac{V_1}{\Omega R}}^{X_H} x^2 dx \quad (1.4-4)$$

where $V_p/\Omega R$ is given by Equation (1.3-22), and $m = \frac{\theta \theta}{a\sigma T_s/T_p}$

To calculate the power coefficient, C_p , for Out of Ground Effect conditions, T_s/T_p in Equations (1.4-3) and (1.4-4) is replaced by $\frac{1 + (T_s/T_p)_\infty}{2}$

1.5. DUCT EFFICIENCY

The duct efficiency is defined as the nozzle exit air power divided by the air power provided by a 100 percent efficient propeller.

$$\eta_D = \frac{P_{ej} A_j V_j}{T_p V_p} \quad (1.5-1)$$

Using the equation of continuity, $A_j V_j = A_p V_p$ Equation (1.5-1) can also be written

$$\eta_D = P_{ej} / \frac{T_p}{A_p} \quad (1.5-2)$$

Defining a loss factor, k_2 , such that

$$P_0 + q_0 = P_j + q_j + k_2 q_0 \quad (1.5-3)$$

Equation (1.5-1) becomes also

$$\eta_D = \frac{1 + T_s/T_P}{1 + \left(1 - \frac{P_j}{P_{ej}}\right)(1 + k_2)\left(A_j/A_P\right)^2} \quad (1.5-4)$$

The flow behind the propeller is, generally, rotational and turbulent. No adequate theoretical method exists, at present, to predict the duct efficiency, η_D , or the duct loss factor, k_2 . It becomes necessary, therefore to resort to empirical data, as presented in References 1, 2, and 3, etc. The duct efficiencies and loss factors experienced in the tests under the present program are presented in Section 2.

1.6. EFFECT OF INLET RING

By appropriate design of the inlet ring the thrust of a propeller-duct combination exceeds the thrust of the propeller alone. In the evaluation of the effect of the inlet ring on the performance of a ducted propeller, two cases must be distinguished:

- a.) Operation In Ground Effect
- b.) Operation Out of Ground Effect

For annular jet GEMs only Case a.) is of interest, but because of the requirement for performance analyses of ducted fans out of ground effect, Case b.) will also be discussed.

1.6.1 Operation In Ground Effect

Test data indicate that in Ground Effect the geometry of the inlet ring is of secondary importance for the evaluation of the thrust of a ducted propeller, as compared with the effect of the back pressure, P_0 . This implies that the momentum

relation, Equation (1.3-11) is applicable, or

$$\frac{T_s}{T_p} = \left[1 - \frac{P_0}{T_p/A_p} \right] \left(A_i/A_p \right) \quad (1.6.1-1)$$

Equation (1.6.1-1) can also be expressed in terms of jet parameters, and the duct loss factor, k_2

$$\frac{T_s}{T_p} = \frac{\left(1 - P_j/P_{tj} \right) \left(A_j/A_p \right)^2}{1 + k_2 \left(1 - P_j/P_{tj} \right) \left(A_j/A_p \right)^2} \quad (1.6.1-2)$$

1.6.2 Operation Out of Ground Effect

Out of Ground Effect the design of the inlet ring strongly affects the ratio of shroud thrust to propeller

thrust, T_s/T_p . A sharper inlet lip results in lower value of

T_s/T_p . If the shroud cross section is an airfoil, camber as

well affects the inlet performance. It was not the purpose of this program to identify the most general inlet geometry parameter which will result in a universal relationship with

T_s/T_p . It has been found, however, that for inlet shapes of

interest to GEM design, the ratio of the projected inlet ring

and hub area to the propeller area results in T_s/T_p data that do

not vary for the two greatly different configurations tested in this program.

1.6.3. Analytical Determination Of T_s/T_p Out of Ground Effect

Consider the inlet geometry shown in Figure 2. An incremental shroud planform area, dA_s , is given by

$$dA_s = -R^2 \left[1 + \frac{r_s}{R} (1 + \cos \theta_s) \right] \frac{r_s}{R} \sin \theta_s d\theta_s d\psi \quad (1.6.3-1)$$

Neglecting the effect of the propeller hub the shroud thrust, T_s , is obtained as

$$T_s = - \int_{A_s} P_s dA_s \quad (1.6.3-2)$$

Where P_s is the gage pressure along the shroud inlet, it is assumed that P_s varies linearly as follows

$$P_s = k_s P_i \theta_s \quad (1.6.3-3)$$

From a momentum relationship

$$P_i = - \frac{T_p}{A_p} \left(1 - \frac{P_0}{T_p/A_p} \right) \quad (1.6.3-4)$$

Substituting Equations (1.6.3-1), (1.6.3-3) and (1.6.3-4) into Equation (1.6.3-2) and integrating

$$\frac{T_s}{T_p} = k_s \left(1 - \frac{P_0}{T_p/A_p} \right) \frac{\pi R^2 r_s/R \left(1 + \frac{3}{4} r_s/R \right)}{A_p} \quad (1.6.3-5)$$

Since $A_s = 4\pi R^2 (r_s/R) \left(1 + r_s/R \right)$, Equation (1.6.3-5) can also be written as:

$$\frac{T_s}{T_p} = \frac{k_s}{4} \left(1 - \frac{P_0}{T_p/A_p} \right) \left(\frac{A_s}{A_p} - \frac{\pi R^2 (r_s/R)^2}{A_p} \right) \quad (1.6.3-6)$$

For fully expanded flow out of ground effect $P_0 = 0$. The validity of the assumption made in Equation (1.6.3-3) and the value of k_s will be discussed in Section 3.

1.7 DETERMINATION OF BASE PRESSURE

The major analytical effort to date has been concentrated on the determination of the base pressure as a function of the jet total pressure. A review of the available theories and a comparison with experimental data is discussed in Reference 4. The correlation of test data with theory is also discussed in Section 3 of this report. In general, present theories predict a base pressure that is significantly higher than that obtained from tests.

1.8 EFFECT OF NOZZLE VELOCITY DISTRIBUTION

The previous sections discussed the performance analysis of the propeller-duct combination from the air intake to the air exit nozzle. Depending on the propeller blade geometry the exit flow velocity distribution can have various shapes. It appeared from previous work presented in Reference 5 that the velocity distribution which would result in a maximum base pressure recovery corresponds to a vortex type turning of the air flow from the jet. The basic performance problem, however, is not only determined by base pressure recovery, but by the total lift developed by both the base and the nozzles at constant power. To obtain a qualitative understanding of the effect of velocity distribution on the lift to power ratio, L/P , the following analysis was performed.

Considering the geometry of an annular jet nozzle as shown in Figure 3, and assuming that the value of t_e/R_j is sufficiently small so that R_j can be taken as constant across the nozzle,

$$P_b = \rho \frac{R}{R_j} \int_{1-t_e/R}^1 V_x^2 dx \quad (1.8-1)$$

The jet pressure for any value of $x \geq 1 - t_e/R$ is

$$P_j = \rho \frac{R}{R_j} \int_x^1 V_x^2 dx \quad (1.8-2)$$

The nozzle velocity distribution is assumed to vary linearly across the nozzle. With the notation of Figure 4

$$V_x = V_o (1 + \alpha x) \quad (1.8-3)$$

Substituting Equation (1.8-3) into Equations (1.8-1) and (1.8-2), respectively, and integrating,

$$P_b = \rho \frac{R}{R_j} V_o^2 \left[t_e/R + \alpha E_1 + \frac{\alpha^2}{3} E_2 \right] \quad (1.8-4)$$

where $E_1 = 1 - (1 - \frac{t_e}{R})^2$, $E_2 = 1 - (1 - \frac{t_e}{R})^3$

$$P_j = \rho \frac{R}{R_j} V_o^2 \left[(1-x) + \alpha(1-x^2) + \frac{\alpha^2}{3}(1-x^3) \right] \quad \text{for } x \geq 1 - \frac{t_e}{R} \quad (1.8-5)$$

For the case of constant velocity across the nozzle,

$$V = V_A \quad \text{and}$$

$$P_{bA} = \rho \frac{R}{R_j} V_A^2 \frac{t_e}{R}, \quad P_{jA} = \rho \frac{R}{R_j} V_A^2 (1-x) \quad (1.8-6)$$

The airpower for a circular annular jet is given by

$$P = 2\pi R^2 \rho \int_{1-t_e/R}^1 \left(P_j + \frac{1}{2} \rho V_x^2 \right) V_x x dx \quad (1.8-7)$$

Substituting Equations (1.8-3) and (1.8-5) into Equation (1.8-7) and integrating

$$P = 2\pi R^2 \rho V_o^3 \left[\frac{D_1 E_1}{2} + \frac{D_2 E_2}{3} + \frac{D_3 E_3}{4} + \frac{D_4 E_4}{5} + \frac{D_5 E_5}{6} \right] \quad (1.8-8)$$

where

$$\begin{aligned}
 D_1 &= R/R_j (1 + a + a^2/3) + 1/2 \\
 D_2 &= R/R_j (-1 + a + a^2 + a^3/3) + 3/2 a \\
 D_3 &= R/R_j (-2a) + 5/2 a^2 \\
 D_4 &= R/R_j (-4/3 a^2) + a^3/2 \\
 D_5 &= R/R_j (-a^3/3) \\
 E_3 &= 1 - (1 - t_e/R)^4 \\
 E_4 &= 1 - (1 - t_e/R)^5 \\
 E_5 &= 1 - (1 - t_e/R)^6
 \end{aligned}$$

For constant velocity distribution, $a = 0$ and

$$P_{v_A} = 2\pi R^2 \rho V_A^3 \left[\left(R/R_j + \frac{1}{2} \right) E_{1/2} - \frac{1}{3} R/R_j E_2 \right] \quad (1.8-9)$$

For constant power, it follows by equating Equations (1.8-7) and (1.8-8)

$$\left(\frac{V_A}{V_0} \right)^3 = \frac{\frac{D_1 E_1}{2} + \frac{D_2 E_2}{3} + \frac{D_3 E_3}{4} + \frac{D_4 E_4}{5} + \frac{D_5 E_5}{6}}{\left(R/R_j + \frac{1}{2} \right) E_{1/2} - \frac{1}{3} R/R_j E_2} \quad (1.8-10)$$

The vehicle lift is given by

$$L = L_j + L_b = \int_{A_j} (P_j + \rho V_x^2) dA_j + P_b A_b \quad (1.8-11)$$

The ratio of the lift of the vehicle for varying velocity across the nozzle, L , with the vehicle lift at

constant velocity, L_{v_A} , is given by

$$\frac{L}{L_{v_A}} = \frac{\frac{B_1 E_1}{2} + \frac{B_2 E_2}{3} + \frac{B_3 E_3}{4} + \frac{B_4 E_4}{5} + \frac{1}{2} \frac{R}{R_j} (1 - t_e/R)^2 \left[t_e/R + a E_1 + \frac{a^2 E_2}{3} \right]}{\left(\frac{V_A}{V_0} \right)^2 \left[\frac{E_1}{2} \left(\frac{R}{R_j} + 1 \right) - \frac{E_2}{3} \frac{R}{R_j} + \frac{1}{2} (1 - t_e/R)^2 \frac{R}{R_j} \frac{t_e}{R} \right]} \quad (1.8-12)$$

where

$$B_1 = R/R_j (1 + a + a^2/3) + 1$$

$$B_2 = -R/R_j + 2a$$

$$B_3 = -R/R_j a + a^2$$

$$B_4 = -R/R_j (a^2/3)$$

The variation of L/L_{v_A} for constant power vs.

normalized, non-dimensional slope of the velocity across the nozzle, aV_0/V_A , is shown in Figure 5. It is seen that the maximum lift, for a given nozzle air power is obtained for a constant velocity distribution across the nozzle.

2.0 TEST RESULTS

In this section the results of the test program are presented and discussed. Data from the literature is also presented where applicable. The details of the test program are listed in the Appendix. The tabular test data may be obtained from Kellett Aircraft Corporation upon written request. The configurations tested may be summarized as follows:

1. Duct Configuration
 - a. Straight Duct, (axisymmetric, straight walled)
 - b. Curved Duct (90 degree angle between propeller plane and nozzle plane)
2. Inlet Rings
 - a. Large Quarter Elliptic
 - b. 4.5 inch Semi-Circular Cross-Section
 - c. 1.5 inch Semi-Circular Cross-Section

This data will be compared with the theory in the next section.

2.1 OVERALL PERFORMANCE

2.1.1 Performance as a Function of Height-Diameter Ratio

2.1,1.1 Straight Duct

The overall performance of the straight duct for the tests performed with this configuration are shown in Figure 6, in terms of the lift to power ratio against altitude to diameter ratio, h/D . These tests were performed at constant propeller disc loading, T_p/A_p . The numbers shown next to each test points denote the ratio of the total ground board reaction to the total base area of the duct, L/S . It is noted that maximum power loading, L/P , is obtained at an h/D of about

0.1. At values of h/D lower than 0.1, the propeller stalls and any potential gain in L/P that becomes available with decreasing h/D is more than compensated for by the loss in propeller efficiency due to blade stall. At very low height ($h/D = 0.03$) smoke studies have shown that there is almost zero net flow through the duct; however, a pressure is maintained in the duct by a recirculating flow through the propeller. This recirculating flow enters the propeller through the inboard portion of the blade and escapes from the duct through the area swept by the stalled propeller blade tips. It should be noted that the performance at zero height is not a trivial condition since the static height of the nozzles can be zero for any GEM depending on the landing gear and the terrain. However, propeller blade stall can usually be eliminated for these conditions by reducing the blade incidence and increasing rpm.

Examining the variations of L/S at constant h/D and L/P it is seen that comparative performance must be evaluated at constant L/S . The available test data were cross plotted and the results are shown in Figure 7 for area loadings, L/S , of 10 and 15 psf. Calculated performance for the nozzle inclination and nozzle thickness of the test configuration and the performance of an annular jet with optimum nozzle angle and nozzle thickness are also shown. The calculated performance curves are based on the Strand theory as corrected to agree with test data in Reference 6. An internal efficiency of 60 percent was assumed for these calculations. It may be seen in Figure 7 that the tested performance is slightly better than that equivalent to a 60% efficiency at h/D values less than about 0.3. At h/D of 0.15 the apparent internal efficiency is about 67 percent for both of the area loadings shown. The tested performance is also better than the calculated optimum performance for the L/S of 10 psf at h/D from 0.22 to 0.44 for this assumed internal efficiency.

2.1.1.2 Curved Duct

The overall performance of the curved duct is shown in Figure 8. This duct is described in detail in Appendix I; however, it should be noted at this point that this unit has a nozzle area to total base area ratio of 0.33 as compared with 0.80 for the straight duct.

It is seen from Figure 8 that at the same propeller disc loading, T_p/A_p , the curved duct produces more pounds per horsepower than the straight duct at all values of h/D below about 0.15. However, the curved duct also produces less L/S than the straight duct except at values of h/D less than about 0.04. As pointed out previously, a suitable comparison should be made only at constant T/S .

It may be observed from Figure 8 that the performance data does not evidence propeller stall effects with decreasing h/D of equal magnitude as was found for the straight duct tests. This is due to the effect of the smaller nozzle to base area of the curved duct which reduces the propeller blade angle of attack for a given h/D . As will be shown later in this section, propeller blade angles of attack are a function of the blade pitch setting and the parameter $\pi D h/A_i$. Therefore, the curved duct does not experience propeller blade stall until a lower h/D than the straight duct and at lower h/D the increase in performance due to ground effect masks the effect of blade stall on performance.

It may also be noted from this figure that with the curved duct the large quarter-elliptic inlet ring gives slightly better performance than the 4.5 inch inlet ring at all

heights tested. Also the curved duct with the plenum gives slightly poorer performance than the curved duct alone.

As an independent check of the test data the data from Reference 7 is also plotted on this figure. The data from this reference is from an axisymmetric duct which has a propeller to jet area ratio of 0.618 and a nozzle to total base area ratio of 0.103. This duct also includes radial stability augmenting slots in the base. This referenced data includes the losses in one transmission between the torque meter and the propeller. The data shown from this reference in Figure 8 were obtained at a constant lift at a similar total base area loading, L/S , of 10 psf as for the curved duct tests and show a very similar performance to that of the curved duct of the present program.

2.1.2 Effect of Detail Geometry Modifications on Performance

As noted in the previous section the variation of the two dependent variables L/S and L/p with h/D or configuration precludes the comparison of performance data in this form. This difficulty does not occur if the performance data are presented in the form of the power factor, Z . This parameter is used in Figures 9 and 10 to show the effect the following design modifications:

2.1.2.1 Inlet Geometry

The three inlet rings described in the Appendix were tested on the straight and the curved ducts. The effect of these rings on performance is shown in Figures 9 and 10 for the straight and curved ducts, respectively. It may be noted from these figures that the quarter elliptic inlet ring gives about 5 percent better performance in the straight duct than the 4.5 inch semicircular inlet ring. The curved duct performance is almost identical with either of these inlet rings.

The effect of the long inlet on the performance of the straight duct is also shown in Figure 9. As shown by this data, the performance with the long inlet is about ten percent less

than the short inlet at large and small h/D . At an h/D of 0.2 the performance with either inlet length is essentially the same.

2.1.2.2 Internal Modifications to Curved Duct

From tuft studies it was found that the flow in the curved duct was separated in the region of smallest curvature of the outer wall ($\psi = 0^\circ$, $\theta = 30^\circ$). To improve this flow the following modifications were tried:

- 1.) Guide Vane
- 2.) Axial Streamlined Body

It was found that both of these modifications reduced performance as shown in Figure 10. At low height the effect of the body is small; however, at h/D of 0.20 the body reduces performance about 18 percent. The guide vane also caused about an 18 percent reduction in performance. The above reduction in performance were evidenced despite the fact that the tufts in the duct seemed to indicate that the flow was improved for each of these modifications. This apparent paradox is probably caused by the drag losses of these objects being larger than the energy losses due to flow separation.

2.1.3 Performance with Pitch or Roll Inclination of the Annular Jet

2.1.3.1 Straight Duct

The effect of ground board inclination on the performance and flow of the short duct and the short duct with the nozzle and base extension at an h/D of 0.14 is shown in Figure 11. The total base area loading decreases slightly with increased ground board inclination and the power loading remains essentially constant. The maximum change in the power factor represented by these changes in performance is about 10 percent of the value of Z without inclination.

2.1.3.2 Curved Duct

The curved duct performance when inclined is as shown in Figure 12. It may be noted that the changes in performance are somewhat larger than were noted with the straight duct; however, performance is significantly improved for nose down and left side up inclinations. At an h/D of 0.182 the maximum performance was achieved at minus seven degrees pitch and plus seven degrees roll, and it was not until these inclinations were about twelve degrees that the performance decreased to the value without inclination. The performance decreased at about the same magnitude as the straight duct for nose up and left side down inclinations; that is, about a 10 percent increase in Z , for a 12 degree inclination.

2.1.3.3 Control Plug in Curved Duct

To provide some insight into the performance penalties which are required for control an exploratory study was made into the effects of two sizes of a plug inserted into the nozzles of the curved duct. These plugs were tested at various azimuthal positions. The effect of these plugs on performance is as shown in Figure 13. The effect of the plugs on the center of pressure of the annular jet is as shown in Figure 14. From these two figures it may be concluded that a center of pressure shift of 20 percent of the base radius can be achieved in any direction with about a 20 percent increase in power.

2.1.4 Overall Internal Efficiency

The internal efficiency of the test units was measured at various ground board heights. This efficiency was determined by measuring the velocity and total pressures in the flow at various radial and azimuthal positions. From these measurements the air horsepower was calculated. The internal efficiency, in percent, is then 100 times the ratio of the air horsepower to the input shaft horsepower.

The tests indicated that the maximum internal efficiency with the straight duct test unit was about 78 percent and with the curved duct the maximum internal efficiency was about 68 percent. The variation of these efficiencies

with h/D is shown in Figure 15. The reduction in performance due to the duct turning angle was caused in part by losses due to a flow separation in the duct and in part by the losses due to the asymmetry of the flow through the propeller.

2.2 PROPELLER DATA

The propeller tested in the curved and straight ducts had zero twist rectangular blades. All testing was performed at the same pitch setting. The unit tested permitted the measurement of the thrust produced by the propeller alone. The geometry and instrumentation of this unit is described in detail in Appendix I.

2.2.1 Thrust

The propeller thrust coefficient data obtained for the straight and curved duct are shown in Figure 16. It may be seen in the figure that the propeller thrust coefficient for the straight and curved ducts are coincident when plotted against the GEM clearance area to nozzle area ratio, $\pi D h/A_j$.

The curved duct and the short straight duct plenum with the large base modification show a somewhat higher thrust coefficient.

2.2.2 Power

The propeller power required may be shown in nondimensional form as a power coefficient. The data obtained for the various straight and curved duct configurations are

shown in Figure 17 plotted against $\pi D h/A_j$. While there is some scatter in this data it appears that for a given $\pi D h/A_j$

the configuration with the plenum requires a slightly larger torque coefficient than the straight duct. The curved duct requires a slightly smaller power coefficient than the straight duct. Out of ground effect power coefficient data is also shown in this figure for the straight duct and the curved duct with the plenum.

2.2.3 Flow Conditions at the Propeller

The flow conditions which produced the above mentioned performance have been measured in detail. In general, these conditions result from an interaction of the propeller and the duct; however, the general flow field and the inlet flow will be described in Section 2.3. The flow conditions which directly affect propeller performance are the following:

- a. Magnitude and distribution of the velocity.
- b. Swirl angle in the flow.

To determine the velocity at the propeller, flow surveys were made at various distances before and after the propeller. The data obtained for an out-of-ground-effect condition is shown in Figure 18, with the velocity non-dimensionalized by the theoretical value of the velocity for uniform inflow. The out-of-ground-effect conditions are shown since for this case the velocity at the propeller is largest and the velocity distribution is most pronounced. It is seen from Figure 18 that before the propeller the velocity distribution is uniform and the velocity ratio is unity except for the boundary layer at the shroud and a decrease in the flow near the centerbody. For the measurements nearest to the front of the propeller (0.13 of the propeller tip radius) the boundary layer flow occupies about 10 percent of the inlet area and the reduced flow near the centerbody is about 90 percent of the theoretical value and covers about 30 percent of the propeller area. Over the remaining propeller area the velocity is uniform at the theoretical value. Thus, the area weighted average velocity is within ten percent of the theoretical velocity, but is lower than predicted. The propeller changes the uniform approach velocity to a trapezoidal velocity distribution which of course, cannot occur discontinuously, and which is not quite established at a distance of 0.17 of the propeller tip radius behind the propeller. The change from a uniform flow to the trapezoidal flow requires that there be a radial component of the velocity. This trapezoidal velocity distribution is probably the most nonuniform velocity which would be achieved unless the propeller was specially designed to produce a non-uniform velocity (with reversed twist or an inversely tapered blade planform). This non-uniformity of the inflow velocity is small enough to expect the assumption of uniform inflow to yield reasonably accurate results for performance calculations for installed propellers.

In the curved duct the propeller also produces a similar velocity distribution, however, the curvature produces also an azimuthal variation on the flow through the propeller. The dynamic pressure of the flow after the propeller at an

h/D of 0.182 and $T_P/A_P = 16$ psf are as follows:

r/R of Measurement	f_{CONSTANT}	$f_{\text{OSCILLATION}}$
0.52	3.8	$2.2 \sin (\psi - 270^\circ)$
0.80	10.0	$2.0 \sin (\psi - 270^\circ)$
0.92	13.1	$1.9 \sin (\psi - 270^\circ)$

This data indicates that there is about 10 percent of the velocity near the 75 percent blade radius.

The magnitude of the average velocity at the propeller depends on the requirements of the annular jet as influenced by the duct system, as has been discussed previously in Section 1.8. However, the ratio of the velocity at the propeller to the propeller tip speed may be calculated from any of the following relations:

$$\begin{aligned}
 \frac{V_P}{\Omega R} &= \sqrt{2 C_T (T_s/T_P)} \\
 &= \sqrt{2 C_T (-P_i/T_P)} \\
 &= \sqrt{2 C_T (P_{tj}/T_P/A_P) (1 - P_j/P_{tj}) (A_j/A_P)^2}
 \end{aligned}$$

In the test program these pressure and thrust ratios were measured independently. Therefore, the velocity ratio at the propeller was calculated using each of these relations and the results are compared in Figure 19.

It may be noted from Figure 19 that the relations which depend on the momentum relations discussed in the theoretical analysis result in a lower value of the velocity at the propeller than the velocity data which was measured

directly at the nozzles and in the inlet. It should be noted that the propeller velocity ratio is the same for the curved and straight duct at the same $\pi D h / A_j$. This gives considerable support to the test data since a large number of measurements are involved with two different test set ups.

The propeller also causes a rotation or swirl in the flow as a reaction to the propeller torque. Typical swirl angle data are shown in Figure 20 for the straight duct. This data shows that swirl angle varies with height. This variation is of sufficient magnitude that it would be difficult to design an anti-rotation vane system which would give good performance at all heights. It should also be noted that at low heights when the swirl angle is large the flow is reduced so that the rotational energy loss is always small (about 2 percent of the air horsepower). This conclusion, of course, only applies to configurations similar to those tested.

2.2.4 Propeller Efficiency

As given previously the efficiency of the propeller is defined as:

$$\eta_p = \frac{T_p V_p}{550 \text{ HP}}$$

This relation may also be expressed as

$$\eta_p = \left(\frac{C_T}{C_P} \right)^{\frac{3}{2}} \frac{A_j}{A_p} \sqrt{2 \left(P_{tj} / T_t \right) \left(1 - P_j / P_{tj} \right)}$$

These parameters have been measured and the efficiency calculated with this relation is shown in Figure 21. It may be noted in this figure that an average efficiency of 94 percent is reached

at about a $\pi D h / A_j$ of 1.7. This efficiency for the propeller is unusually high. A maximum efficiency of about 35 percent was expected for this zero twist rectangular planform propeller. If the value of P_{tj} was 0.9 of the measured value, η_p would be 85 percent. As is discussed in Section 2.3.2 there are also

other reasons to suspect the pressure measurements.

2.3 DUCT PERFORMANCE

The function of the duct is to channel the flow to the propeller taking advantage of the negative inlet pressures to increase the flow. The duct then delivers the flow from the propeller to the nozzles, and should in conjunction with the propeller provide the velocity distribution which will give best annular jet performance. To determine how well the duct performs this function, surveys were made of the flow into the inlet in the duct and at the nozzle exits. Typical examples of this data are presented in this section to show the general flow field of the test units.

2.3.1 Flow Field Data

For the straight duct out-of-ground effect, the flow field in the vicinity of the propeller and inlet was investigated and the data obtained are shown in Figure 22. Upstream of the propeller the total pressure is approximately atmospheric and therefore, the static pressure data shown also is indicative of the dynamic pressure of the flow into the inlet. Downstream of the propeller the static and total pressures are increased so that the total pressure in the duct is about 80 percent of the propeller disc loading. The static pressure in the duct downstream of the propeller is slightly negative (gage) apparently due to propagation of the negative pressure induced at the periphery of the nozzle and at the base of the centerbody.

The effect of a change in the length of the inlet on the inlet flow is also shown in Figure 22. At the inlet the flow is shown to be similar for the two distances to the propellers that were tested. However, for the case where the duct inlet is close to the propeller the velocity is significantly larger near the outer end of the blades. The difference in the shape of the velocity distribution shown is apparently due to the change in the proximity of the inlet to the propeller. As will be explained later, the difference in the magnitude of the inflow velocity in this region is apparently due to the difference in the disc loading of these tests on inlet performance rather than due to the effect of the inlet length.

For conditions where the nozzles are close to the ground, the flow is as shown in Figure 23. This figure shows pressure data obtained at various locations in the duct. The inlet flow data given in Figure 23 can also be compared with

the data of Figure 22. This comparison shows that the inlet flow pressures become a smaller fraction of the propeller disc loading as the nozzle height is reduced. The static pressure in the duct is shown to be fairly uniform in the region behind the propeller to the nozzle, and varies from nearly zero gage pressure out of ground effect, to a value slightly less than the base pressure when the nozzle is very near the ground.

It may also be noted in Figure 23 that at $h/D = 0.12$ the velocity of the flow through the duct (as indicated by the difference between the total and the static pressure data) is almost zero near the centerbody. This indicates that the effective nozzle thickness is less than the actual nozzle thickness. Tuft studies show that the flow in this region is reversed, apparently due to the influence of the base pressure on the flow. The reduction of effective nozzle thickness with height may reduce the base pressure which can be achieved for a given nozzle total pressure and also may reduce overall performance.

Typical nozzle flow data for the curved duct are shown in Figure 24 for h/D of 0.181. This data shows azimuthal and radial variations in the total and static pressures at the nozzle. As shown in the figure the nozzle static pressure is negative at zero degrees ψ apparently due to the effects of the small radius of curvature of the duct in this area. This effect causes some changes to the annular jet performance, as will be discussed in a later section.

2.3.2 Duct Efficiency

The efficiency of the duct system may be determined by measuring the total pressure of the flow at the jet, P_{t_j} , and the propeller disc loading, T_p/A_p . The ratio of these two parameters is the efficiency of the duct, η_D , since this ratio is equal to the ratio of the air horsepower delivered to the nozzles divided by the air horsepower produced by the propeller. This is derived in the theory. The duct efficiencies of the test units are shown by the data of Figure 25.

It is noted that the product of the duct efficiency and the isolated propeller efficiency is the overall internal efficiency. A comparison of the data in Figures 25, 21 and 15.

shows fairly good agreement of η_i with the product of η_p and η_d , this product being about six percent less than η_i .

This difference is possibly due to the manner in which the data of the total pressure was averaged. It should be noted that the total pressure varies with the radius. For this report,

all average P_t data are an area weighted average, which is the one which should be used for determining forces. However, for determining air power a flow quantity weighted average should be used. Since the flow quantity increases with P_t when the

static pressure is constant a flow quantity weighted average is larger than an area weighted value. Therefore, the data given in Figure 25 indicates a slightly smaller duct efficiency than the actual value.

It should be noted in Figure 25 that duct efficiency is reduced by duct curvature. About 10 percent less efficiency was obtained for the curved duct than the straight duct. The addition of the plenum caused a further decrease in efficiency. Still it is noted that the efficiency of the configuration with the plenum is unexpectedly high. Since this configuration consisted of the straight duct, the plenum and then the curved duct in series it is expected that the efficiency of this combination would be the product of the efficiency of the components. This would indicate that the efficiency of the plenum was 94 percent efficient at a $\pi D h / A_j$ of unity. It

was expected that the plenum efficiency would be considerably less than this value. One reason for this large plenum efficiency is probably due to the alignment of the straight duct exit with the inlet of the curved duct. Also it is possible that the curved and straight duct efficiencies benefit from this combination of ducts and plenum.

A portion of the data which relates to duct efficiency has an apparent discrepancy which cannot be explained. That is, for numerous data points with the straight duct at all tested heights and for the curved duct at $\frac{\pi D h}{A_j}$ greater than unity the total pressure behind the propeller was found to be less than the total pressure at the nozzles. This data is shown in Figure 26. Although the discrepancy is of small magnitude, it is of significance since it was measured at so many points. Possible

explanations for this discrepancy are:

- 1.) The rotation in the flow
- 2.) Unsteady flow effects near the propeller
- 3.) Instrumentation inaccuracies

The inlet performance and duct losses are discussed in the following:

2.3.2.1 Inlet Performance

The inlet ring produces a thrust which is related to an increase of mass flow in the ducts. This thrust is caused by the negative static pressure acting on the area of the inlet ring.

The inlet ring surface static pressure was measured during these tests and typical data for an out-of-ground effect condition are shown in Figure 27. For this data, the propeller disc loading was used as a non-dimensionalizing parameter. The data shows that the flow separates from the surface at an inlet ring cross-section angle, θ_s , of about

135 degrees. Separation is indicated by the peak in the curve of surface static pressure with inlet angle. The thrust of the inlet ring was estimated by integrating the measured pressures across the inlet ring and the average ratio of inlet thrust to propeller thrust out-of-ground effect was found to be 0.70 for the specific test configuration.

The inlet flow also causes a reduction in the surface static pressure on the nose of the centerbody. This static pressure was measured and the typical data obtained are shown in Figure 23. The thrust which this pressure distribution represents was also obtained by numerically integrating the pressure, and for the out-of-ground effect condition, was found to be about 0.1 of the propeller thrust. The centerbody nose contribution decreases with decreasing nozzle height and becomes

insignificant at values of h/D less than 0.3.

The straight duct test unit was also tested out-of-ground effect with an increased inlet length. That is a duct extension about three propeller radii long was placed between the propeller and the inlet ring. Static and total

pressure measurements were made at the mid length of this extension and the data are shown in Figure 29, and similar inlet data measured close in front of the propeller are shown in Figure 22.

The total pressure data shown in Figure 29 indicates that with increased disc loading the outer wall boundary layer becomes less thick. Since the inlet loss is the total pressure times the flow quantity a decrease in this boundary layer indicates improved performance. As a consequence of the increased boundary layer the static pressure to disc loading ratio becomes of larger magnitude (more negative) with decreased disc loading. From momentum relations and Bernoulli's equation, it can be shown that:

$$\frac{T_s}{T_p} = - \frac{P_i}{T_p} \frac{A_p}{A_i} \left(\frac{A_i}{A_p} \right)$$

Since the measured T_s/T_p seems to be independent of disc loading it appears that A_i/A_p varies with disc loading since $-\frac{P_i A_p}{T_p}$ is shown to vary. This effect may be considered as a contraction of the flow into the inlet which appears like a separation or a thickened inlet boundary layer. From this data A_i/A_p is about 0.76 at T_p/A_p of 9 psf, and is equal to unity at T_p/A_p of 15.6 psf. It should be noted that consideration of this effect may provide agreement of the propeller velocity ratio data shown in Figure 19.

It may also be noted from Figure 29 that the static pressure-disc loading ratio generally increases negatively near the centerbody at $r/R \approx 0.5$, as compared to values at .

This indicates that the velocity near the centerbody is higher than the velocity near the outer wall boundary layer of the duct. This effect is apparently due to the inlet since the velocity after the propeller is larger near the outer wall.

The data shown in Figure 29 can also be used to estimate the loss in efficiency due to inlet separation. Since the total pressure was zero until the loss due to the inlet, the negative total pressure near the outer wall represents

a loss of energy. This loss can be shown to represent about 2% of the input horsepower at a disc loading of 15.6 psf.

It may also be noted in Figure 29 that there does not appear to be a region of negative total pressure near the centerbody. This would substantiate the conclusion that the reason for the thick boundary layer near the outer wall is due to the inlet ring flow separation and not due to a boundary layer caused by skin friction.

The measured inlet ring thrust out-of-ground for the 4.5 inch semicircular cross section inlet ring is compared with similar data from the literature in Figure 30. Since this data agrees fairly well with the data from the literature there was no further effort to correlate the thrust of the other inlet configurations with this out-of-ground effect data. As previously noted the other inlet rings were tested to determine the effect of the inlet ring design on overall performance.

The theoretical variation of inlet ring thrust with inlet ring area is also presented in this figure, as will be discussed in Section 3.

The effect of the height of the nozzles from the ground on the inlet thrust is shown in Figure 31. The ratio of inlet thrust to propeller thrust decreases with height since for a given propeller thrust the flow through the duct decreases with the height. With a reduction in the flow into the inlet the static pressure in the inlet increases, and hence the thrust contribution of the inlet ring decreases. When plotted against $\pi D h / A_j$ the ratio of T_s to T_p is coincident for the straight and curved ducts.

It should be noted that the curved duct inlet thrust varies with the propeller azimuth angle, ψ . Typical data are shown in Figure 32 that show this variation. When integrated this data can be represented by the following relation:

$$\frac{T_s}{T_p} = 0.405 + 0.143 \cos(\psi - 20^\circ)$$

This relation was determined for the data shown for $\pi D^h/A_j$ of 2.2, and would only be expected to be valid for conditions near this point.

2.4 ANNULAR JET PERFORMANCE

The characteristics of the annular jet determines the lift producing capacity of the GEM and the purpose of the previously discussed GEM component characteristics is to provide information on the internal flow feeding the jets. The present program was mainly concerned with the internal aerodynamic problems and the greater part of the test effort was confined to this area. Some measurements of the jet characteristics were obtained however, and this data is presented below with a brief discussion.

2.4.1 Base Pressure Recovery

The primary performance parameter of the usual annular jet configuration is the ratio of the base pressure to the total pressure of the jet. The test data for the curved and straight duct configurations is shown in Figure 33 with comparative test data from Reference 7 and various theoretically predicted data based on the theories from References 6, 8 and 9. It may be noted from this figure that the test data are considerably less than the theoretical values. At

$\pi D^h/A_j$ of unity the test value is only about 76 percent of the theoretical value. The test data from Reference 7 is not exactly comparable to the test data from this program, since the GEM tested in this reference had inclined nozzles and had a small nozzle width to diameter ratio, t_e/D , as compared with the straight or curved duct configurations. A comparison was also made of this data with the appropriate theory and it is seen that the data of Reference 7 are also about 20 percent less than the theoretical values.

It may be noted that the curved duct has a somewhat lower base pressure recovery than the straight duct. This unexpected loss in base pressure recovery is apparently due to the peculiar nozzle pressure distribution for this duct which was noted previously.

2.4.2 Nozzle Pressure

The nozzle static pressure data for the curved and straight ducts and the Reference 7 data are shown in Figure 34. This data shows that the nozzle static pressure-nozzle total pressure ratio reaches unity at zero height when there is no flow from the nozzle and becomes negative out of ground effect. It can be shown that most of the theories predict that the nozzle pressure is one-half the base pressure. The nozzle pressure data is presented as a ratio to the base pressure in Figure 35. This figure shows that the nozzle pressure is one-half the base pressure at only one height. At $\pi D h / A_j$

values less than about three the base pressure exceeds this theoretical value. Since as shown before the predicted base pressure recovery is optimistic and the nozzle static pressure is greater than predicted, it would be expected that annular jet configurations should have larger nozzle area to base area ratios than the theoretical optimum.

2.4.3 Augmentation Ratio

This ratio is of very questionable value; however, the test data obtained have been plotted in Figure 36 with comparative data from References 7, 10, and 11. It should be noted that the comparison of this data cannot be related to the annular jet performance as presented in other sections of this report.

3.0 CORRELATION OF ANALYTICAL METHODS WITH TEST RESULTS

In this section the analyses of Section 1 is compared with the test data of Section 2. The degree of correlation between analysis and test data is discussed.

3.1 PROPELLER PERFORMANCE

In Sections 1.3 and 1.4 methods are presented for predicting propeller thrust and power, respectively. Propeller performance calculations have been made with the method assuming constant velocity at the propeller and also with the method in which radial variations in the propeller inflow velocity are considered. The calculated data are shown with the comparative test data in Figure 37 for propeller thrust coefficient and in Figure 38 for the propeller power coefficient. These data were calculated assuming a constant slope of the airfoil section, 5.73/radian, and a power series drag polar with coefficients S_0 of 0.0087, S_1 of -.0216 and S_2 of 0.4. These airfoil characteristics are based on data given in References 12 and 13 for the tested 0012 Section. The calculated thrust coefficient data are not more than 10 per-

cent larger than the experimental values of all $\pi D h / A_j$ values larger than unity. At values of $\pi D h / A_j$ smaller than unity the calculated C_T increases more rapidly with decreasing $\pi D h / A_j$ than does the experimental C_T data. The reason for this

divergence of the calculated data from the experimental data is that the propeller blade tips are stalling. This may be shown by calculating the blade tip angle of attack, α_{TIP} ,

using the following relation

$$\alpha_{TIP} = \theta_{TIP} - \sqrt{2 C_T (\tau_s / \tau_r)}$$

The blade tip angle of attack based on the experimental value of C_T is shown in Figure 39. As shown in Reference 12 the 0012 airfoil of the tested propeller stalls at 11 degrees at the tested tip Mach numbers. This stall angle is in good agreement with the test data in that 10.5 degrees tip angle of attack

are reached at $\pi D h / A_j$ of unity. At angles of attack beyond stall the measured thrust should be less than the calculated

thrust since the calculations were made for a constant lift curve slope with no consideration for stall. If it was desired to predict the thrust coefficient for conditions with stall the airfoil section data from a reference such as Reference 12 should be used together with Equation 1.3-13. The value of $V_p/\Omega R$ is then found by an iteration method using numerical integration techniques.

It is seen from Figure 37 that for the sample calculation point the thrust coefficient based on a radially varying inflow velocity is approximately equal to that obtained using the constant inflow velocity assumption.

The calculated propeller coefficient is compared with experimental data in Figure 38. As shown in this figure the propeller power coefficient calculated with a uniform propeller velocity is about 15 percent lower than the test data

at $\pi D h/A_j$ of unity. It should be noted that if the radial variation of propeller velocity is considered better agreement is obtained, the calculated data in this case is about 10 percent less than the test data.

3.2 DUCT EFFICIENCY

3.2.1 Duct Losses

The duct loss factor has been calculated based on the data presented in Figures 25, 31 and 34 for the curved and straight ducts. This data is shown in Figure 40. The loss factor is shown to approach infinity as $\pi D h/A_j$ approaches

zero. This is caused by P_j becoming equal to P_t for zero flow conditions, and therefore this parameter cannot be used in this form for conditions which approach zero flow. At

larger values of $\pi D h/A_j$ the duct loss factor somewhat approaches the value for duct friction loss given in the literature such as References 1, 3, and 14. However, at $\pi D h/A_j$ of 2.5 the value of

k_2 is twice the value for long smooth duct friction. It is believed that a large portion of this discrepancy is caused by duct inlet losses.

3.2.2 Inlet Ring Performance

The analysis of Section 1.6.3 is now compared with the test data shown in Figures 27 and 39. As shown in Figure 27 the assumption of a linear variation of the inlet ring pressure, P_s , with inlet angle, θ_s , is good up to $\theta_s = 135^\circ$. For the evaluation of the inlet thrust, T_s , the portion of the inlet of $\theta_s > 135^\circ$ is only of minor importance. A value for $k_s = 2.25$, represented in Figure 27 as the straight line, is considered applicable. With this value of k_s , the variation of T_s/T_p vs. A_s/A_p , using Equation 1.6.3-6, has been computed and the result is shown in Figure 30. The theory is applicable up to A_s/A_p for which T_s/T_p is equal to unity. Beyond this A_s/A_p , T_s/T_p should be taken as unity. It is seen that this analysis agrees reasonably well with the available test data.

4.0 METHOD OF DESIGN OF PROPELLER AND DUCT SYSTEMS

In the design of an annular jet ground effect vehicle, it is necessary to establish the following parameters.

1. General Arrangement Parameters
 - a. Base Area, S
 - b. Gross Weight, W
 - c. Maximum Hovering Height, h_{max}
2. Annular Jet Parameters
 - a. Nozzle Area A_j , and Inclination, θ_n
 - b. Base Pressure, P_b
 - c. Nozzle Pressure, P_j
3. Duct Design
 - a. Propeller Area, A_p
 - b. Counterbody Area, A_{cb}
 - c. Inlet Area, A_i
 - d. Inlet Ring Area, A_s
 - e. Length, Curvature and Area Parameters
 - f. Struts and Protuberances
 - g. Vanes
 - h. Duct Efficiency, η_D
4. Propeller Design
 - a. Rotational Speed, Ω
 - b. Blade Parameters, θ_x, τ

In general, the parameters, S , W and h_{\max} will be given for the design of the propeller and duct system. The problem is then to establish the detail characteristics of propeller and ducts and to determine the required power. These parameters cannot be established until the annular jet requirements are defined. Methods for the design of these components are given in this section.

4.1 ANNULAR JET PARAMETERS

The required propeller and duct parameters depend on the flow requirements of the annular jet and therefore, these parameters must be established before the duct and propeller are considered.

The determination of the nozzle flow parameters is hampered by the lack of agreement of the existing theories. As noted in Section 2 the existing theories give an inaccurate prediction of the nozzle flow parameters. To determine the accuracy of the theory of Reference 6 in predicting overall performance, the calculated internal efficiency of the test units was evaluated, and the resulting data are shown in Figure 41. This efficiency is determined from the G_{eff}

data of Reference 6 as follows:

$$(\eta_i)_{\text{calc.}} = G_{\text{eff}} / Z$$

As noted previously in Section 2.1 the calculated internal efficiency of the straight duct configuration is about 70 percent as compared to the actually measured 78 percent. The maximum curved duct internal efficiency was measured as 68 percent and was fairly constant at this value between h/D of 0.1 and 0.2. From the data shown in Figure 41, the calculated internal efficiency is 52 percent at an h/D of 0.1 and decreases to 40 percent at an h/D of 0.2. This rather poor correlation of test data and theory results from the fact that the nozzle and base pressure prediction method is inaccurate.

The lack of agreement between theory and experimental data is of a magnitude which makes the theoretical determination of an optimum nozzle geometry of questionable value. However, the experimental nozzle flow and base pressure data are given in Figures 33 and 34 for the tested configurations which significantly differ only in the parameter A_j/S . It is seen from these figures that the effect of A_j/S is much smaller than the effect of $\pi D h/A_j$. This data can also be used to estimate the optimum value of A_j/S . This optimum can be estimated by use of the test data together with the following relations:

$$L = P_b A_b + P_j A_j + \rho A_j V_j^2 \quad (4.1-1)$$

$$= P_{tj} A_j \left[\frac{P_b}{P_{tj}} \left(\frac{S}{A_j} - 1 \right) + \left(2 - P_j/P_{tj} \right) \right] \quad (4.1-2)$$

$$P = \frac{1}{\eta_i} P_{ti} F \quad (4.1-3)$$

$$= \frac{1}{\eta_i} (P_{ti})^{3/2} A_j \sqrt{\frac{2}{\rho} (1 - P_j/P_{tj})} \quad (4.1-4)$$

Thus

$$\frac{L}{P} = \frac{\left[\frac{P_b}{P_{tj}} \left(\frac{S}{A_j} - 1 \right) + \left(2 - P_j/P_{tj} \right) \right]}{\frac{1}{\eta_i} \sqrt{P_{tj} \left(\frac{2}{\rho} \right) (1 - P_j/P_{tj})}} \quad (4.1-5)$$

Equation (4.1-5) can be solved for the lift-power ratio for various values of P_{tj} . For this comparison, however, the parameter L/S is of greater interest than P_{tj} . Equation (4.1-2) can be solved for P_{tj} for a given L/S and this value may be substituted for P_{tj} in Equation (4.1-5). This results in the following:

$$\frac{L}{P} = \frac{\eta_i \left[\frac{P_b}{P_{tj}} \left(\frac{S}{A_j} - 1 \right) + \left(2 - P_j/P_{tj} \right) \right]^{3/2}}{\sqrt{(L/S) \left(\frac{S}{A_j} \right)^{3/2} \rho (1 - P_j/P_{tj})}} \quad (4.1-6)$$

The measured values of P_b/P_{tj} and P_j/P_{tj} introduced into Equation 4.1-6, and by some extrapolation a plot of the ratio $L/\eta_i HP$ is obtained as a function of A_j/S for a given L/S and for various values of h/D . The results of these calculations are shown in Figure 42. As noted above in connection with the data shown in Figures 33 and 34, the effect of A_j/S is of a second order only. Hence, in calculating $L/\eta_i HP$ from Equation 4.1-6, the assumption has been made that the pressure data is a function of $\pi D h/A_j$ only. The curves shown in Figure 42 span the practical range of A_j/S and result in an $L/\eta_i HP$ variation that is similar to that of Reference 11.

Figure 42 indicates that ground effect machines designed to hover at an h/D of 0.2 should have nozzle area to base area ratios as large as 40 percent.

For GEMs designed to hover at values of h/D less than 0.2 the information shown in Figure 42 indicates that a smaller A_j/S is to be used for increased performance.

4.2 DUCT DESIGN

In the design of the duct system the available test data can be used for qualitative information, but for detailed quantitative results a model test approach or a very flexible prototype development program is warranted.

The design of the duct system requires consideration of many variables, including those which determine size, weight, noise, structural ruggedness, cost and of course, performance. For all of the above, but the performance considerations, rather small inlet and propeller areas are desirable. Additional investigations are required to determine whether large angle

diffusing such as discussed in Reference 15 can be used to provide small propellers and good overall performance. In the present program only constant area ducts were investigated.

The size of the centerbody to be used should be determined by weighing the effect of increased centerbody size on duct friction losses, duct weight and propeller performance. In general, it is believed that the propeller centerbody should be as small as possible.

Except for very small values of $\pi D^4/A_j$, the inlet ring geometry can significantly influence performance and, therefore, this geometry should be carefully selected. In the design of the inlet ring, aerodynamic performance is a major parameter. This is especially true with a diffusing duct system. For a very high performance vehicle, it is recommended that inlet conditions should be studied with a model of the duct system. This model could be connected at the nozzles to a plenum with an exhaust fan. This will provide air flow into the inlet without propeller distortions. Pressure measurements should be obtained to indicate the configuration with the least losses. The usual scale effect considerations such as discussed in Reference 1 must be made in determining the model size and evaluating the results.

The effects of length, curvature and duct area will probably be small for CEM duct configurations. These parameters mostly define skin friction losses which cause only a small portion of the overall losses. Curvatures which may cause separation should be minimized.

In the design of CEM ducts it is recommended that every effort be made to keep struts and protuberances out of the ducts. At the low Reynolds numbers which are encountered in CEM ducts, the drag of these struts is very large. In this regard the use of turning or anti-rotation vanes should be carefully evaluated. The drag losses should be studied and compared to the possible power saving which these vanes may produce.

1.2 PROPELLER DESIGN

The following general considerations should be made in the design of a propeller for a CEM:

1. Propellers should be located in the duct where uniform flow conditions are approached.
2. Blade twist and pitch setting should be chosen considering both the angle of attack for
 $(C_D/C_L^{1/2})$ minimum and the increasing angles of attack which may be caused by reduced operating height. Propeller blade twist and planform should be designed to cause uniform inflow.
3. Propeller tip speed should be as small as can be tolerated from propeller and drive cost and weight considerations. The upper limit to propeller tip speed is established by consideration of noise and drag divergence due to compressibility effects.
4. Propeller solidity should be large enough to produce the desired thrust. Once the propeller size and tip speed and the nozzle flow requirements are established, the method of calculating propeller performance given in Section 1 should be followed.

APPENDIX

THE TEST PROGRAM

1. SCOPE AND PURPOSE

The purpose of the test program was to provide the information necessary for the formulation of methods for improved duct and propeller design, with the object of obtaining more efficiently performing Ground Effect Machines.

2. DESCRIPTION OF TEST CONFIGURATIONS AND INSTRUMENTATION

A. Test Configurations

In order to determine the effect of various parameters affecting the performance and stability of ground effect machines, a number of parameters were varied for tests of three basic configurations. The test units consisted of a propeller, inlet ring, ducting and ground board.

The propeller characteristics are given in Table 1.

The ground board was used to simulate the ground; it consisted of a circular platform 9 feet in diameter. In order to record the lift reaction of the GEM duct test unit, the ground board was instrumented with three strain-gage beams. The distance from the ground board surface plane to the base of the test unit was variable to simulate changes in height. The ground board could also be inclined to simulate change in angle of pitch or roll of the test unit. Tests were performed with distances varying from 10 feet to 1/16 inch and at angles up to 15 degrees.

1.) Straight Duct Tests

Straight duct tests were performed with combinations of three duct sections:

- (a) Short straight duct (length = 54 in.)
- (b) Long inlet duct (length = 48 in.)
- (c) Nozzle extension duct (length = 27 in.)

Three inlet rings were tested which may be described as follows:

- (a) 1.5 inch radius semi-circular inlet ring
- (b) 4.5 inch radius semi-circular inlet ring
- (c) Quarter-elliptic inlet ring

Duct Sections

(a) Short Straight Duct

The short duct contained the drive unit and the propeller. The duct inside diameter was 2.9 feet. The propeller drive unit was contained within a cylindrical centerbody of radius equal to 8 inches. Figure 43 presents the dimensions of the duct.

(b) Long Inlet Duct

In order to investigate the effects of the change in inlet distance from the propeller, a long inlet duct was added to the short duct. This configuration is shown in Figure 44.

(c) Nozzle Extension Duct

In order to investigate the effects of the change in distance from the propeller to the nozzle, a nozzle extension duct was added to the short duct. This configuration is shown in Figure 45.

Inlet Rings

(a) 1.5 inch Semi-Circular Inlet Ring

This inlet ring was circular with an inside diameter of 2.9 feet to match the diameter of the duct system. The inlet ring was semi-circular with a radius of curvature of 1.5 inch.

(b) 4.5 inch Semi-Circular Inlet Ring

The construction of this ring is similar to the 1.5 inch ring, except the ring radius of curvature was 4.5 inches.

(c) Quarter Elliptic Inlet Ring

The shape of this inlet ring can be approximated by assuming it to be a quarter of an ellipse whose equation is,

$$\frac{x^2}{28.6} + \frac{y^2}{52.3} = 1$$

where x and y are in inches. Figure 46 shows the geometry of the inlet ring, and the coordinates are given in Table 2.

The short duct with the three inlet rings are shown in Figures 47, 48, and 49.

The base of the test unit consisted of the centerbody base for the straight duct system. For a series of tests, a base of larger area was added to the existing centerbody at the nozzle.

Geometric parameters of the straight duct are given in Table 3.

2.) Curved Duct Tests

The curved duct tests were performed with the three inlet rings as described in the straight duct section. The duct centerbody contained the propeller and drive unit. The curved duct inlet was located 90 degrees from the nozzle. The duct and centerbody were designed as circular cross-sections of constant flow area (5.21 sq. ft.) distributed along an elliptical centerline. The coordinates of the outer wall, centerbody, and centerline are given in Tables 4 and 5. Geometric parameters of the curved duct are given in Table 3 and also in Figure 46. A general test set-up of the curved duct with the 4.5 inch inlet ring is shown in Figure 50.

A number of modifications were made on the curved duct in order to improve the flow in the duct. In particular, the modifications consisted of making the flow follow the duct at the place where the curvature was the greatest. (Flow separation occurred at that place in the duct). This place corresponds to an azimuth angle of zero as seen on Figure 51.

One modification consisted of adding a guide vane to the duct, located 6 inches behind the propeller, extending from $\psi = 300$ degrees to $\psi = 60$ degrees. The guide vane

curvature was the same as the outer wall, and had a chord equal to 6 inches. The vane was placed 3 inches radially from the outer wall. The guide vane is shown installed in the duct in Figure 52.

Another modification to achieve better flow in the duct was the addition of a streamlined body to the curved duct in place of the guide vane. The shape of the streamlined body was that of a symmetrical airfoil whose chord was placed along the zero azimuth line. The maximum body thickness was 6 inches and the chord was 18 inches. The span extended from the centerbody to the outer wall.

In order to obtain the effect of placing various objects such as control vanes, structure, fuel tanks, and compartments in the ducts of a GEM, two sizes of control plugs were placed in the nozzle of the curved duct test unit at various azimuth positions. The two control plugs were semi-circular with a length of 3 inches and 27 inches, respectively.

3.) Curved Duct Tests with Plenum Chamber

This test configuration consisted of the following:

- (a) Short straight duct containing the propeller and drive unit.
- (b) Quarter elliptic inlet ring on the short duct.
- (c) Plenum or settling chamber 10 feet high, 10 feet wide and 5 feet in length in the direction of the flow.
- (d) Curved duct section with a 4.5 inch inlet ring protruding into the plenum chamber.

The plenum chamber configuration was used to study the effects of a propeller located at a great distance from the curved duct section, and the effect of the flow in the curved duct without the effects of the propeller. The test set-up is shown in Figures 53 and 54. Figure 53 shows the plenum chamber with the straight duct and elliptic inlet ring, and Figure 54 shows the base of the curved duct section along with the ground board.

B. Instrumentation

Pressure data was obtained at various stations throughout the test unit. Pressure probes and rakes sensed total and static pressure. The probes were connected by plastic tubing to 4 banks of multiple tube manometers. The pressure data was recorded at the following locations:

(a) Inlet Ring

Static pressures were measured (at four azimuth positions) along the surface of the inlet ring.

(b) Inlet Nose Pressures

Static pressures were measured along the nose surface at two azimuth positions.

(c) Duct Pressures

Static and total pressures were measured at various azimuthal and radial positions at various lengths along the duct from the propeller plane. Surface duct static pressures were measured along the duct wall and along the centerbody. During certain tests, a calibrated pressure probe was used to obtain data concerning the propeller swirl angle.

(d) Base Pressures

The base of the centerbody was instrumented to sense azimuthal and radial variation of pressures.

(e) Ground Board Pressures

Ground board static pressures were recorded at various radial positions.

(f) Pressure Surveys

The flow pattern near the inlet and also near the exit nozzle was studied by recording total and static pressures at various azimuthal and radial positions.

A hot wire anemometer was also used to obtain velocities at various stations in the duct and nozzle.

Propeller thrust was read from a microammeter - strain-gage combination.

Propeller torque was read from the microammeter which was connected through slip rings on the propeller shaft.

Propeller rpm was read by means of a magnetic pickup which sensed the passage of gears on the propeller shaft.

Double instrumentation was used to obtain reliable data.

Propeller torque was also read by using a calibrated hydraulic pressure gage mounted on the drive unit hydraulic line. A stroboscope was used to obtain a double check on the propeller rpm. The accuracy of measurement using the double instrumentation is given in Section 5, along with examples of independently measured test data.

The ground board had three strain gages to sense loads. From these loads, moments and center of pressure could be calculated.

3. SUMMARY OF TESTS

Tables have been prepared which present a summary of tests performed along with the data recorded, test configuration and purpose of test. These tables are available upon request. The following parameters were varied during the testing; configuration, disc loading, ground board height, and ground board tilt.

4. DISCUSSION OF TEST RESULTS

In order to evaluate the performance and control of ground effect machines, certain parameters are needed. The following sections present methods of calculating the important parameters.

The following data was reduced from the recorded data, propeller thrust T_p , total lift L (total ground board reaction), propeller rpm N , and propeller torque Q .

Calculation of Internal Efficiency, η_i

The internal efficiency is an important measure of the aerodynamic losses in the duct system. The internal efficiency

is defined as the ratio of the air horsepower at the nozzle exit to the propeller shaft input .

$$\eta_i = \frac{AHP}{HP} = \frac{\text{Jet Air Horsepower}}{\text{Input Shaft Horsepower}} \quad (1)$$

The jet air horsepower is calculated from the following equation:

$$AHP = \frac{F_j P_{tj}}{550} \quad (F_j = \text{Volume Flow at Exit}) \quad (2)$$

The actual calculation was accomplished by a numerical integration of the product of the area, total pressure, and velocity over the jet annular at the nozzle. Total pressure was obtained directly from the pressure data at the nozzle. Velocities were calculated from the static and total pressures using the Bernoulli equation.

$$P_{tj} = P_j = \frac{1}{2} \rho V_j^2 \quad (3)$$

Solving for velocity

$$V_j = \sqrt{\frac{2}{\rho} (P_{tj} - P_j)} \quad (4)$$

Using equation (4) and the differential equation form of (2) the equation to be solved by numerical integration is:

$$AHP = \frac{2\pi}{550} \int_{R_i}^R \sqrt{\frac{2}{\rho} (P_{tj} - P_j)} P_{tj} r dr \quad (5)$$

The propeller shaft input horsepower is calculated from:

$$HP = \frac{Q \cdot \Omega}{550} \quad \left(HP = \frac{Q(N)}{63,000}, \text{ For the case of the test units} \right) \quad (6)$$

Volume Flow, F (ft³/Sec.)

Volume flow is calculated by a numerical integration of the velocity over the annular duct area. The velocities are calculated from equation (4). The density is corrected for

air duct temperature.

$$F = VA$$

$$F = 2\pi \int_{R_H}^R \sqrt{\frac{2}{\rho} (P_t - P_s)} r dr \quad (7)$$

An average jet velocity \bar{V}_j used in the analysis will be defined as:

$$\bar{V}_j = F_j / A_j \quad (8)$$

Power loading (L/HP) is obtained by dividing total lift L , by shaft horsepower HP . Total base area loading L/S is obtained by dividing total lift by base plus nozzle area, S .

Jet Momentum

The momentum of the jet is calculated by,

$$T_j = m_j \bar{V}_j$$

where m is the mass flow at the jet

$$m_j = \rho A_j \bar{V}_j \quad \bar{V}_j = \sqrt{\frac{2}{\rho} (P_{tj} - P_j)}$$

A graphical integration of the mass flow and pressures was used to calculate jet momentum.

$$T_j = 4\pi \int_{R_H}^R (P_{tj} - P_j) r dr \quad (9)$$

The augmentation factor which is shown in Figure 36 is defined as the total lift, divided by the jet momentum. Inlet ring thrust, T_s , was obtained by a numerical integration of the axial component of the static pressure times the wetted area of the inlet ring.

Average nozzle total pressure, P_{tj} , was obtained by a numerical integration of the nozzle total pressure over the

nozzle annular divided by the nozzle area

$$P_{tj} = \frac{\int_{R_H}^R 2\pi r (P_{tj}) dr}{\pi (R^2 - R_H^2)} \quad (10)$$

This average jet total pressure is the parameter used in P_b/P_{tj} of figure 33.

An arithmetic average was used for base pressure P_b . The variation of base pressure with angle of pitch and roll angle for the curved duct is shown in Figure 12.

5. ACCURACY OF MEASUREMENTS

The accuracy of measurement of parameters can be demonstrated by giving examples of data in the following table.

Accuracy of Measurements									
Parameter Measured	Means of Measurement	Test No. 11	12	13	14	Percent Difference of Two Measurements			
Propeller Torque	Microammeter Hydraulic Gage	267	209	150	104	3.7	1.4	1.0	2
		257	206	149	101				
Propeller RPM	Voltmeter Stroboscope	3300	3300	2800	2350	2.5	5.7	6.6	3
		3900	3500	3000	2500				

Propeller torque was measured with differences of less than 4 percent as shown from the tests of the above table. Propeller rpm was measured within 3 percent. The above tests represented a sample of the 217 tests performed, but a calculation of the differences was not greater than these reported above. Propeller thrust measurement was read on a millivoltmeter with a scale of 44 pound per millivolt. Due to unsteady flow conditions, the reading was accurate to ± 1 mv or a total of 3 pounds. This represents an accuracy of 11 percent for the 3.6 psf disc loading and 3 percent for the 14 psf disc loading.

The accuracy of the pressure data was dependent on the degree of steadiness of the liquid in the manometer tubes. Flow conditions within the duct test unit were of a nature that gave readings of ± 0.05 inch, which represents a difference in pressure of ± 0.22 psf for $T_p/A_p = 16$ psf. Flow conditions at the duct exit, however, were more unsteady giving readings of ± 0.3 inch or ± 1.3 psf. The nozzle pressure maximum and minimum values were recorded in order that a good average value could be obtained.

A sphere type yawhead probe was used to obtain swirl angles behind the propeller. A calibrated pressure rake was also used to obtain swirl angle at 3 radial distances in the duct. This rake was calibrated at the wind tunnel facility of Princeton University. The calibrations are given in Figures 55 and 56. From Figure 56, probe indicated dynamic pressure is essentially equal to the actual dynamic pressure for angles of yaw between ± 30 degrees. Since the swirl angles for the tests performed were not above 30 degrees, there was no need for the recorded pressures to be corrected for swirl angle.

One method of determining the overall accuracy of measurements consists of summing the individual components of the duct thrust and comparing this sum with the measured ground board reaction of total lift, L . The individual thrusts consist of base thrust ($A_b P_b$), and jet reaction, $(A_j P_j + m_j V_j)$.

In addition, the individual thrusts may be given as base thrust

($A_b P_b$), shroud thrust T_s , and propeller thrust T_p .

Figure 57 presents the summation of the individual thrusts divided by the total lift for the straight duct and curved duct

test configurations vs. h/D . Theoretically, neglecting friction

losses, the summation of the individual thrusts should be equal to the total lift. Deviation from this equality represent the accuracy of measurement. Test points using the values of shroud and propeller thrust are shown to have greater difference from the theoretical value of unity than test points which use base thrust and nozzle thrust. This is believed to be due, in part to the fact that the value of shroud thrust was not directly recorded, but was obtained from an integration of pressure obtained on the inlet ring.

REFERENCES

1. Pope, A., Wind-Tunnel Testing, John Wiley and Sons, New York, 1954.
2. Hoerner, I. S., Fluid-Dynamic Drag, published by the author, 1958.
3. Baumeister, Jr., T., Fans, McGraw-Hill Book Company, Inc., New York 1935.
4. Rawlings, W. L., and Swiveno, D. H., State-of-the-Art Summary Air-Cushion Vehicles, Revision 1, Prepared by Aeronutronics, U. S. Army Transportation Research Command Report 61-108, August 1961.
5. Pinnes, R. W., The Propulsion Aspects of Ground Effect Machines, IAS Preprint Paper No. 60-13, January 1960.
6. Carmichael, B. H., et. al., State of the Art Summary Air-Cushion Vehicles, Aeronutronics Division of Ford Motor Company, Report No. U-926, June 1960.
7. Anonomous, Results of Full-Scale Air Flow Tests of the Gyrodyne Model 55 Annular Jet Type of Ground Effect Machine, Gyrodyne Company of America, Report No. X55-313310-2, June 1961.
8. Ehrich, F., F., The Curtain Jet, Published in the Journal of the Aerospace Sciences, Volume 28, Number 11, November 1961.
9. Jones, R. S., Some Design Problems of Hovercraft, Saunders-Roe Division, I.A.S. Preprint No. 61-45, January 1961.
10. Sweeny, T. E., and Nixon, W. B., Preliminary Flight Experiments with the Princeton University Twenty-Foot Ground Effect Machine, Department of Aeronautical Engineering Princeton University Report No. 506, January 1960.
11. Goodson, K. W., and Otis, J. H., Effect of Ratio of Jet Area to Total Area and of Pressure Ratio on Lift Augmentation of Annular Jets In Ground Effect Under Static Conditions, NASA TN D-720, March 1961.

12. Carpenter, P. J., Lift and Profile-Drag Characteristics of an NACA 0012 Airfoil Section as Derived From Measured Helicopter-Rotor Hovering Performance, NACA TN 4357, September 1958.
13. Gessow, A., and Myers, G. C., Jr., Aerodynamics of the Helicopter, Macmillan Company, New York, 1952.
14. Marks, L. S., Mechanical Engineers' Handbook, McGraw-Hill Book Company, Inc., New York, 1951.
15. Kline, S. J., On the Nature of Stall, paper published in the Journal of Basic Engineering, Volume 81, Series D, September 1959.
16. Anon., Comparative Performance Charts for Ducted Propellers, Hiller Aircraft Corporation, Report No. ARD-257, ASTIA No. 241376, March 1960.

TABLE 1

PROPELLER CHARACTERISTICS

Number of Blades, b	4 Blades
Outer Radius, R	1.45 ft.
Hub Radius, R_H	0.67 ft.
Blade Chord, c	3.0 inches
Blade Pitch, θ_b	16.5 degrees
Blade Twist, θ_1	0.0 degrees
Blade Tip to Duct Clearance, B	0.040 inches
Maximum Design Propeller Thrust, T_p	10% lb.
Maximum Propeller Disc Loading, T_p/A_p	20 PSF
Planform	Rectangular

TABLE 2

CO-ORDINATES OF THE QUARTER ELLIPTIC INLET RING

STATION	RADIAL DISTANCE FROM ϕ OF ROTATION TO THE SURFACE OF THE INLET RING
12.00	17.4
17.36	17.4
18.37	17.7
19.33	17.9
20.26	18.2
21.20	18.54
22.02	19.10
22.76	29.83
23.35	20.59
23.79	21.51
24.00	22.38

TABLE 3
GEM-DUCT-TEST UNIT GEOMETRIC PARAMETERS

STRAIGHT DUCT

Centerbody to Outer wall Radius Ratio, $\frac{R_H}{R}$ *	0.46
Length from Propeller Plane to Duct Exit Plane,	53.0 inches
Duct Cross Sectional Flow Area, A_p	5.21 square feet
**Base Area, A_b	1.39 square feet
Nozzle Exit Area, A_j	1.39 square feet
Total Base plus Jet Area, S	6.6 square feet

* R = Propeller radius, but since tip clearance is 0.04 inches the wall radius is approximately equal to R

** Large Base area was 3.69 square feet

CURVED DUCT

Centerbody to Outer Wall Radius Ratio at Propeller, $\frac{R_H}{R}$	0.46
Duct Curvature, θ	90 degrees
Duct Cross Sectional Flow Area, A_p	5.21 square feet
Base Area, A_b	10.69 square feet
Total Base plus Jet Area, S	15.9 square feet
Nozzle Outside Diameter, D	4.5 ft.

TABLE 4

RADIUS OF SECTIONS OF THE OUTER WALL AND
THE CENTERBODY OF THE CURVED DUCT

All Sections Are Taken Along Station Lines.
All Sections are Circular.
The Centers of all Sections at all Stations
are located on the centerline of the
Duct Centerbody.

Radius of Section (inches)		
Station	Centerbody	Outer Wall of Duct
12.0	8.00	17.40
10.0	8.00	17.40
8.0	8.00	17.40
6.0	8.00	17.40
4.0	8.05	17.50
2.0	8.20	17.60
0	8.60	17.65
10°	10.75	19.10
20°	13.60	20.80
25°	14.60	21.60
30°	15.55	22.30
40°	17.60	23.80
50°	19.30	24.90
55°	19.90	25.30
60°	20.50	25.70
70°	21.10	26.50
80°	21.70	27.00
90°	22.10	27.60

TABLE 5

CO-ORDINATES OF THE ELLIPTICAL CENTER LINE OF
THE CENTERBODY OF THE CURVED DUCT

The Center of the Ellipse is at The
Intersection of Station Line 0
and Station Line 90°

Station Line	Distance From The Center of The Ellipse Measured Along Station Lines, (Inches)
0	38.40
10°	38.50
20°	38.90
30°	39.56
40°	40.48
50°	41.40
60°	42.28
70°	43.80
80°	43.88
90°	44.10

TABLE 6
SUMMARY OF CONFIGURATIONS AND TESTS PERFORMED

CONFIGURATION	SYMBOL	PURPOSE OF TEST	TEST UNIT
Short Duct, 4.5 In. Inlet Ring	◇	Out of Ground Effect Performance	Straight Duct
Short Duct plus Long Inlet Duct, 4.5 In. Inlet Ring	□ □	Out of Ground Effect Performance	
Short Duct, 4.5 In. Inlet Ring	◇	Effect of Disc Loading in Ground Effect	
Short Duct, 4.5 In. Inlet Ring	◇	Effect of Angle of Attack on Performance	
Short Duct Plus Nozzle Extension Duct, 4.5 In. Inlet Ring	△	Effect of Angle of Attack on Performance	
Short Duct Plus Large Base 4.5 In. Inlet Ring	⊙	Effect of h/D on Performance	
Short Duct, 1.5 In. Inlet Ring	○	Effect of h/D on Performance	
Short Duct Plus Long Inlet Duct, 4.5 In. Inlet Ring	△	Effect of h/D on Performance	
Short Duct Plus Nozzle Extension Duct, Quarter Elliptic Inlet Ring	⊠	Obtain Pressure Data	
Short Duct, 4.5 In. Inlet Ring	◇	Obtain Pressure Data	
4.5 In. Inlet Ring	►	Effect of h/D on Performance	Curved Duct
Quarter Elliptic Inlet Ring	★	Effect of h/D on Performance	
Quarter Elliptic Inlet Ring	★	Effect of Disc Loading on Performance	

CONFIGURATION	SYMBOL	PURPOSE OF TEST	TEST UNIT
Quarter Elliptic Inlet Ring	★	Effect of Angle of Attack on Performance	Curved Duct
Quarter Elliptic Inlet Ring	★	Effect of Roll Angle on Performance	
1.5 In. Inlet Ring	●	Effect of Modification on Performance	
Quarter Elliptic Inlet Rings Guide Vane Installed in Duct	▲		
4.5 In. Inlet Ring, Guide Vane Installed in Duct	●		
Quarter Elliptic Ring Streamlined Body Installed in Duct with Ground Board Extension and Fillett in Duct	✕		
4.5 In. Inlet Ring, Streamlined Body Installed in Duct	◆		
Quarter Elliptic Inlet Ring 3 In. Control plug Installed in Nozzle	▲	Effect of Control Plug on Performance	
4.5 In. Inlet Ring, 27 In. Control Plug Installed in Nozzle	▲	Effect of Control Plug on Performance	
Quarter Elliptic Inlet Ring	★	Effect of h/b on Performance	
4.5 In. Inlet Ring	▶	Obtain Pressure Data	
4.5 In. Inlet on Curved Duct	▲	Effect of Plenum Chamber on Performance	Curved Duct with Plenum Chamber
4.5 In. Inlet With Ground Board Side Plate	●	Effect of Plenum Chamber on Performance	Curved Duct with Plenum Chamber

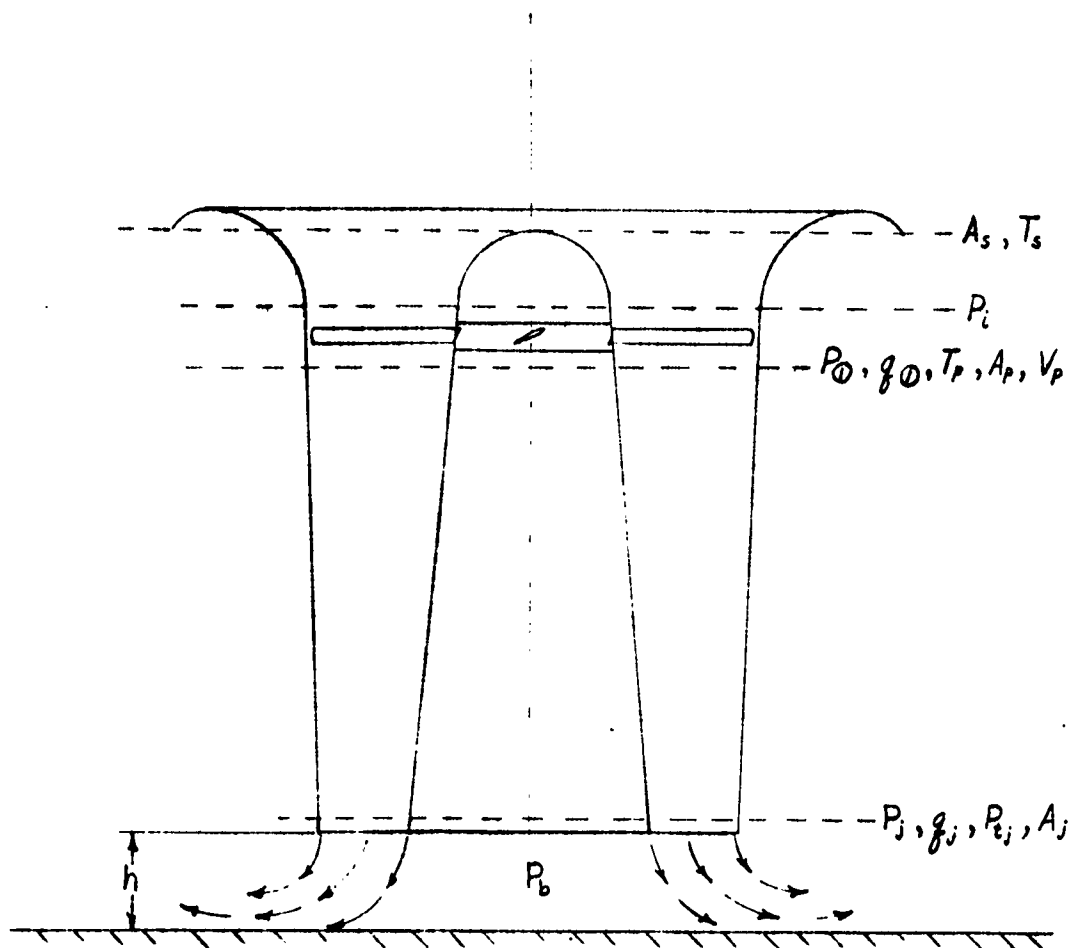


FIGURE 1: NOTATION USED IN THE ANALYSIS OF THE ANNULAR JET

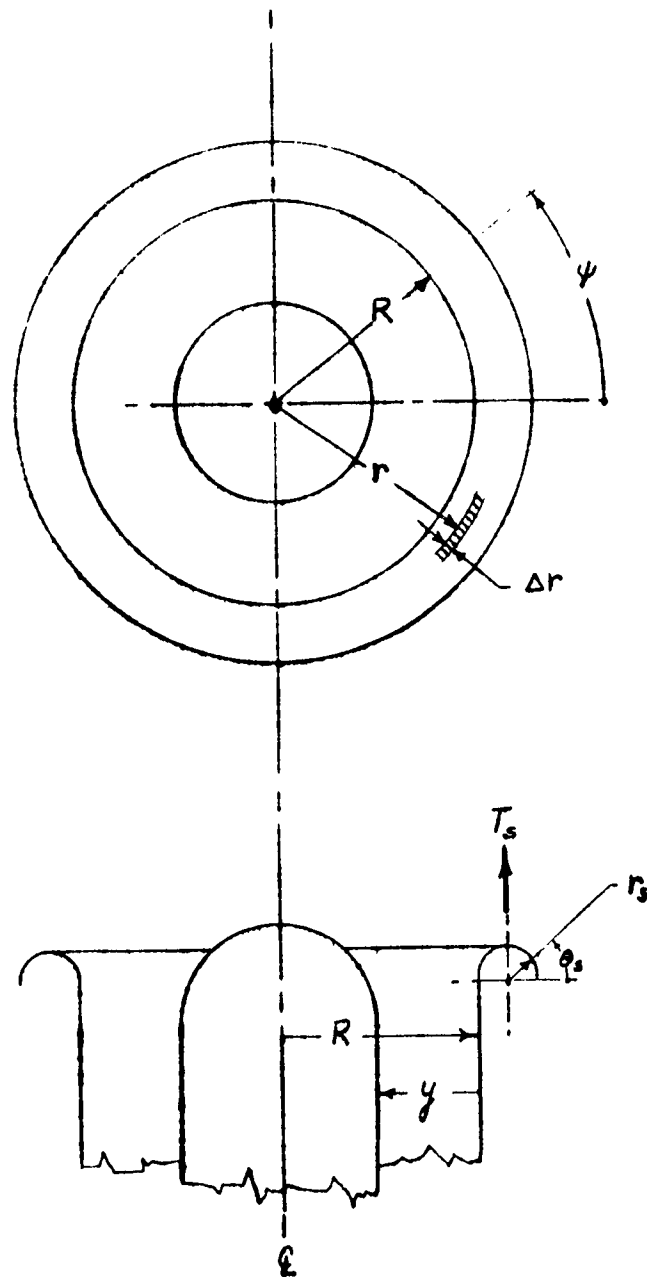


FIGURE 2: NOTATION FOR INLET GEOMETRY

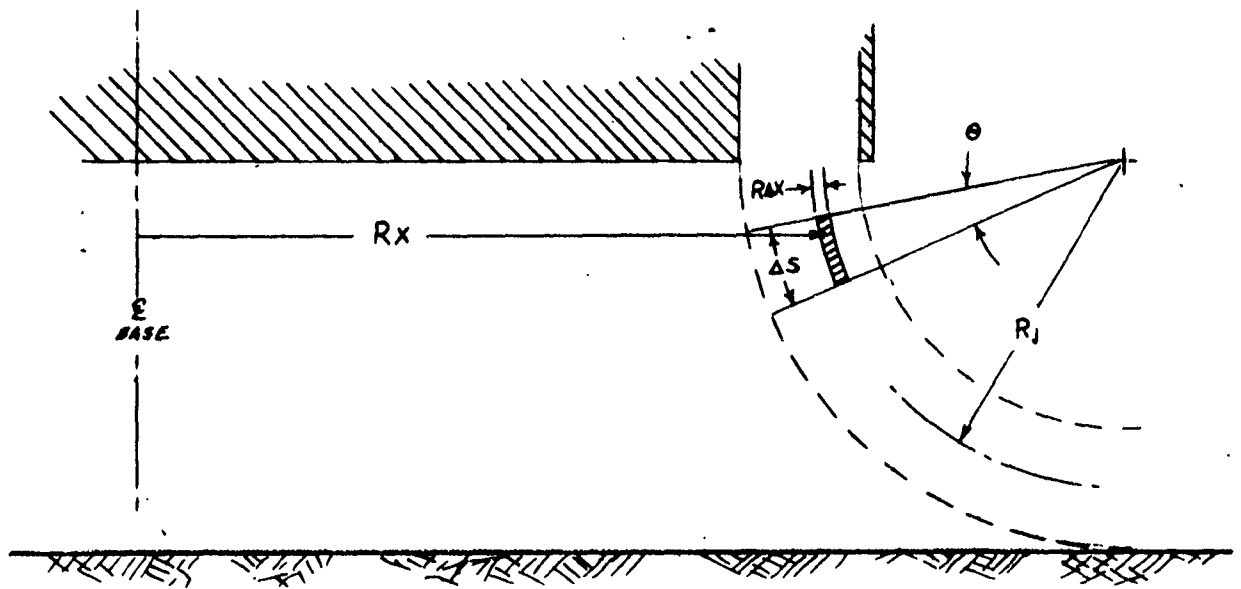


FIGURE 3: NOTATION FOR NOZZLE GEOMETRY

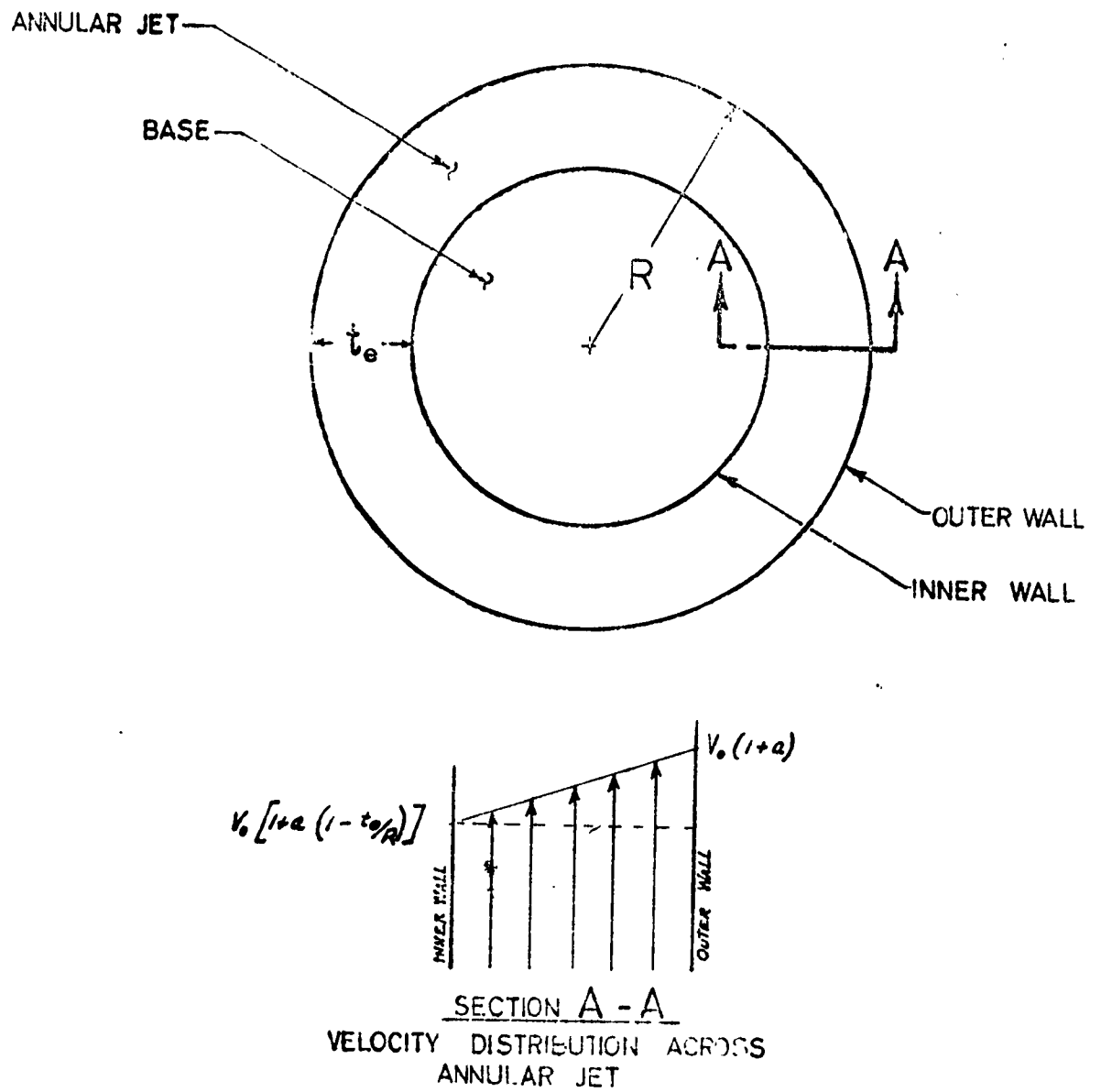


FIGURE 4: DEFINITION OF NOTATION

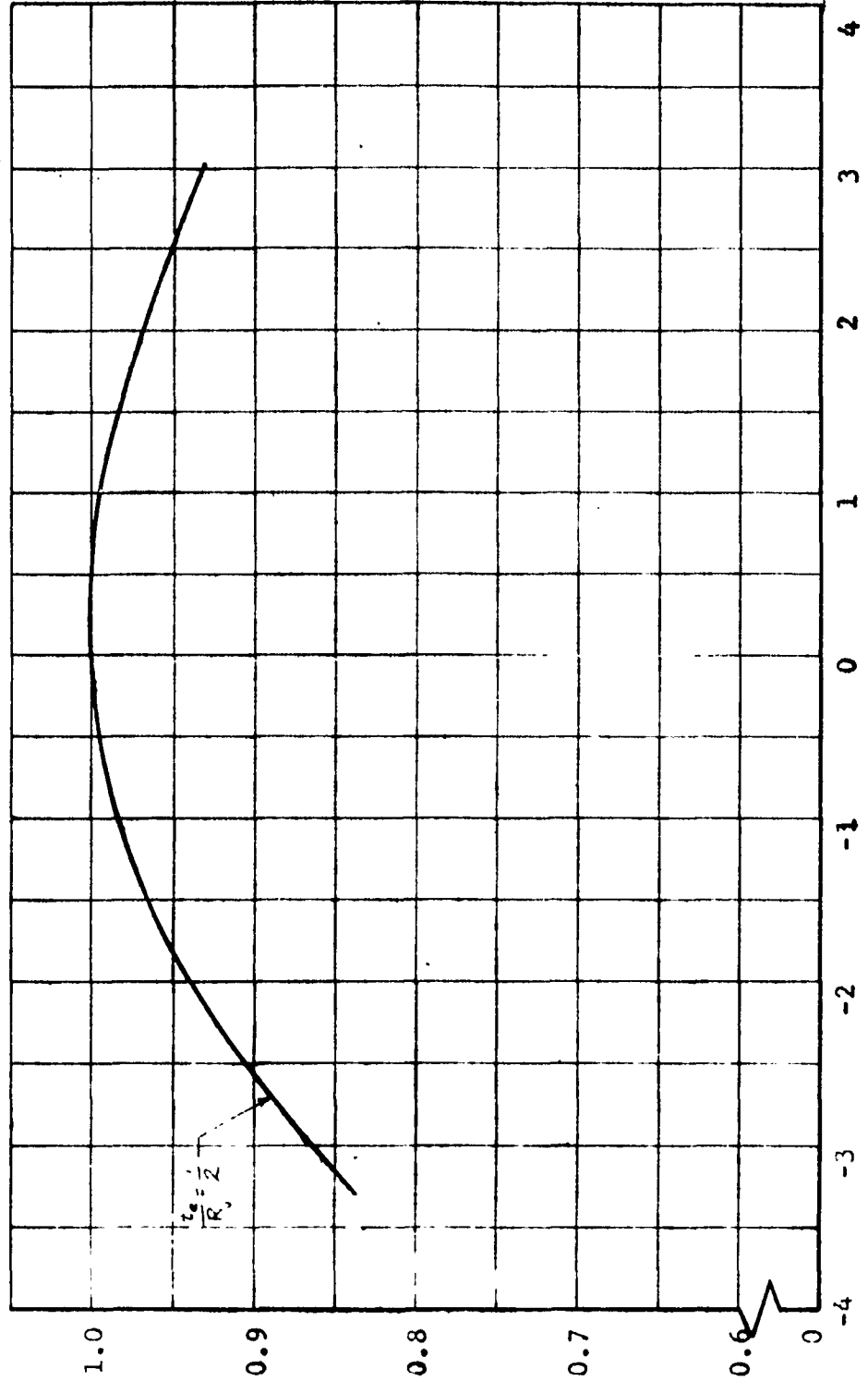
Notes:

Velocity Distribution; $V_x = V_o (1 + ax)$

$a V_o / V_A = 2.8$ the Velocity at the Nozzle
Inner Edge is Zero

$a V_o / V_A = -3.3$ the Velocity at the Nozzle
Outer Edge is Zero

Total Lift Divided by Lift Obtained by Constant Velocity
Distribution, L/L_A



Normalized, Non-Dimensional Slope of the Nozzle Velocity Distribution, $a V_o / V_A$

FIGURE 5: LIFT PERFORMANCE OF AN ANNULAR JET AS EFFECTED BY NOZZLE VELOCITY DISTRIBUTION

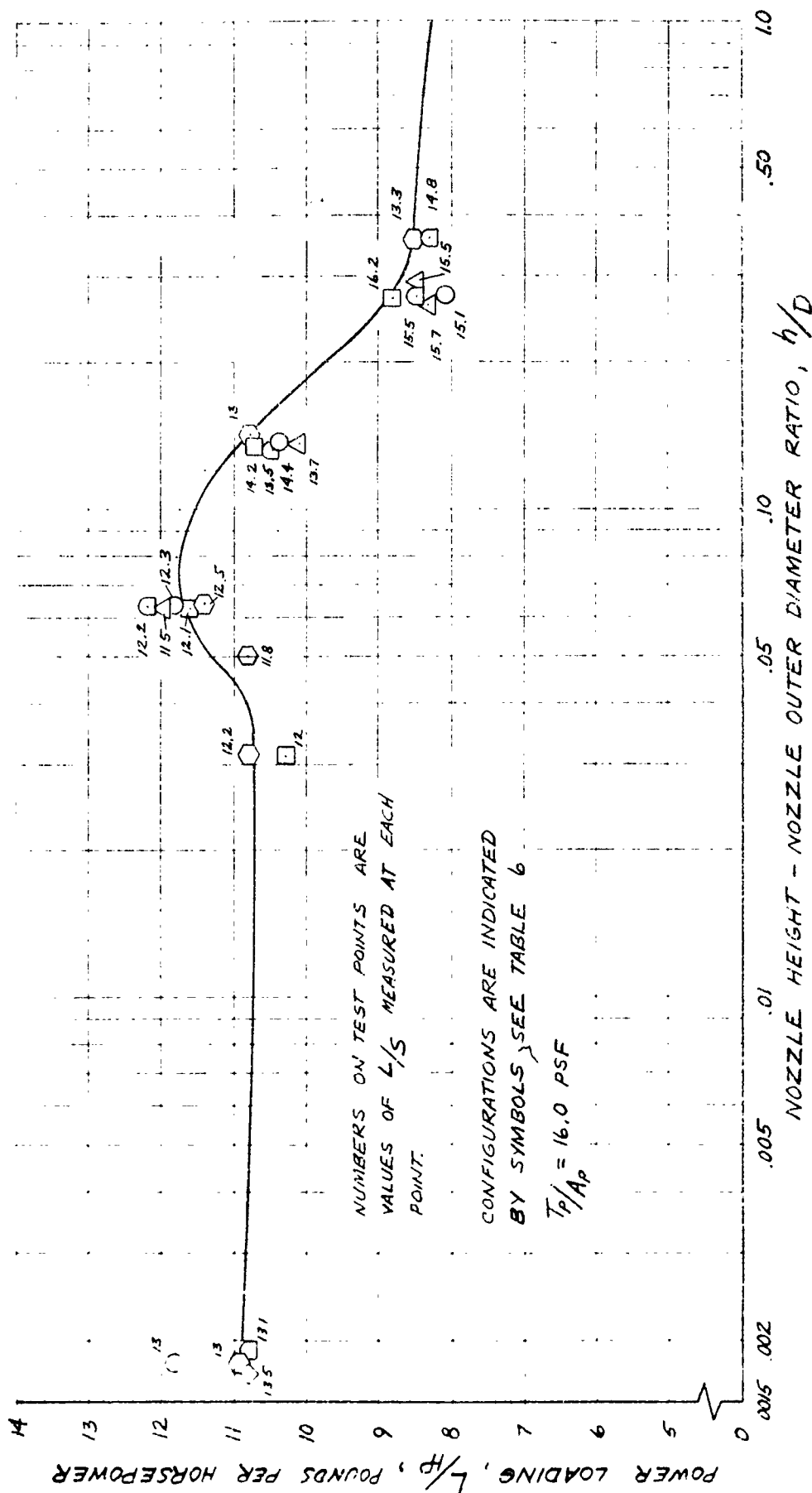


FIGURE 6: PERFORMANCE OF VARIOUS STRAIGHT DUCT TEST CONFIGURATIONS AT CONSTANT PROPELLER DISC LOADING

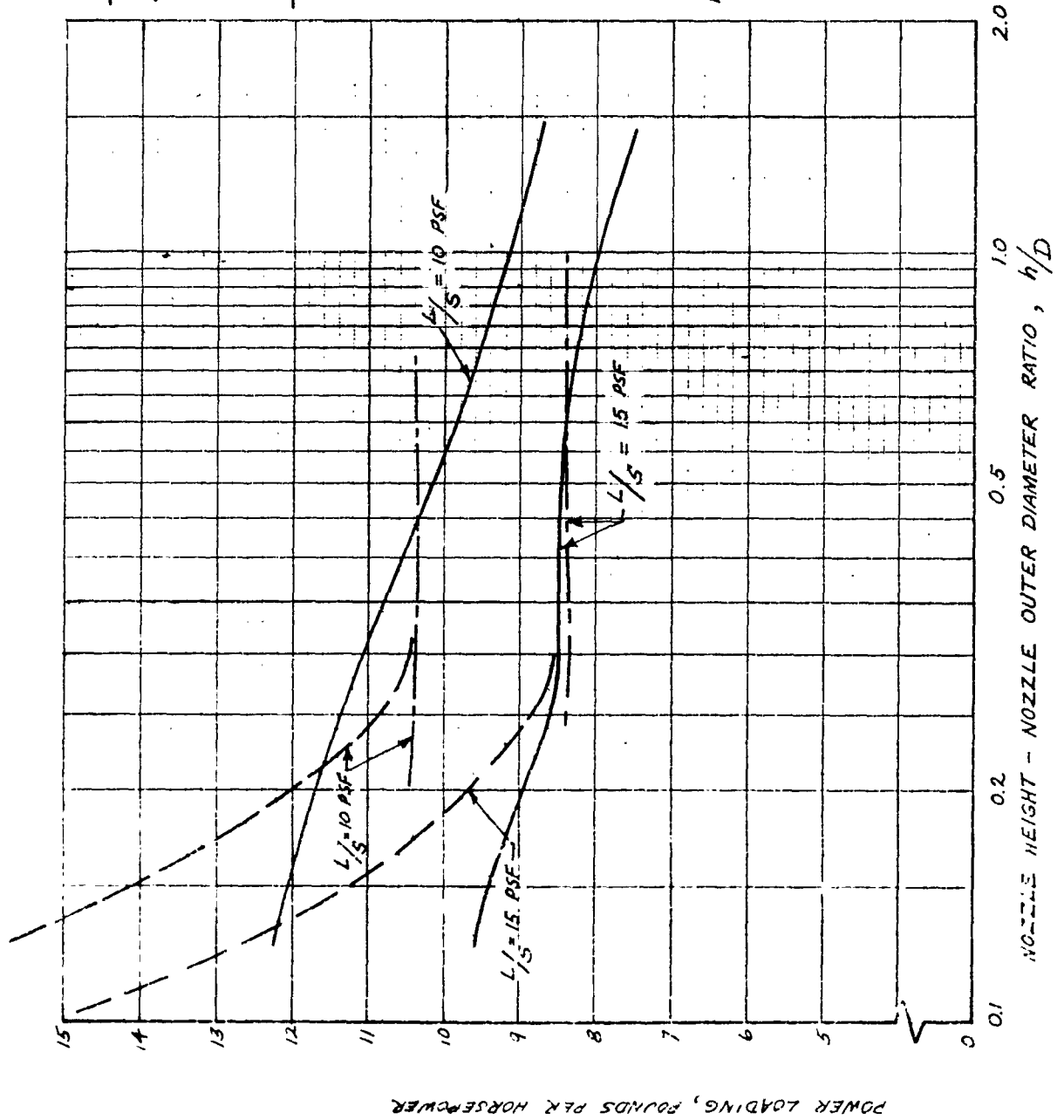


FIGURE 7: PERFORMANCE OF STRAIGHT DUCT TEST UNIT WITH COMPARATIVE CALCULATED PERFORMANCE

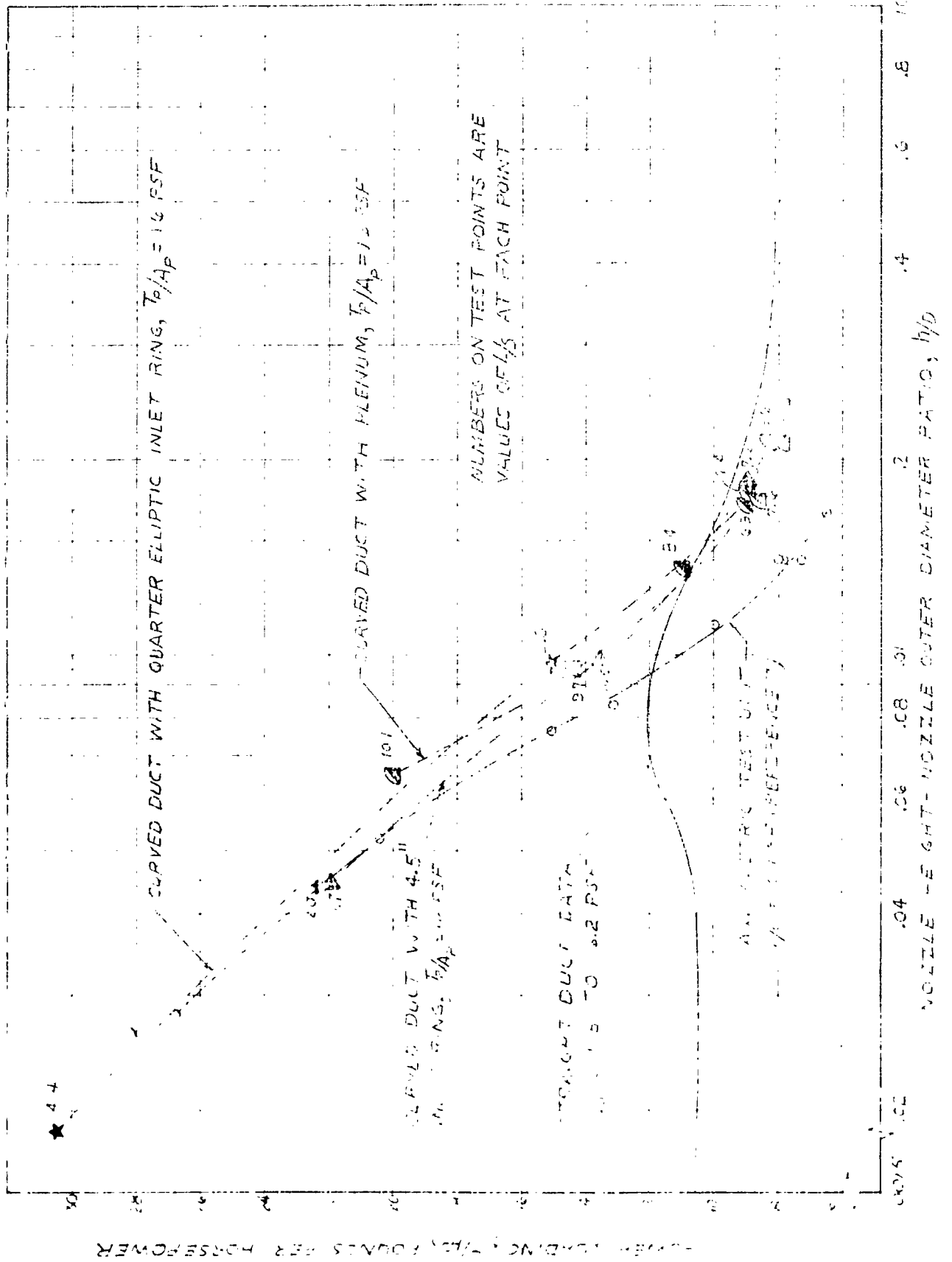


FIGURE 3: PERFORMANCE OF CURVED DUCT CONFIGURATIONS WITH COMPARATIVE STRAIGHT

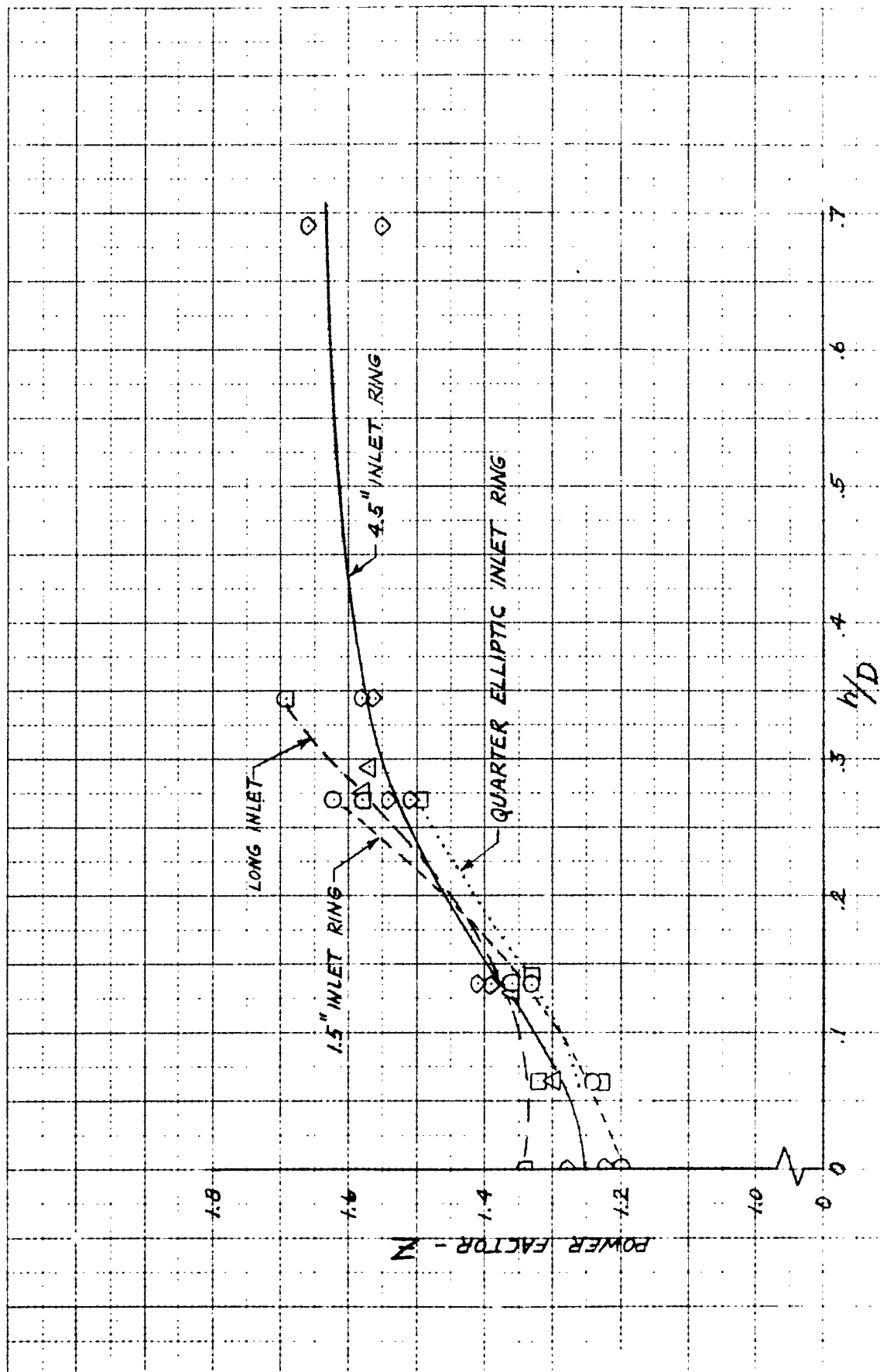


FIGURE 9: PERFORMANCE OF STRAIGHT DUCT TEST UNIT WITH VARIOUS INLET CONFIGURATIONS.

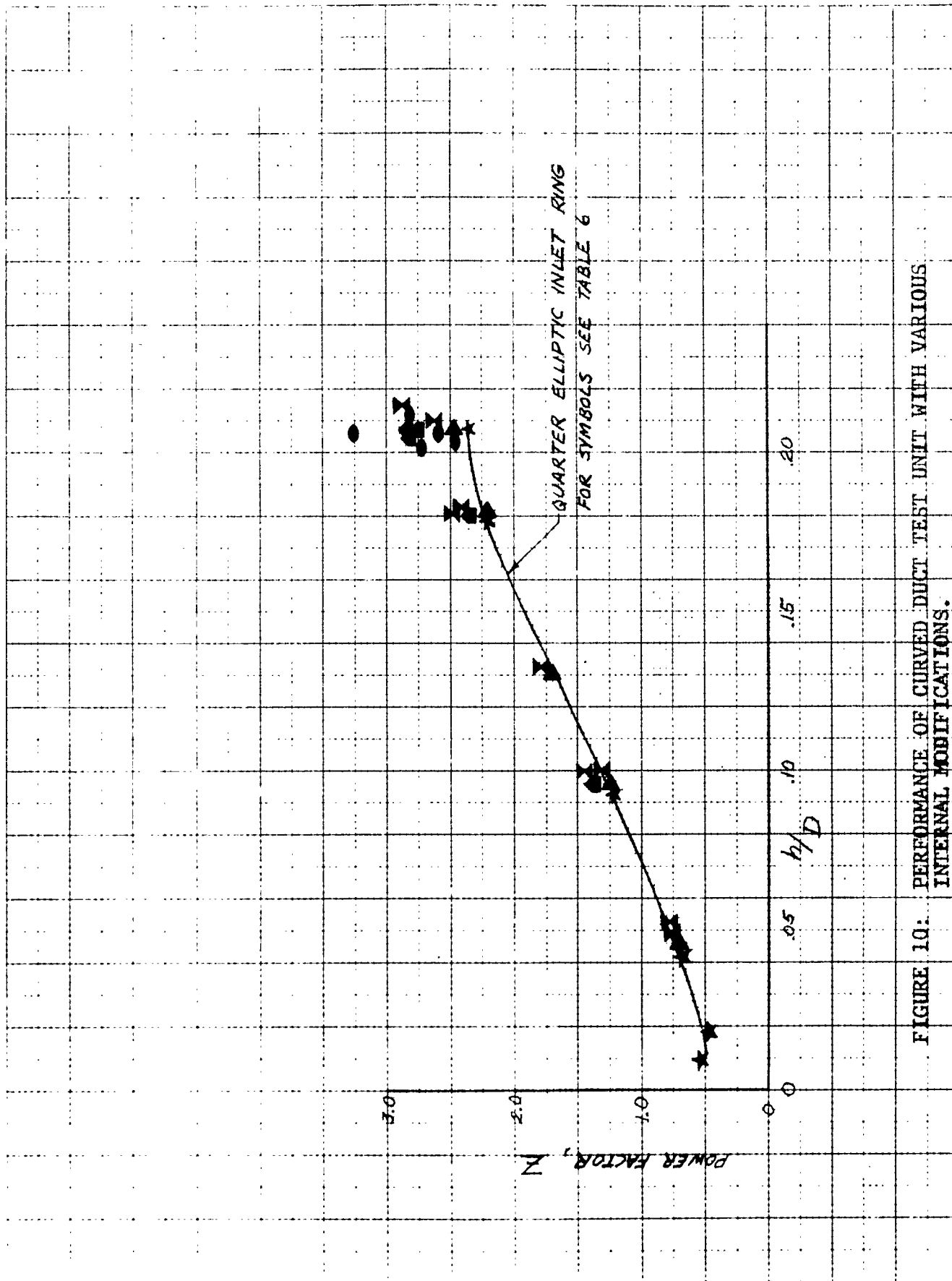


FIGURE 10. PERFORMANCE OF CURVED DUCT TEST UNIT WITH VARIOUS INTERNAL MODIFICATIONS.

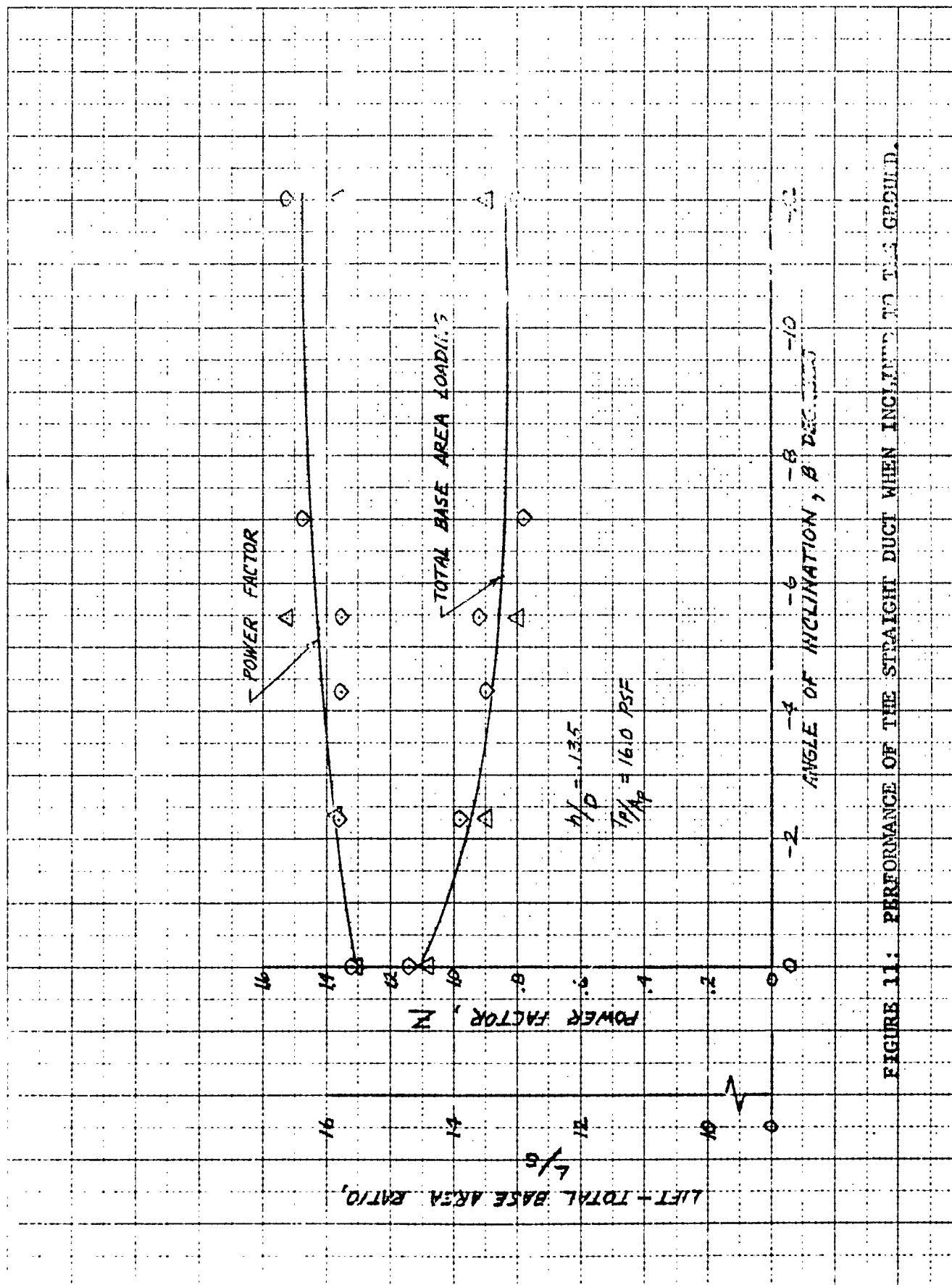


FIGURE 11: PERFORMANCE OF THE STRAIGHT DUCT WHEN INCLINED TO THE GROUND.

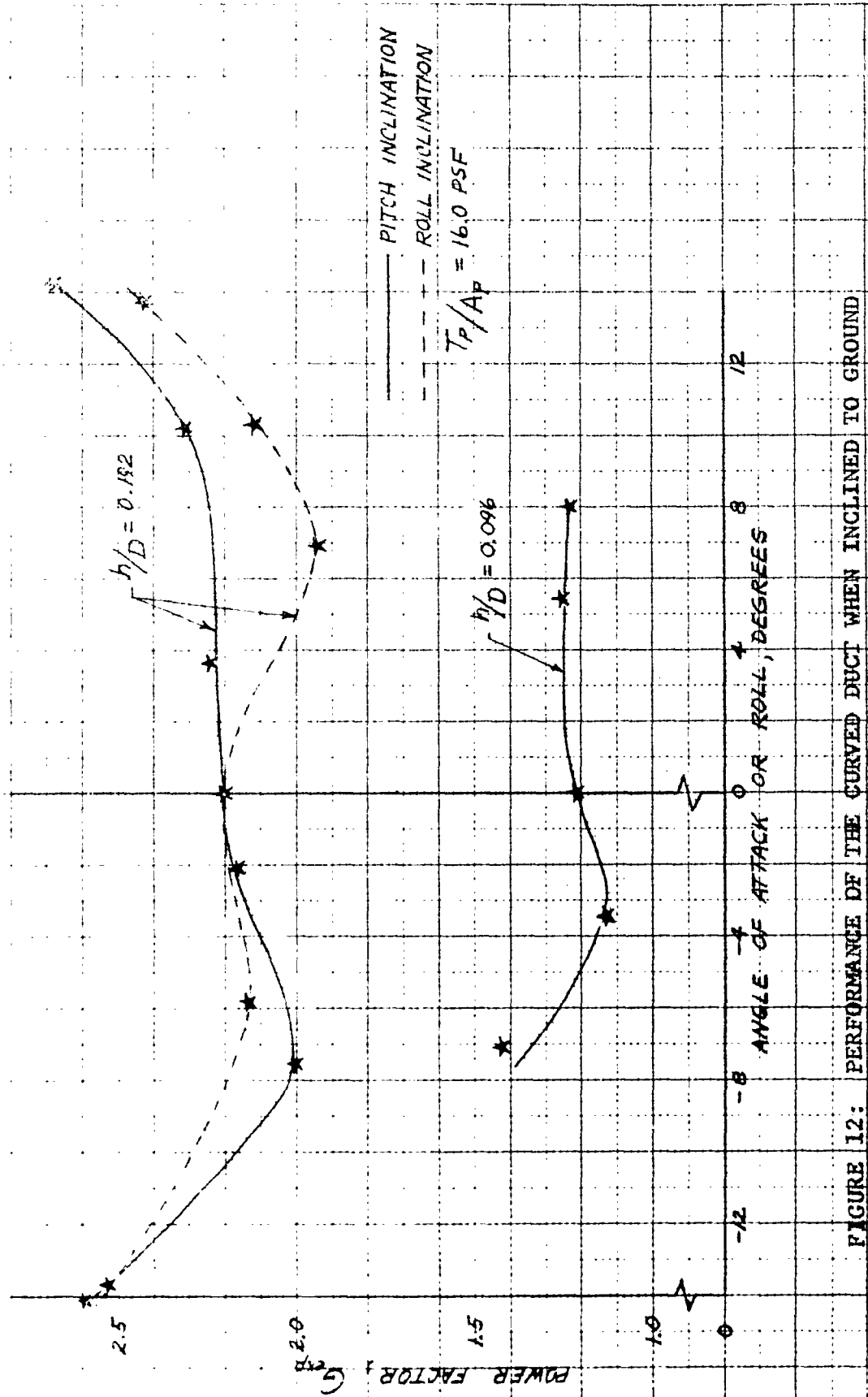


FIGURE 12: PERFORMANCE OF THE CURVED DUCT WHEN INCLINED TO GROUND

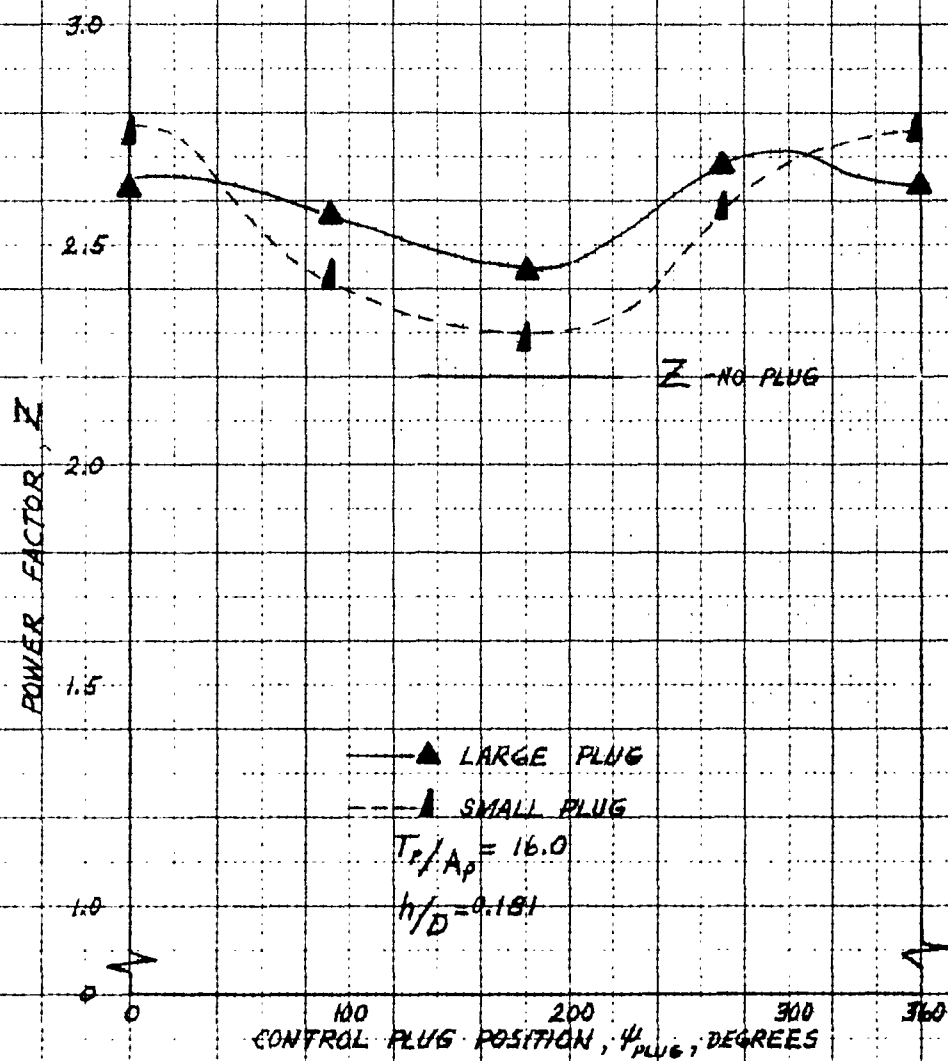


FIGURE 13: EFFECT OF CONTROL PLUG ON PERFORMANCE OF CURVED DUCT

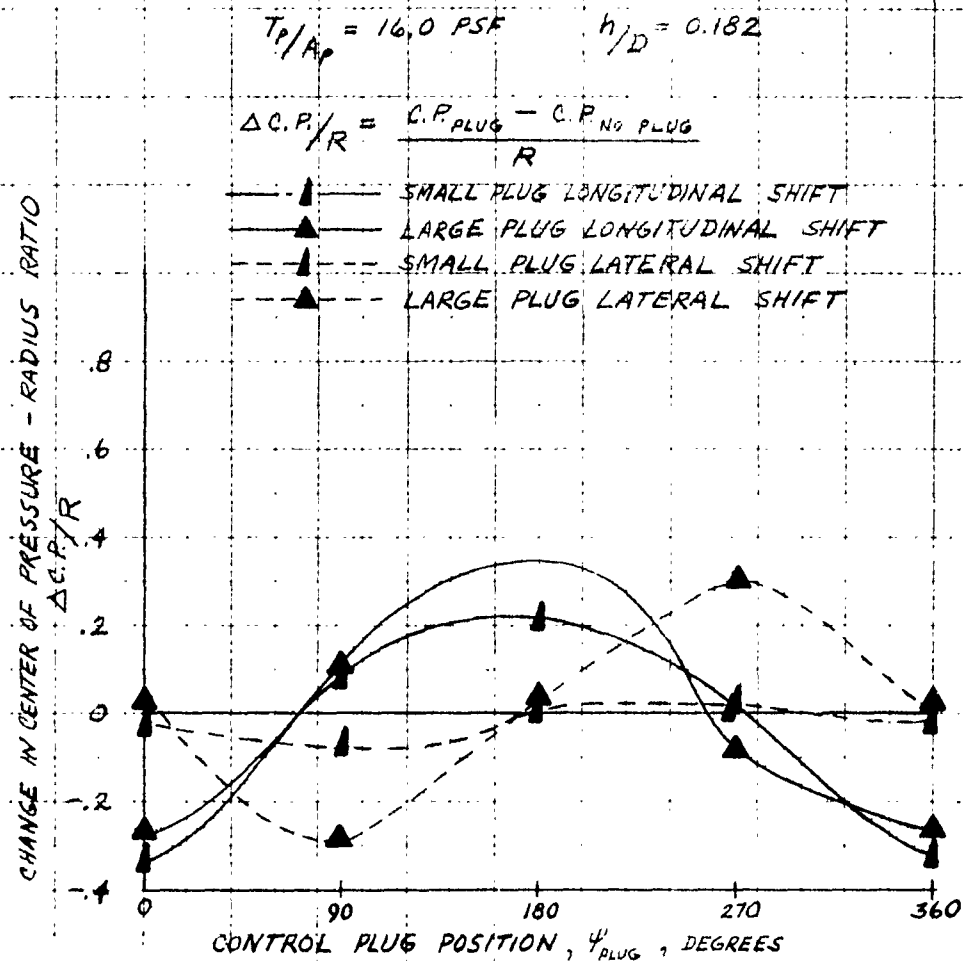


FIGURE 14: CHANGE IN CENTER OF PRESSURE OF THE ANNULAR JET DUE TO A CONTROL PLUG IN THE NOZZLE FOR THE CURVED DUCT.

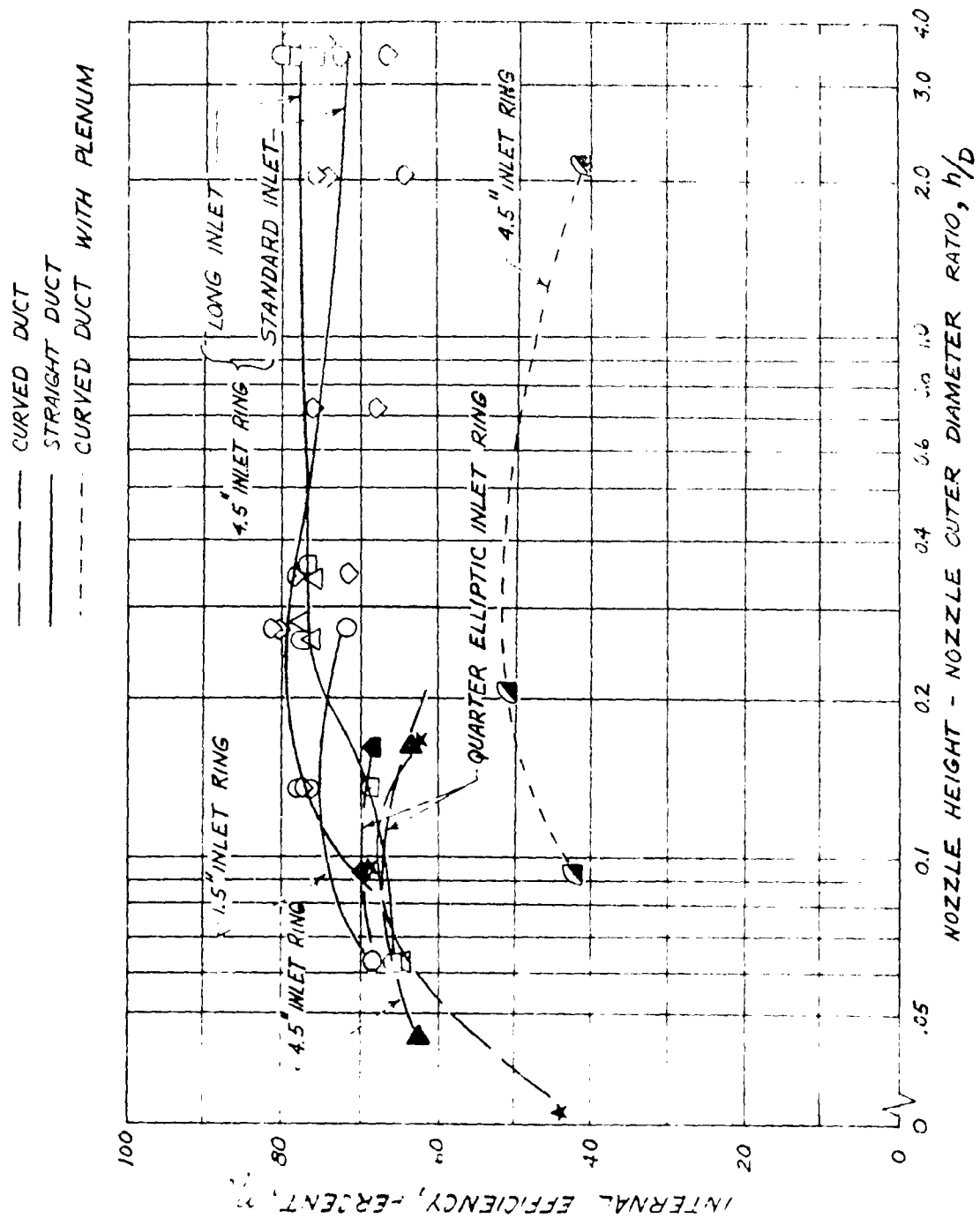


FIGURE 15: OVERALL INTERNAL EFFICIENCY OF VARIOUS STRAIGHT AND CURVED DUCT CONFIGURATIONS

208A90-1 208A90-1 208A90-1 208A90-1 208A90-1

208A90-1 208A90-1 208A90-1 208A90-1 208A90-1

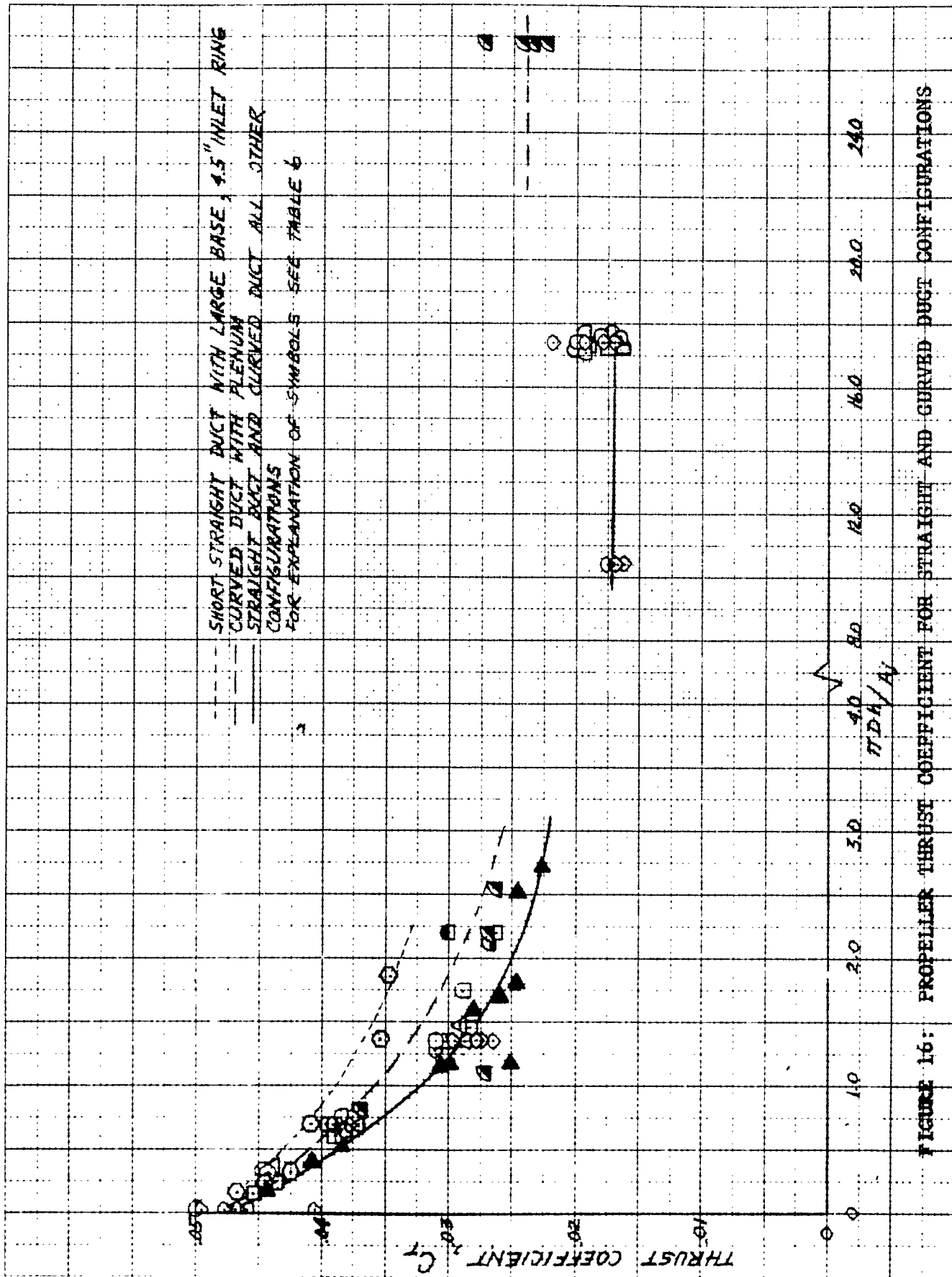
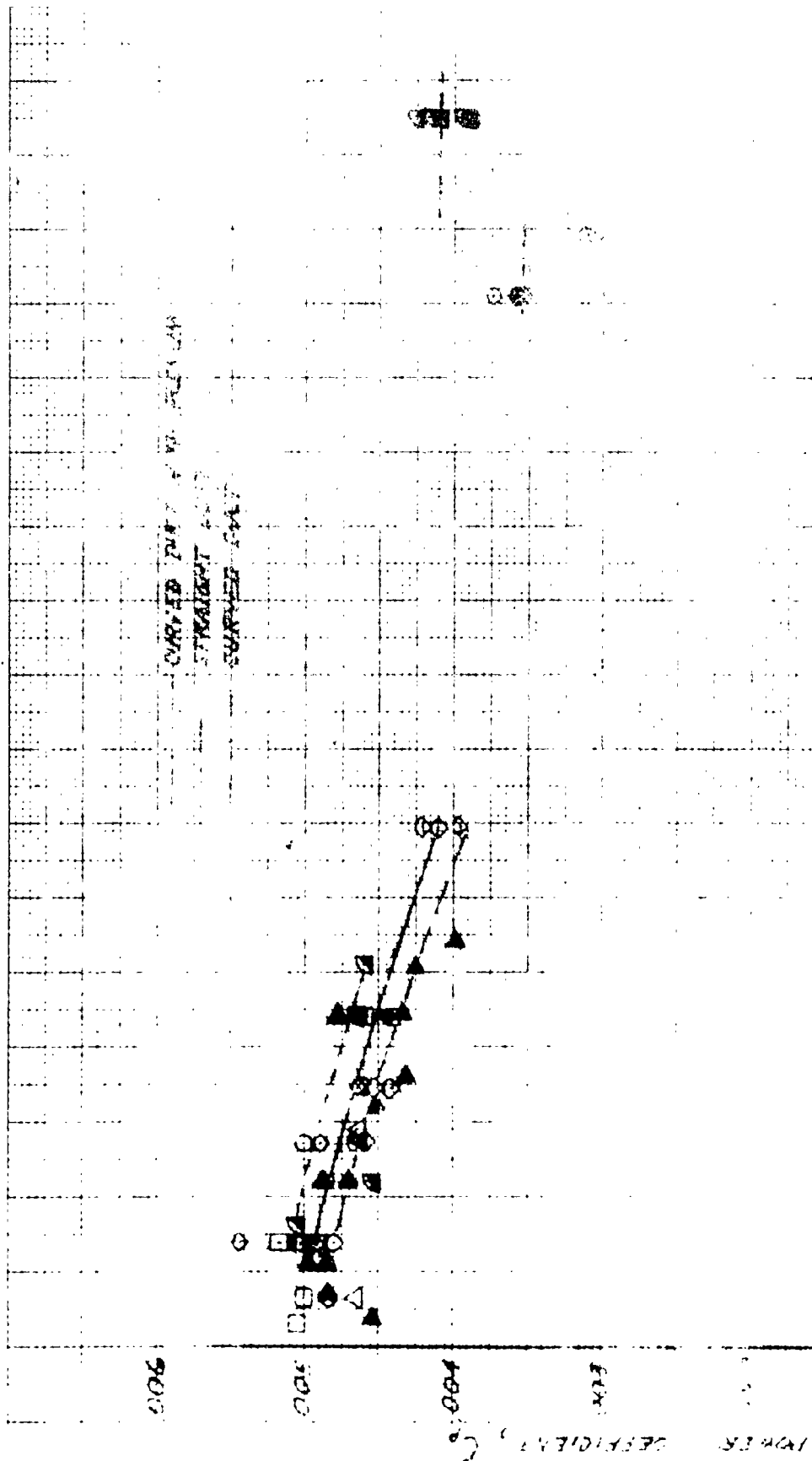


FIGURE 16: PROPELLER THRUST COEFFICIENT FOR STRAIGHT AND CURVED DUCT CONFIGURATIONS

504



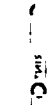
TSR

λ

Curved Planar Airfoil

Straight Airfoil

Curved Airfoil



1
2
3
4
5
6
7
8
9
10
11
12
13
14
15
16
17
18
19
20
21
22
23
24
25
26
27
28
29
30
31
32
33
34
35
36
37
38
39
40
41
42
43
44
45
46
47
48
49
50
51
52
53
54
55
56
57
58
59
60
61
62
63
64
65
66
67
68
69
70
71
72
73
74
75
76
77
78
79
80
81
82
83
84
85
86
87
88
89
90
91
92
93
94
95
96
97
98
99
100
101
102
103
104
105
106
107
108
109
110
111
112
113
114
115
116
117
118
119
120
121
122
123
124
125
126
127
128
129
130
131
132
133
134
135
136
137
138
139
140
141
142
143
144
145
146
147
148
149
150
151
152
153
154
155
156
157
158
159
160
161
162
163
164
165
166
167
168
169
170
171
172
173
174
175
176
177
178
179
180
181
182
183
184
185
186
187
188
189
190
191
192
193
194
195
196
197
198
199
200
201
202
203
204
205
206
207
208
209
210
211
212
213
214
215
216
217
218
219
220
221
222
223
224
225
226
227
228
229
230
231
232
233
234
235
236
237
238
239
240
241
242
243
244
245
246
247
248
249
250
251
252
253
254
255
256
257
258
259
260
261
262
263
264
265
266
267
268
269
270
271
272
273
274
275
276
277
278
279
280
281
282
283
284
285
286
287
288
289
290
291
292
293
294
295
296
297
298
299
300
301
302
303
304
305
306
307
308
309
310
311
312
313
314
315
316
317
318
319
320
321
322
323
324
325
326
327
328
329
330
331
332
333
334
335
336
337
338
339
340
341
342
343
344
345
346
347
348
349
350
351
352
353
354
355
356
357
358
359
360
361
362
363
364
365
366
367
368
369
370
371
372
373
374
375
376
377
378
379
380
381
382
383
384
385
386
387
388
389
390
391
392
393
394
395
396
397
398
399
400
401
402
403
404
405
406
407
408
409
410
411
412
413
414
415
416
417
418
419
420
421
422
423
424
425
426
427
428
429
430
431
432
433
434
435
436
437
438
439
440
441
442
443
444
445
446
447
448
449
450
451
452
453
454
455
456
457
458
459
460
461
462
463
464
465
466
467
468
469
470
471
472
473
474
475
476
477
478
479
480
481
482
483
484
485
486
487
488
489
490
491
492
493
494
495
496
497
498
499
500
501
502
503
504
505
506
507
508
509
510
511
512
513
514
515
516
517
518
519
520
521
522
523
524
525
526
527
528
529
530
531
532
533
534
535
536
537
538
539
540
541
542
543
544
545
546
547
548
549
550
551
552
553
554
555
556
557
558
559
560
561
562
563
564
565
566
567
568
569
570
571
572
573
574
575
576
577
578
579
580
581
582
583
584
585
586
587
588
589
590
591
592
593
594
595
596
597
598
599
600
601
602
603
604
605
606
607
608
609
610
611
612
613
614
615
616
617
618
619
620
621
622
623
624
625
626
627
628
629
630
631
632
633
634
635
636
637
638
639
640
641
642
643
644
645
646
647
648
649
650
651
652
653
654
655
656
657
658
659
660
661
662
663
664
665
666
667
668
669
670
671
672
673
674
675
676
677
678
679
680
681
682
683
684
685
686
687
688
689
690
691
692
693
694
695
696
697
698
699
700
701
702
703
704
705
706
707
708
709
710
711
712
713
714
715
716
717
718
719
720
721
722
723
724
725
726
727
728
729
730
731
732
733
734
735
736
737
738
739
740
741
742
743
744
745
746
747
748
749
750
751
752
753
754
755
756
757
758
759
760
761
762
763
764
765
766
767
768
769
770
771
772
773
774
775
776
777
778
779
780
781
782
783
784
785
786
787
788
789
790
791
792
793
794
795
796
797
798
799
800
801
802
803
804
805
806
807
808
809
810
811
812
813
814
815
816
817
818
819
820
821
822
823
824
825
826
827
828
829
830
831
832
833
834
835
836
837
838
839
840
84

CREVBRINT, BAKER CO

C38 50 X 50 DIVISIONS PER INCH 120 X 500 DIVISIONS

DOW

100% HUMIDITY AT 100% RELATIVE HUMIDITY

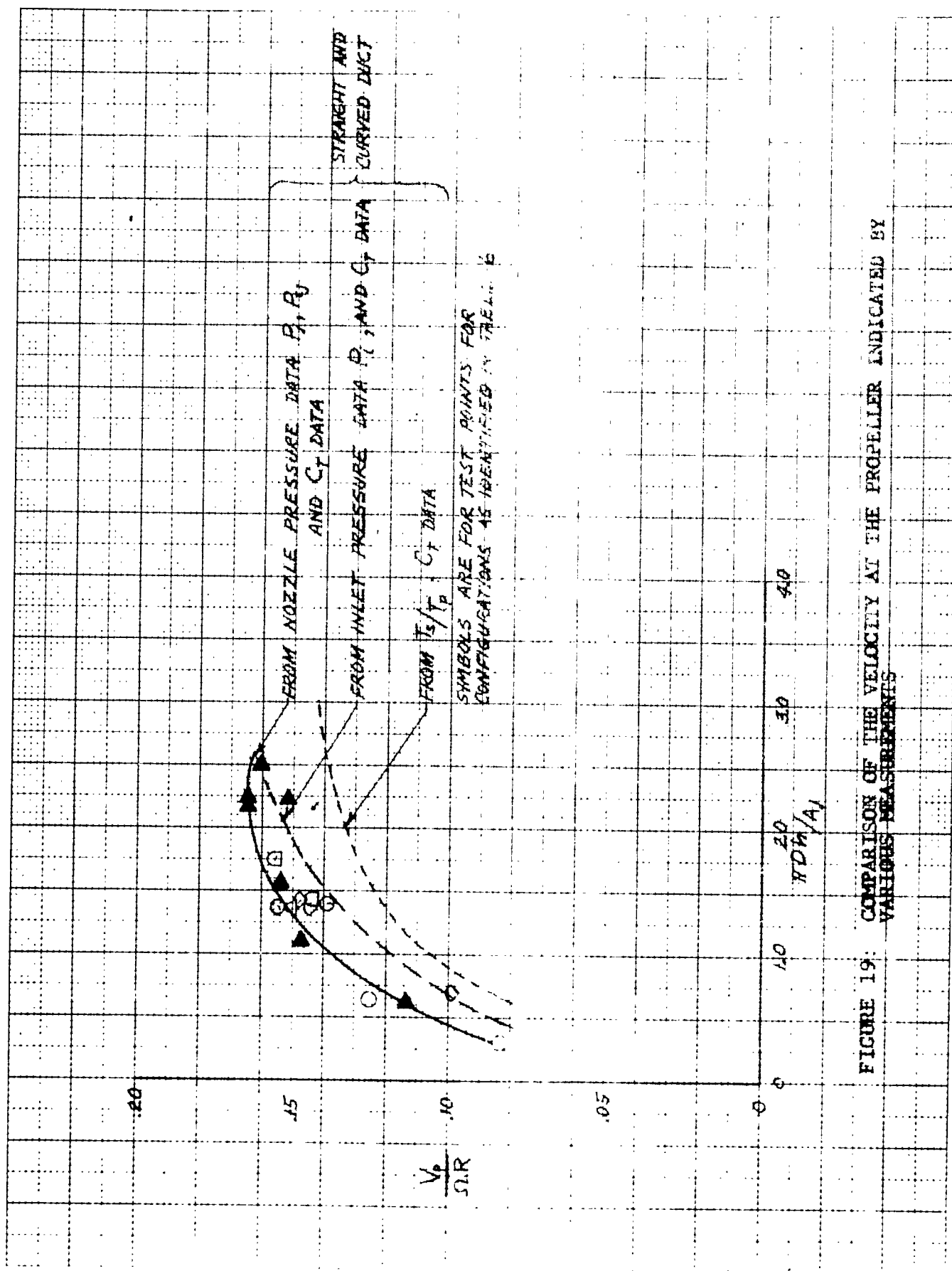


FIGURE 19: COMPARISON OF THE VELOCITY AT THE PROPELLER INDICATED BY VARIOUS MEASUREMENTS

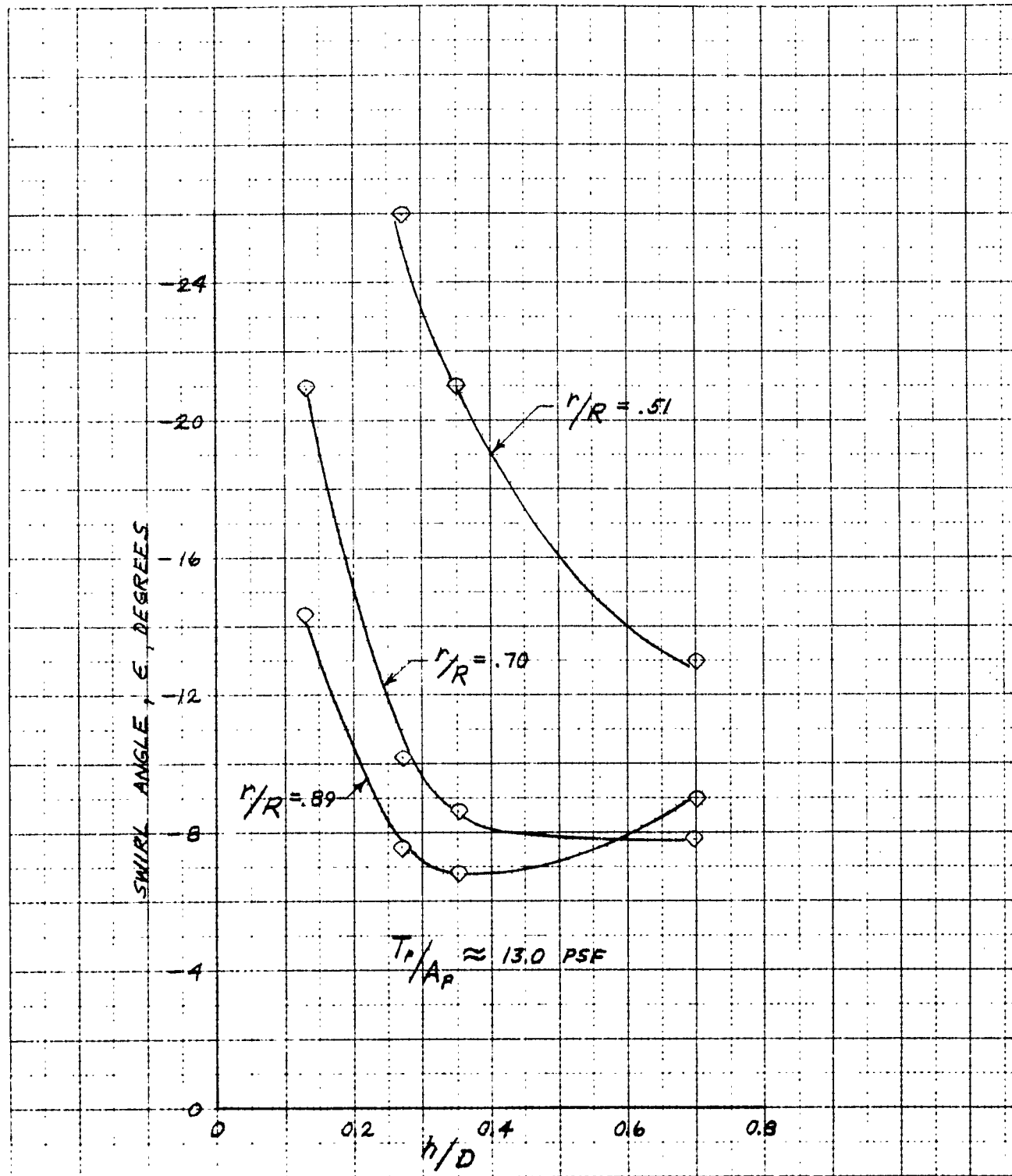


FIGURE 20. TYPICAL FLOW SWIRL DATA FOR STRAIGHT DUCT TEST UNIT WITH 4.5 INCH INLET RING

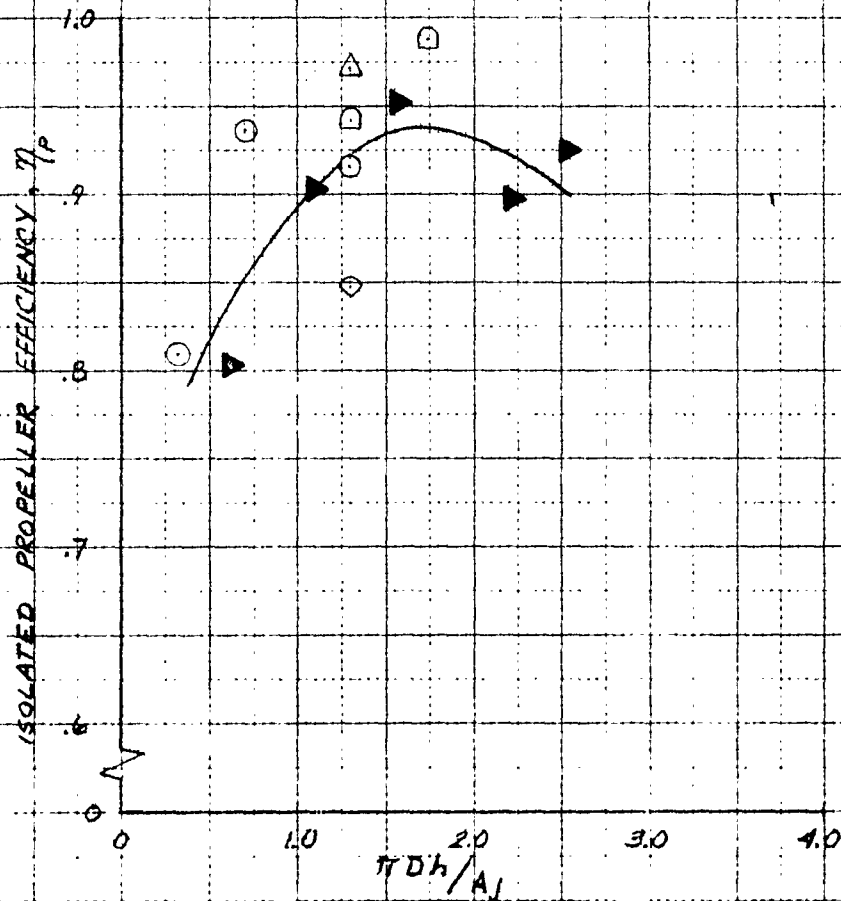
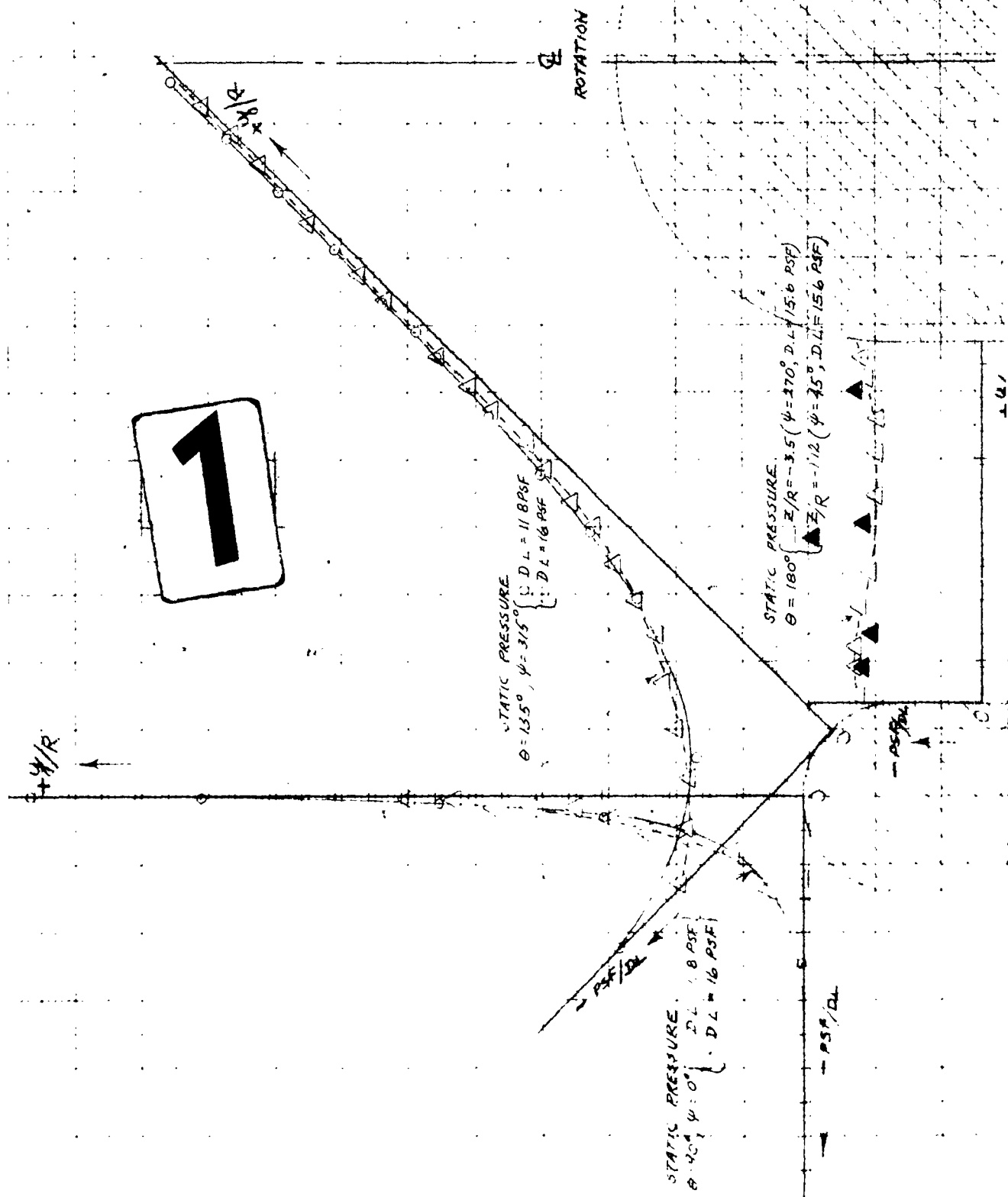


FIGURE 21: ISOLATED PROPELLER EFFICIENCY BASED ON NOZZLE PRESSURE MEASUREMENTS FOR CURVED AND STRAIGHT DUCT CONFIGURATIONS



$\Delta Z/R = -1.2 (\psi = 15^\circ, D/L = 15.6 \text{ PSF})$

$- \text{PSF}/DL$

$+ \psi/R$

$- \text{PSF}/DL$

STATIC PRESSURE

$\theta = 180^\circ, Z/R = -0.17 (\psi = 0^\circ, D/L = 12.1 \text{ PSF})$
 $\theta = 180^\circ, Z/R = -0.17 (\psi = 0^\circ, D/L = 15.6 \text{ PSF})$

$+ \psi/R$

$- \text{PSF}/DL$

$+ \psi/R$

$+ \text{PSF}/DL$

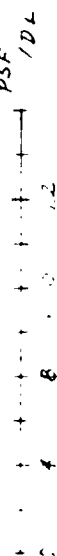
PLANE OF PROPELLER

Short Inlet
 $Z/R = +0.13 (\psi = 180^\circ, D/L = 14.7 \text{ PSF})$
 Long Inlet
 $Z/R = +0.33 (\psi = 45^\circ, D/L = 15.6 \text{ PSF})$
 $\Delta Z/R = +1.48 (\psi = 45^\circ, D/L = 15.6 \text{ PSF})$

STATIC PRESSURE
 TOTAL PRESSURE
 $\theta = 180^\circ$

PSF/DL

SCALE



7.4'

ψ/R

SYMBOLS

--- SHORT INLET (LENGTH FROM FORWARD EDGE OF INLET RING TO PROPELLER = 0.60R)
 --- LONG INLET (LENGTH FROM FORWARD EDGE OF INLET RING TO PROPELLER = 0.80R)

2

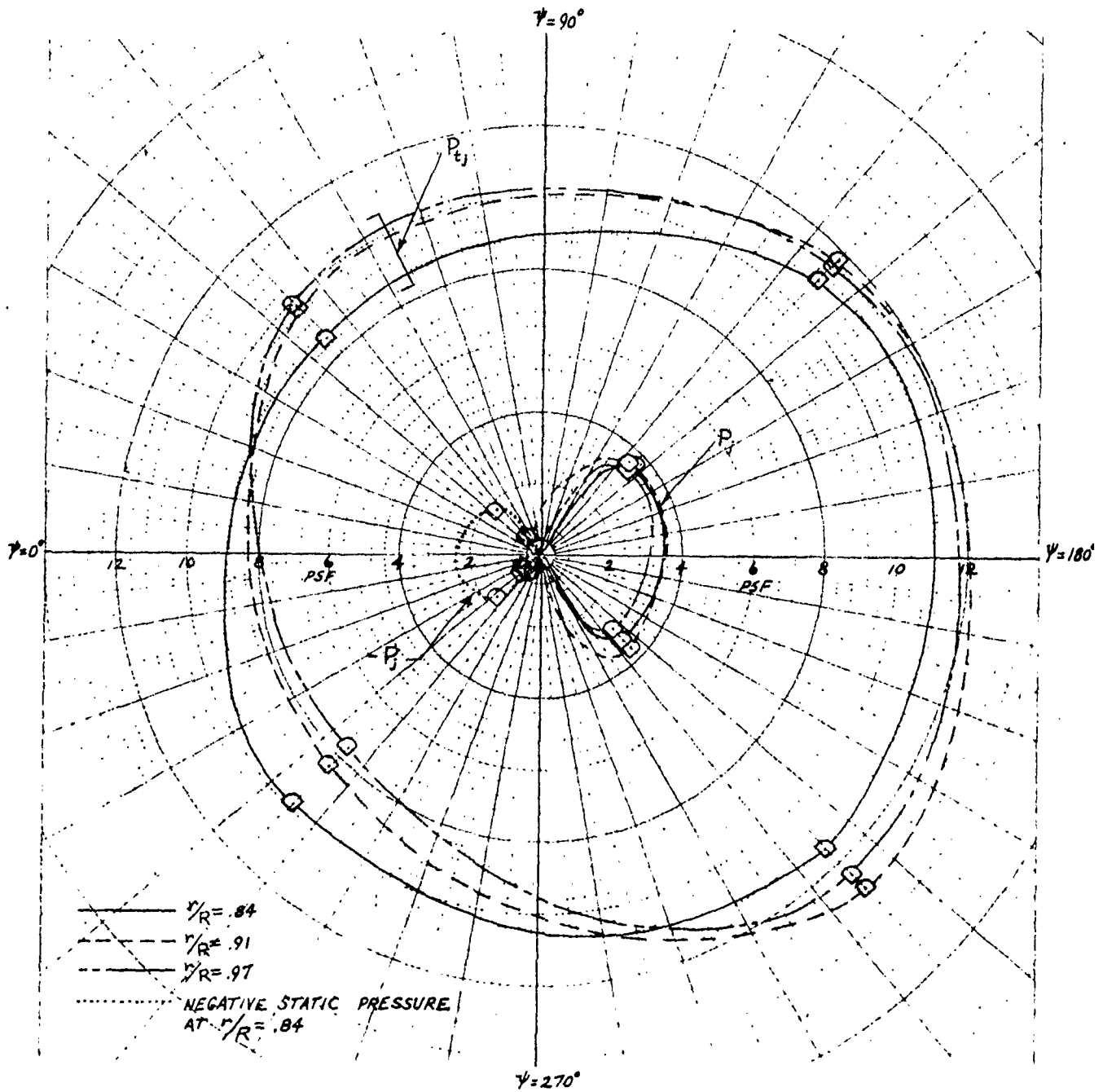


FIGURE 24: POLAR PLOT OF TOTAL AND STATIC PRESSURES AT THE ANNULAR JET NOZZLE OF THE CURVED DUCT AT AN h/D OF 0.181

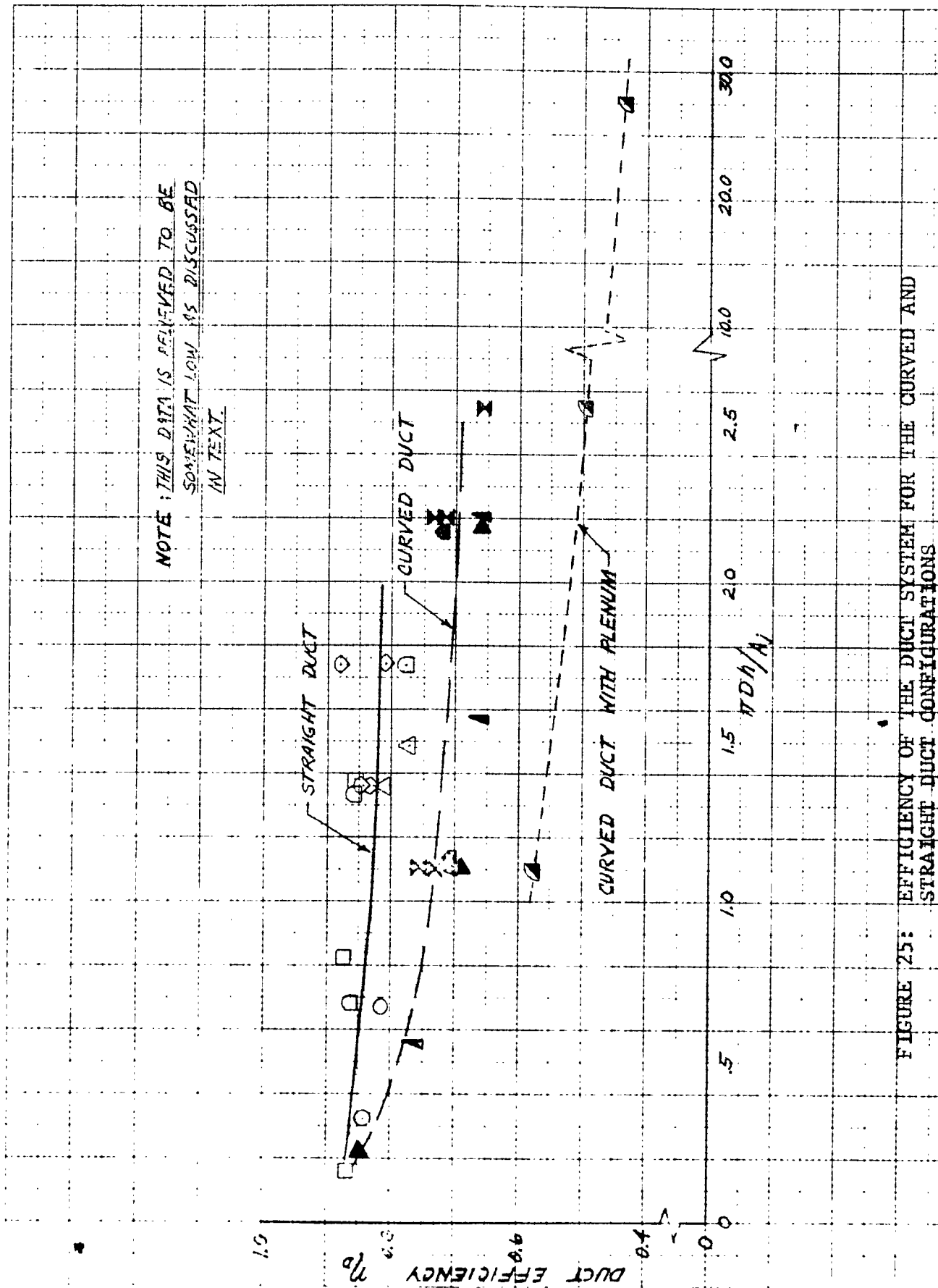


FIGURE 25: EFFICIENCY OF THE DUCT SYSTEM FOR THE CURVED AND STRAIGHT DUCT CONFIGURATIONS

STEADY STATE

M. H. B. R. P. H. D. I. D. S. K. U. S. A. F. S. O. M. E. T. A. I. M. I. N. I. S. T. R. A. T. I. O. N. A. L.

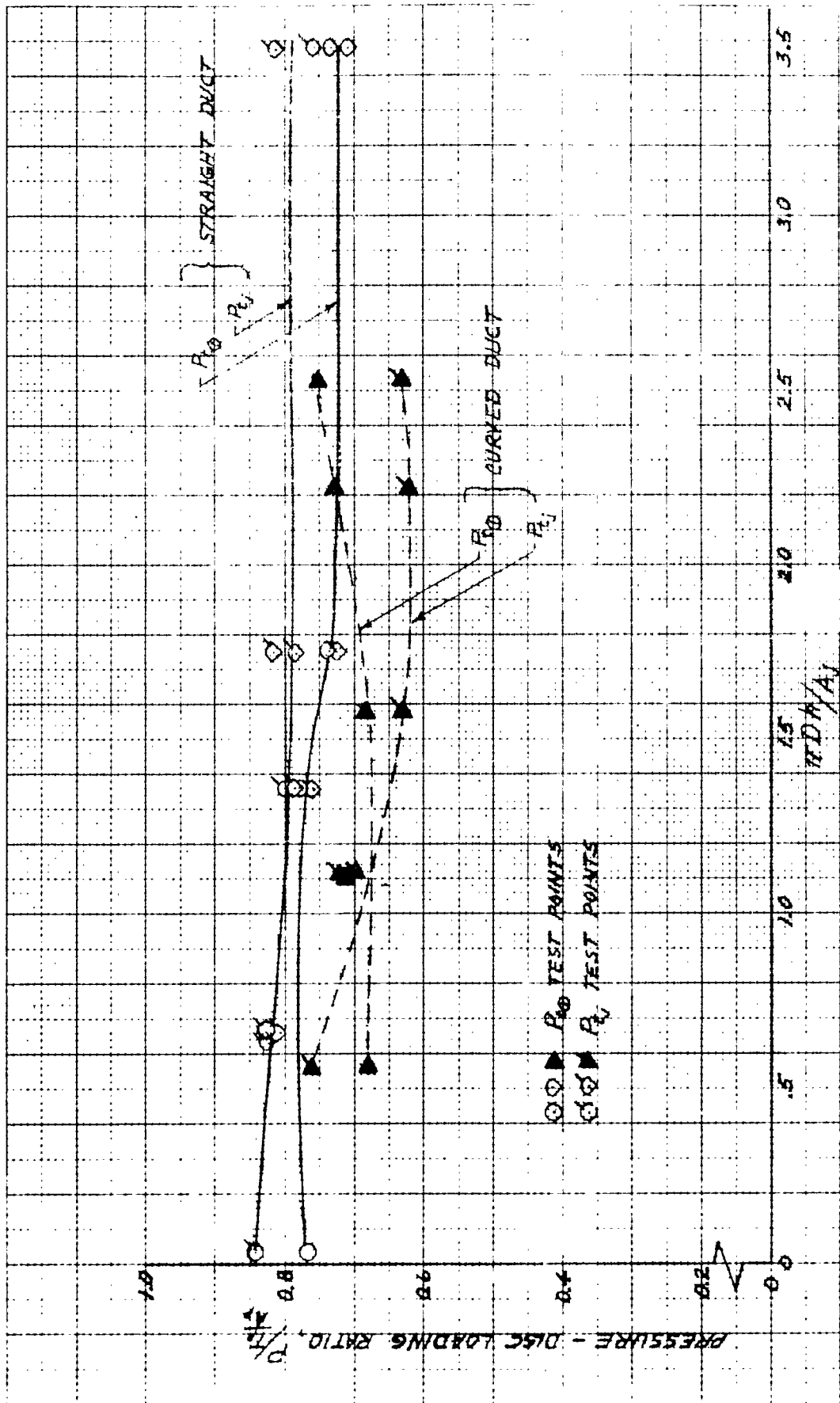


FIGURE 26: TOTAL PRESSURE DATA AT TWO STATIONS BEHIND THE PROPELLER FOR THE CURVED AND STRAIGHT DUCT CONFIGURATIONS

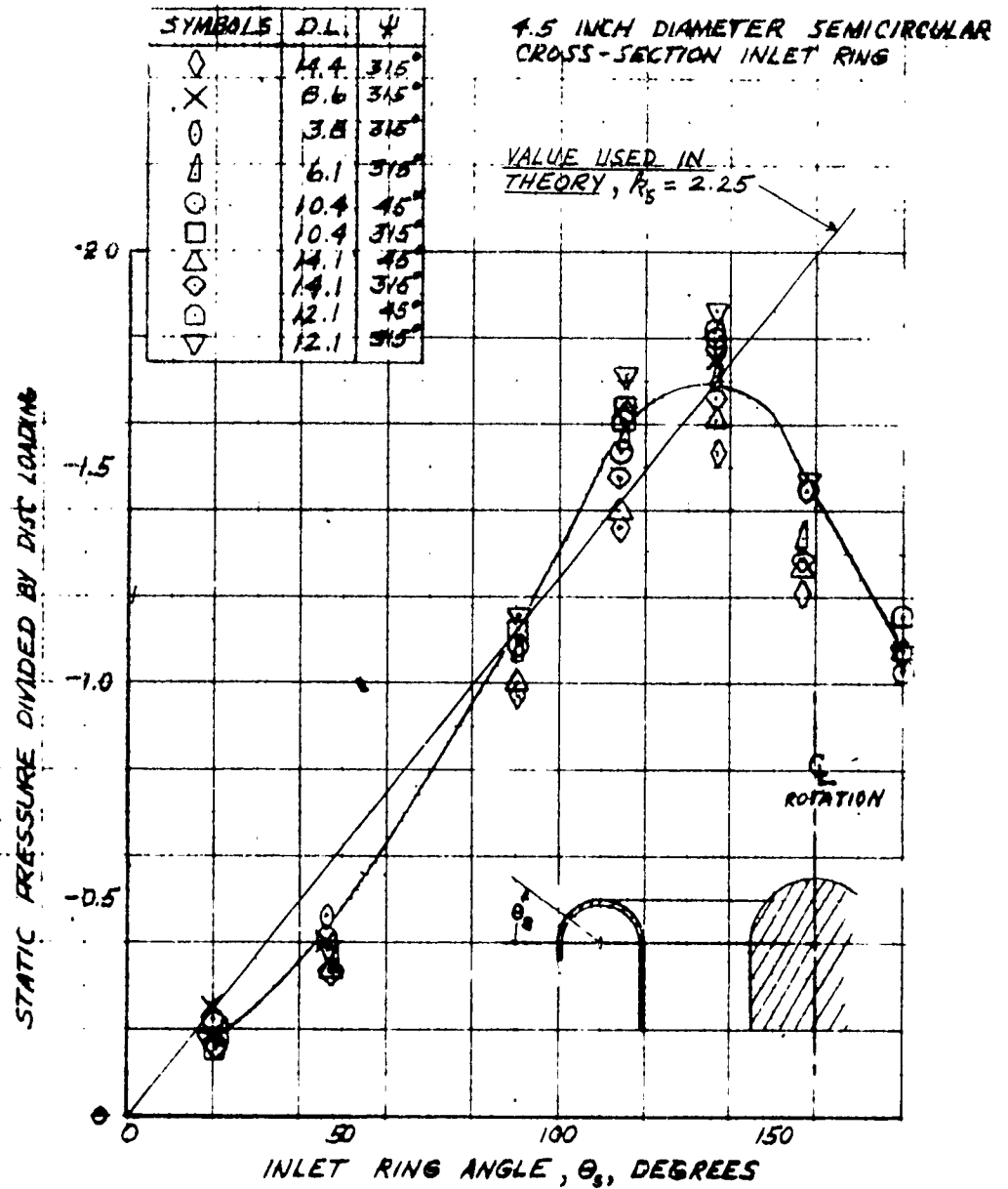


FIGURE 27: STATIC PRESSURE ON INLET RING WITH STRAIGHT DUCT, OUT OF GROUND EFFECT

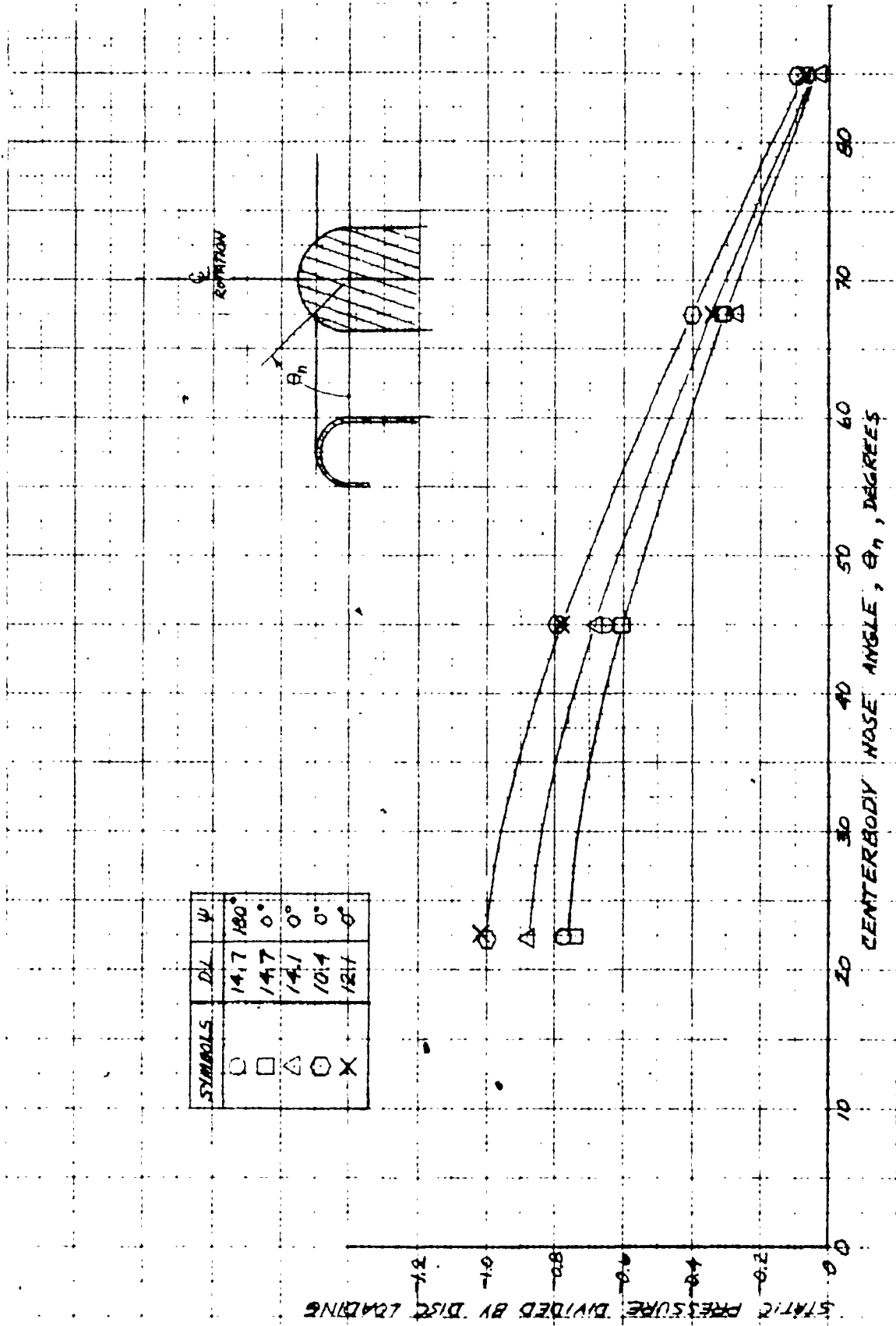


FIGURE 28: STATIC PRESSURE ON INLET NOSE WITH STRAIGHT DUCI, OUT OF GROUND EFFECT

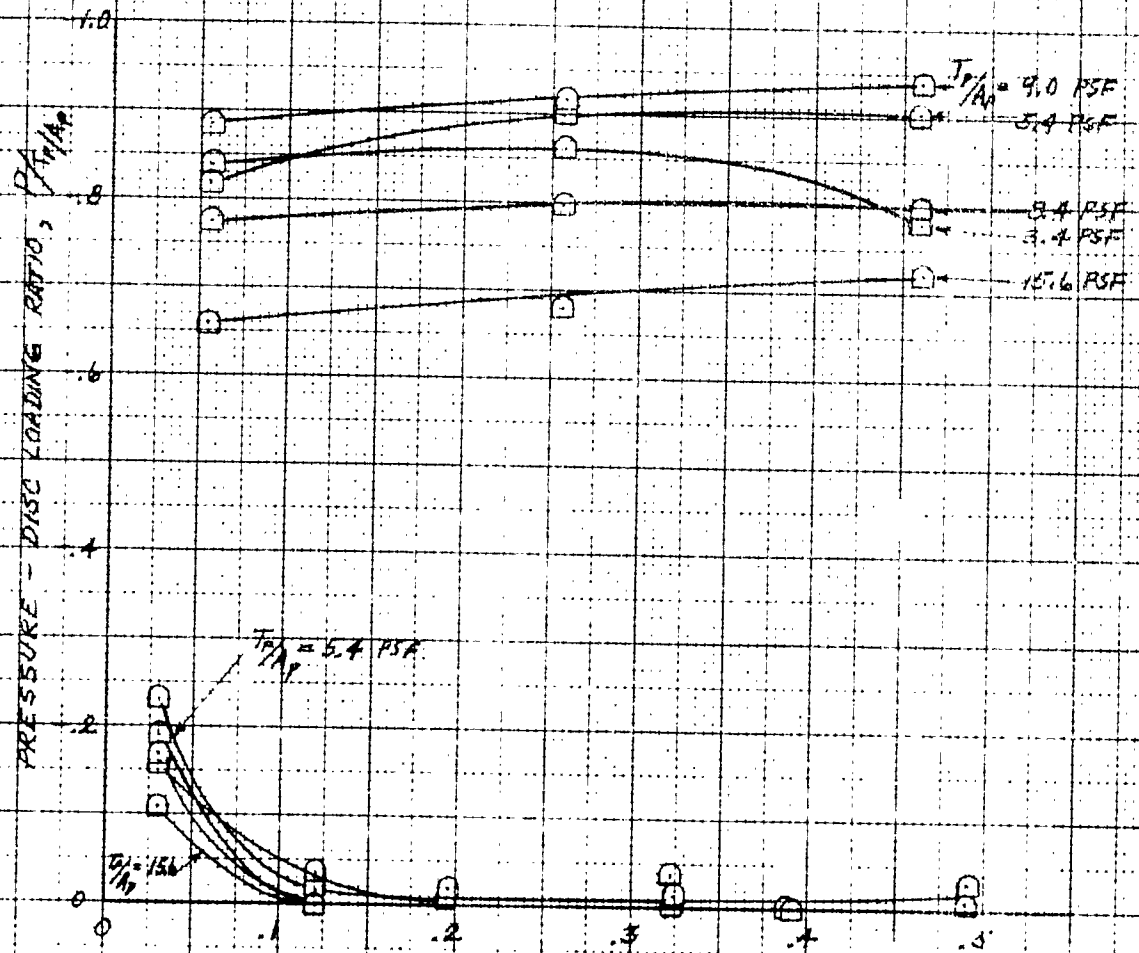


FIGURE 29: STATIC AND TOTAL PRESSURES AT MID LENGTH OF THE LONG INLET ON THE STRAIGHT DUCT.

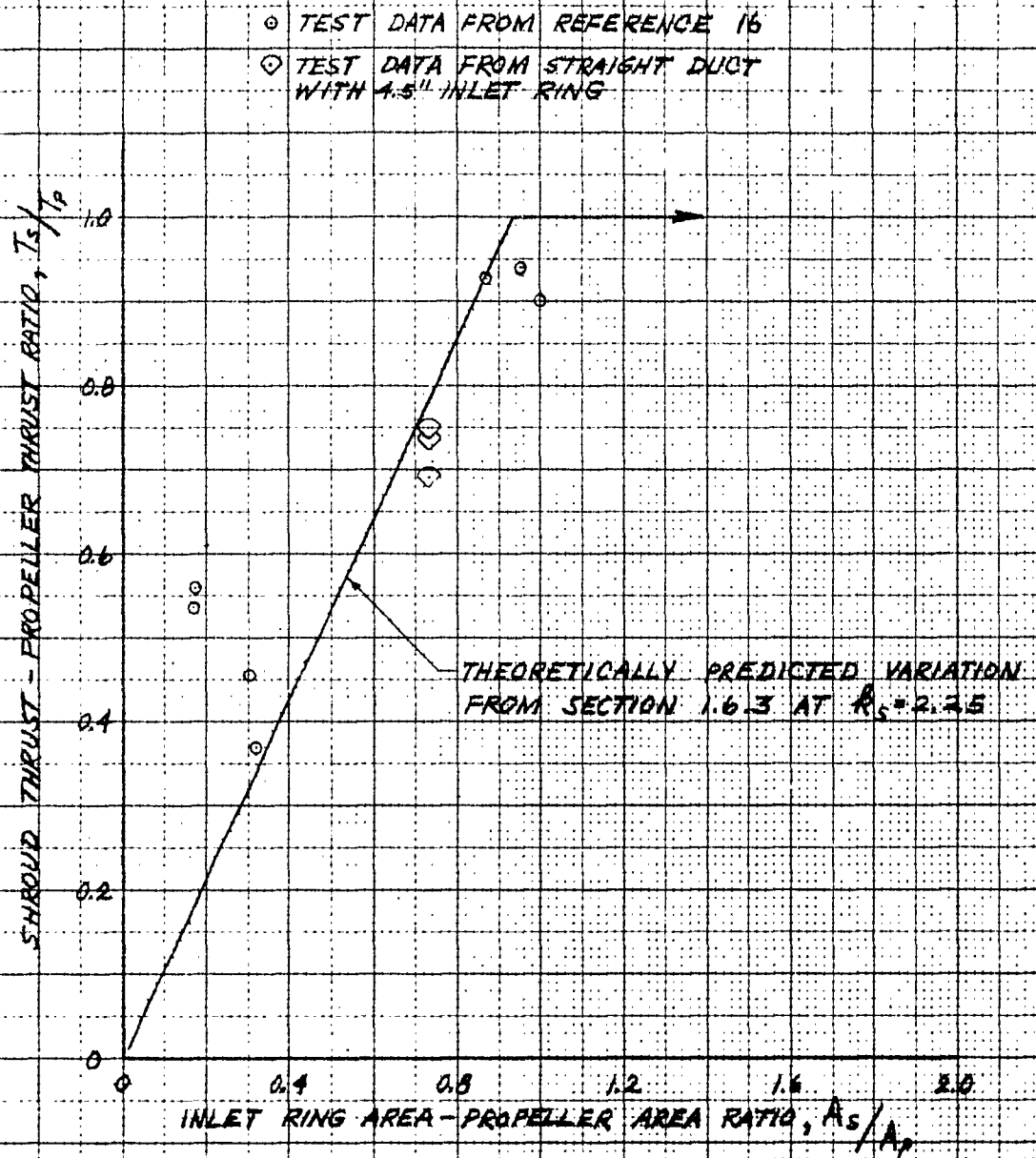


FIGURE 30: INLET RING THRUST AS AFFECTED BY INLET RING AREA BASED ON DATA FROM SHROUDED PROPELLER LITERATURE WITH THEORETICALLY PREDICTED CURVE

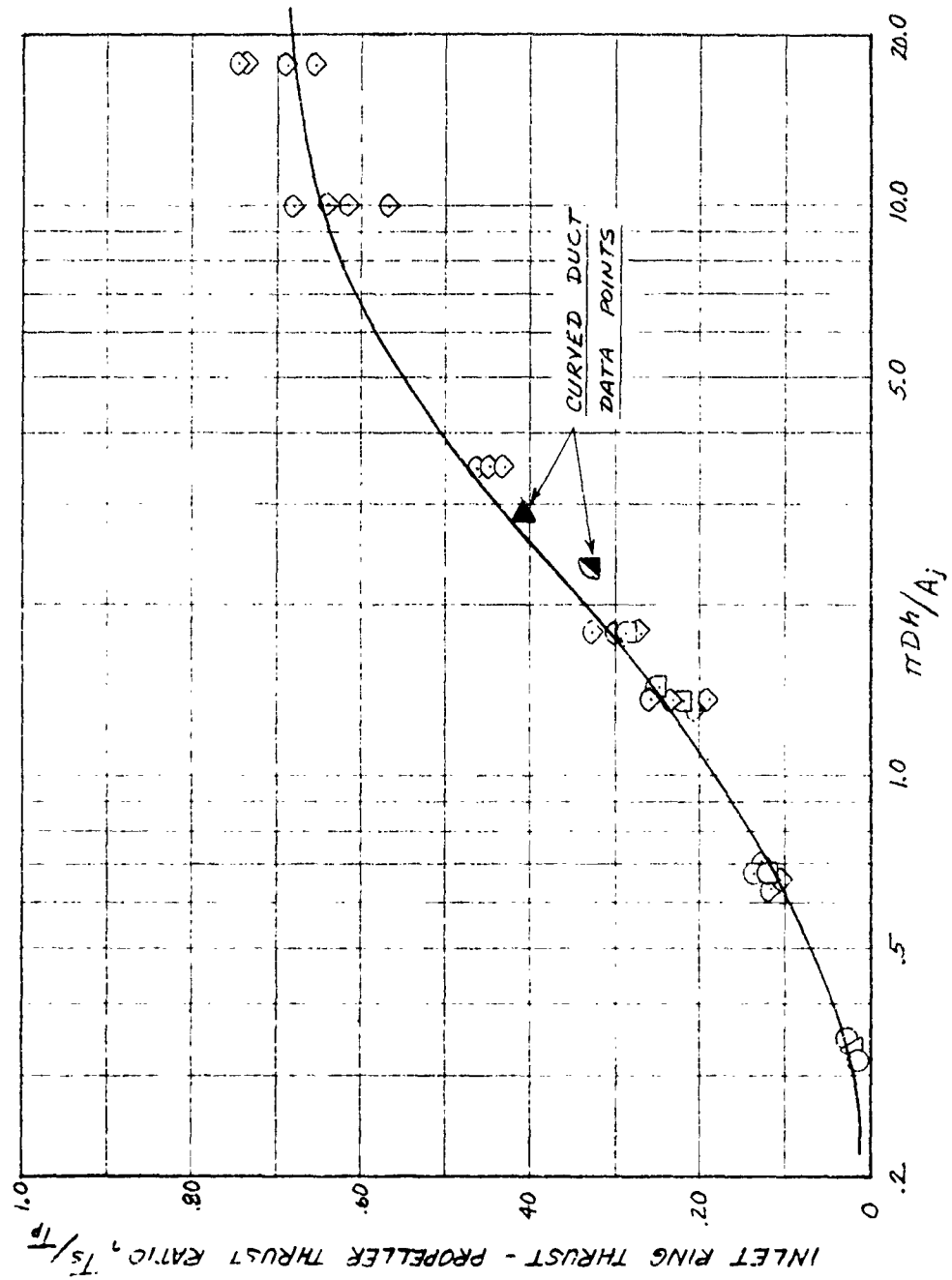


FIGURE 31: INFLUENCE OF NOZZLE HEIGHT ON INLET RING THRUST FOR CURVED AND STRAIGHT DUCT CONFIGURATIONS

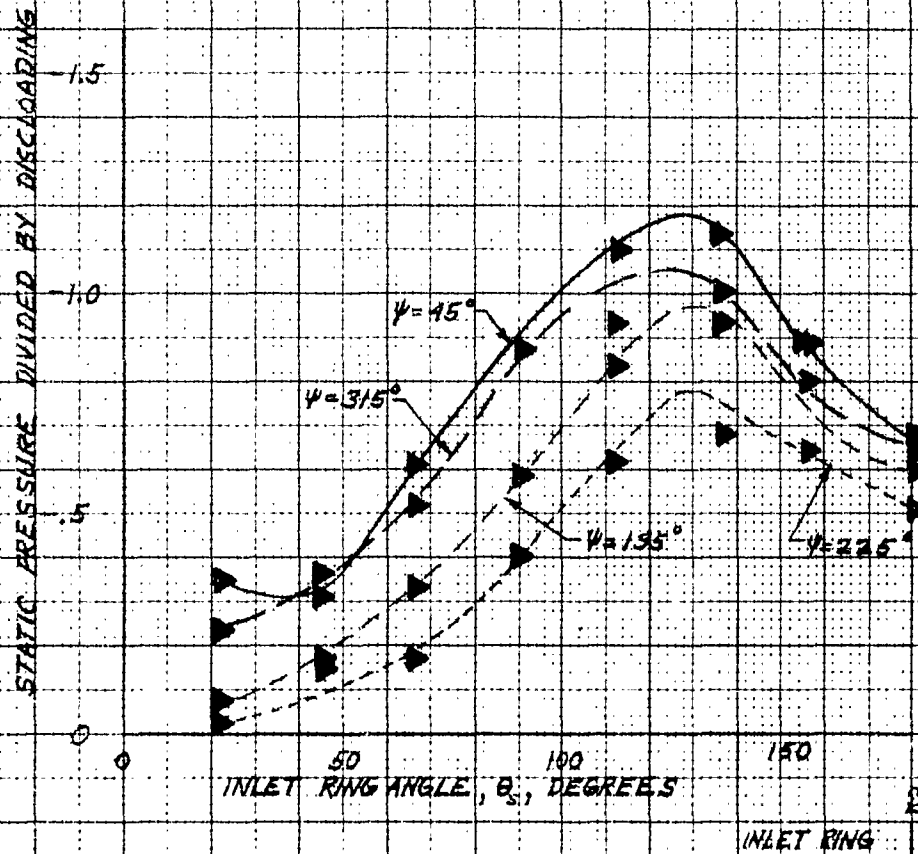


FIGURE 32: STATIC PRESSURE DISTRIBUTION ON A 4.5 INCH INLET RING WITH CURVED DUCT

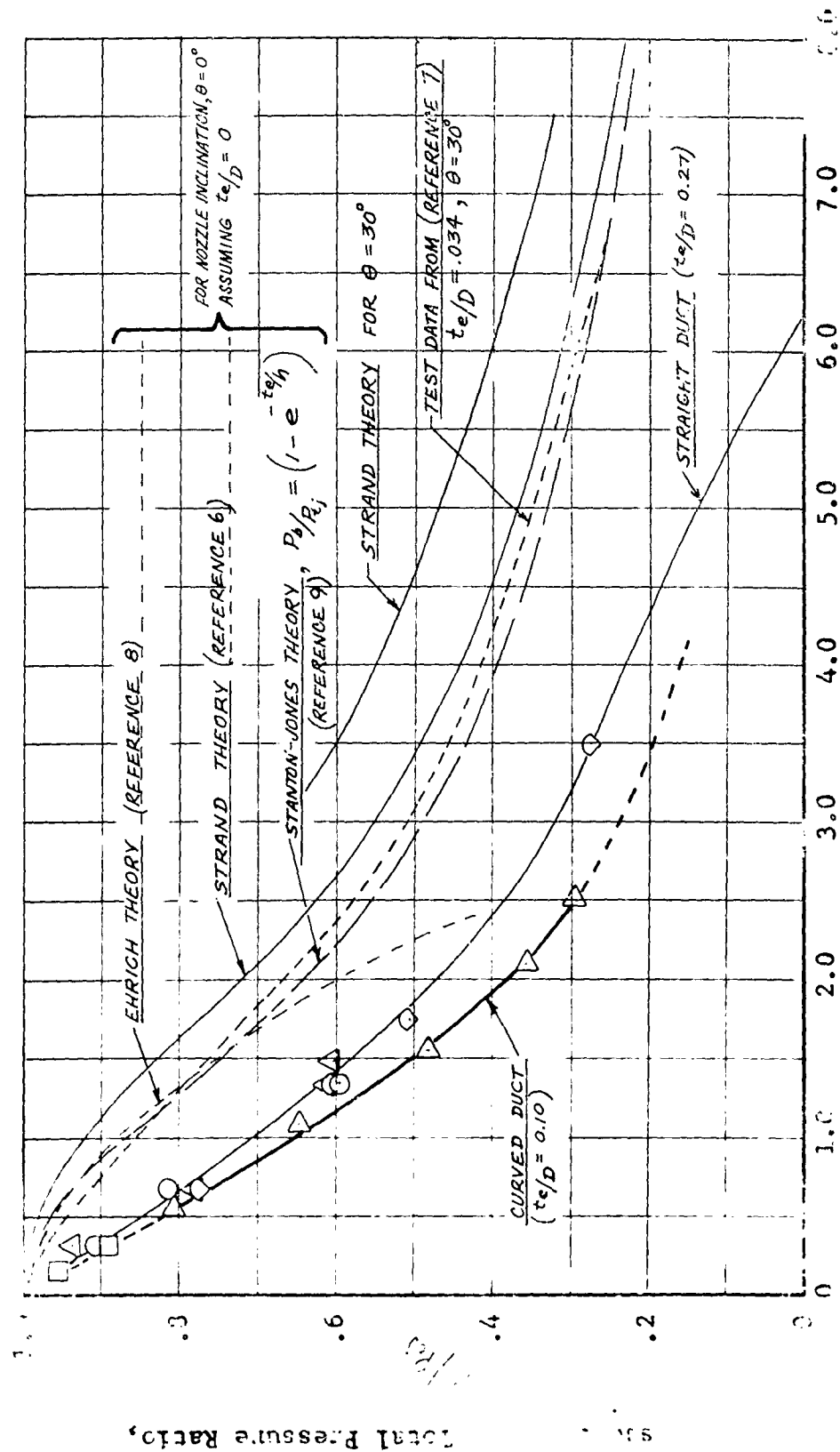
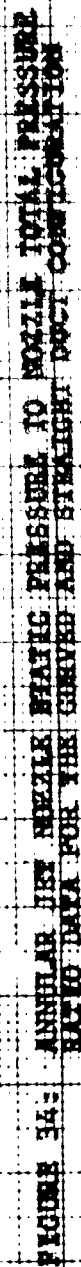


FIGURE 33 COMPARISON OF BASE PRESSURE TO NOZZLE TOTAL PRESSURE RATIO DATA WITH THEORETICAL PREDICTION



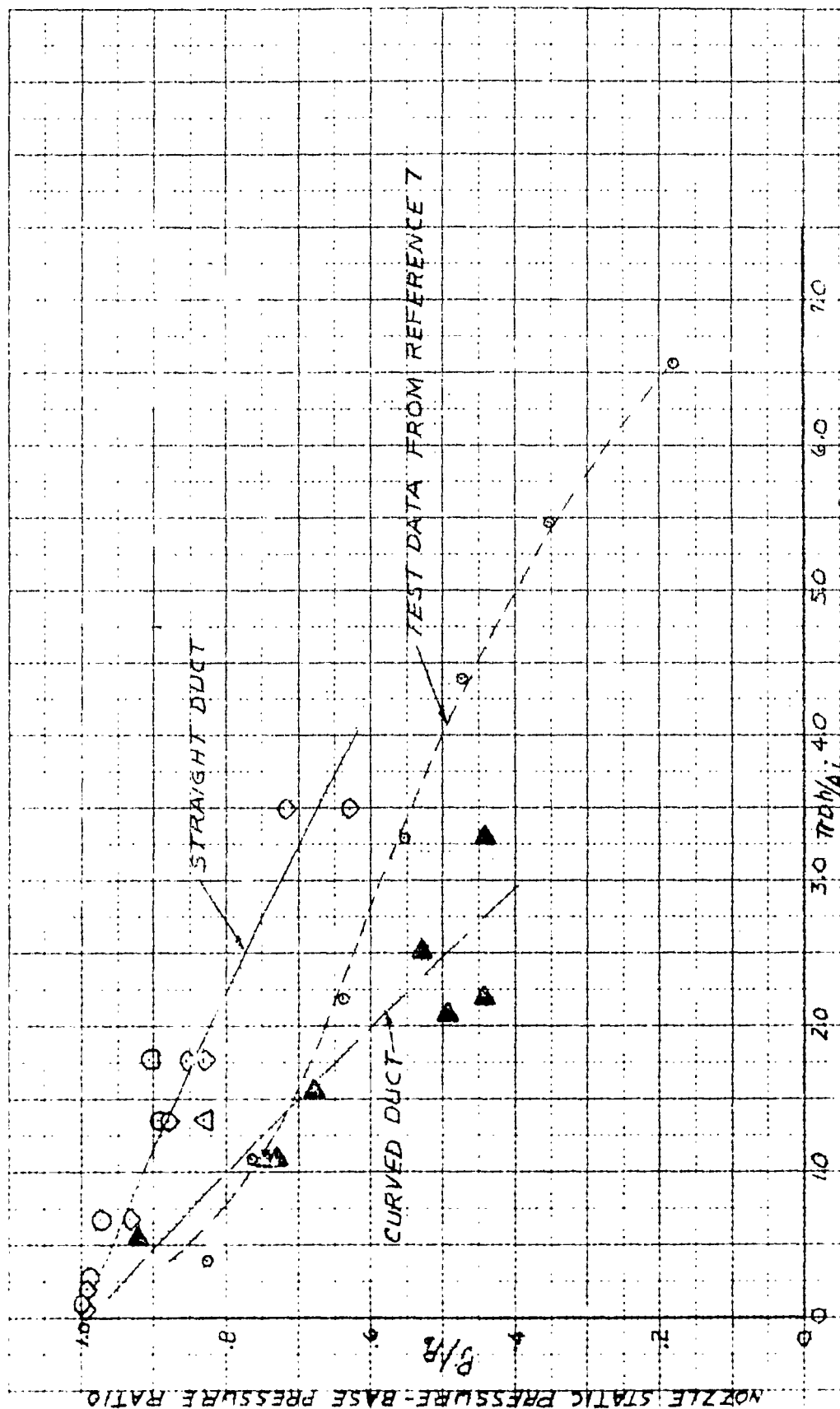


FIGURE 3: ANNULAR JET NOZZLE STATIC PRESSURE TO BASE PRESSURE RATIO FOR THE CURVED AND STRAIGHT DUCT CONFIGURATIONS

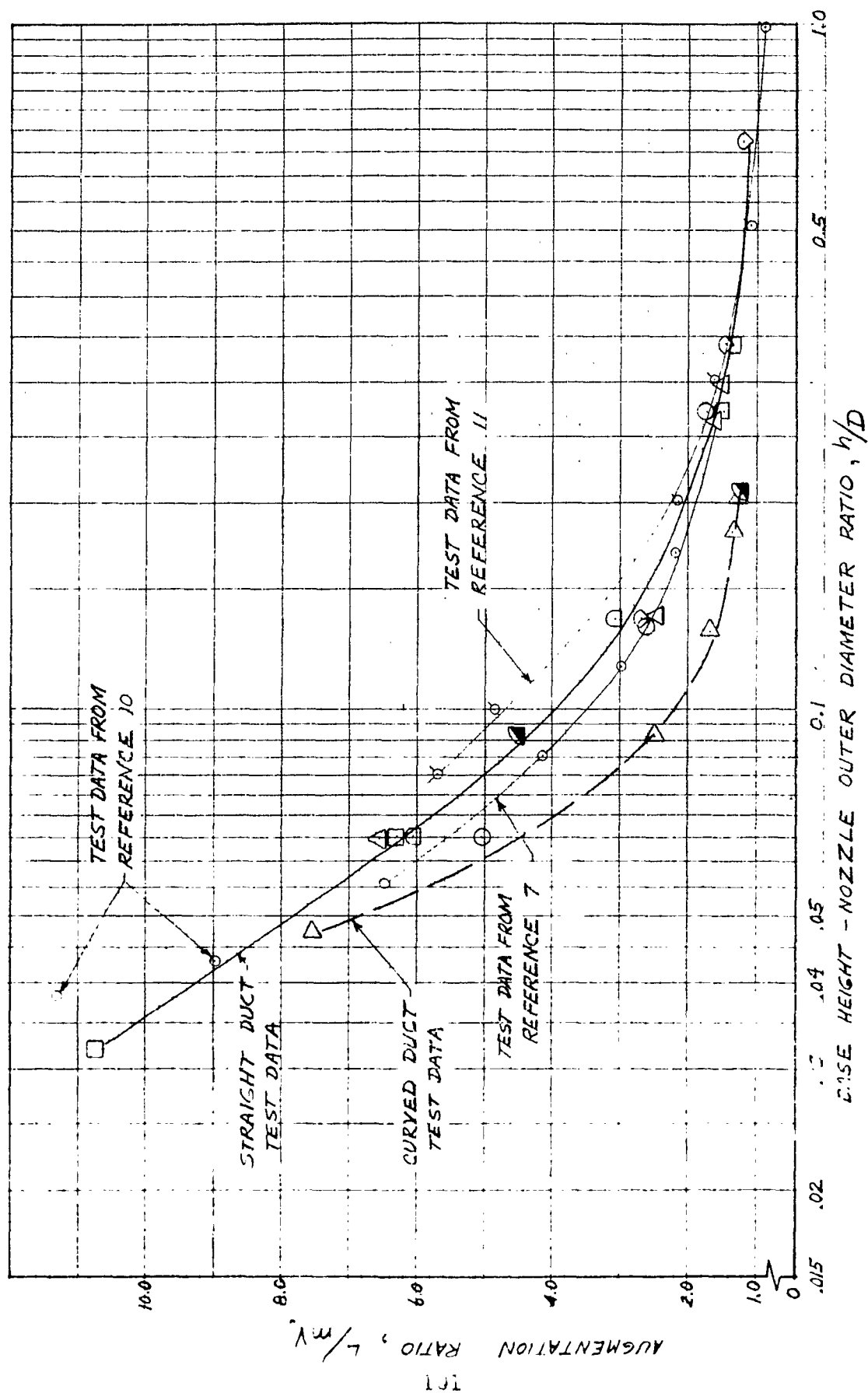


FIGURE 36: AUGMENTATION RATIO DATA WITH COMPARATIVE REFERENCED DATA

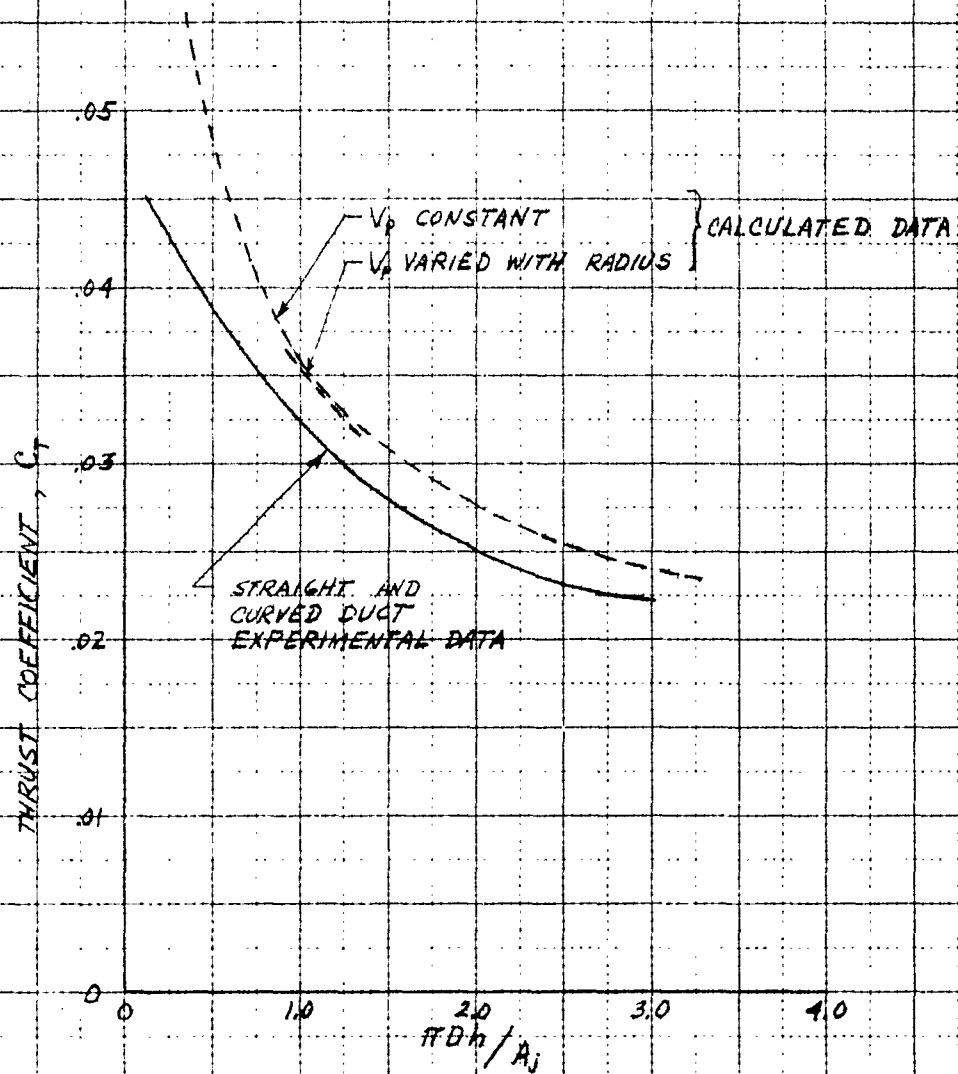


FIGURE 37: COMPARISON OF THEORETICAL AND EXPERIMENTAL PROPELLER THRUST DATA

CREVBRINT PAPER CO

C38 50 X 50 DIVISIONS PER INCH 120 X 500 DIVISIONS

50

PRINTED IN U.S.A. ON CREVBRINT PAPER CO. PAPER NO. 100

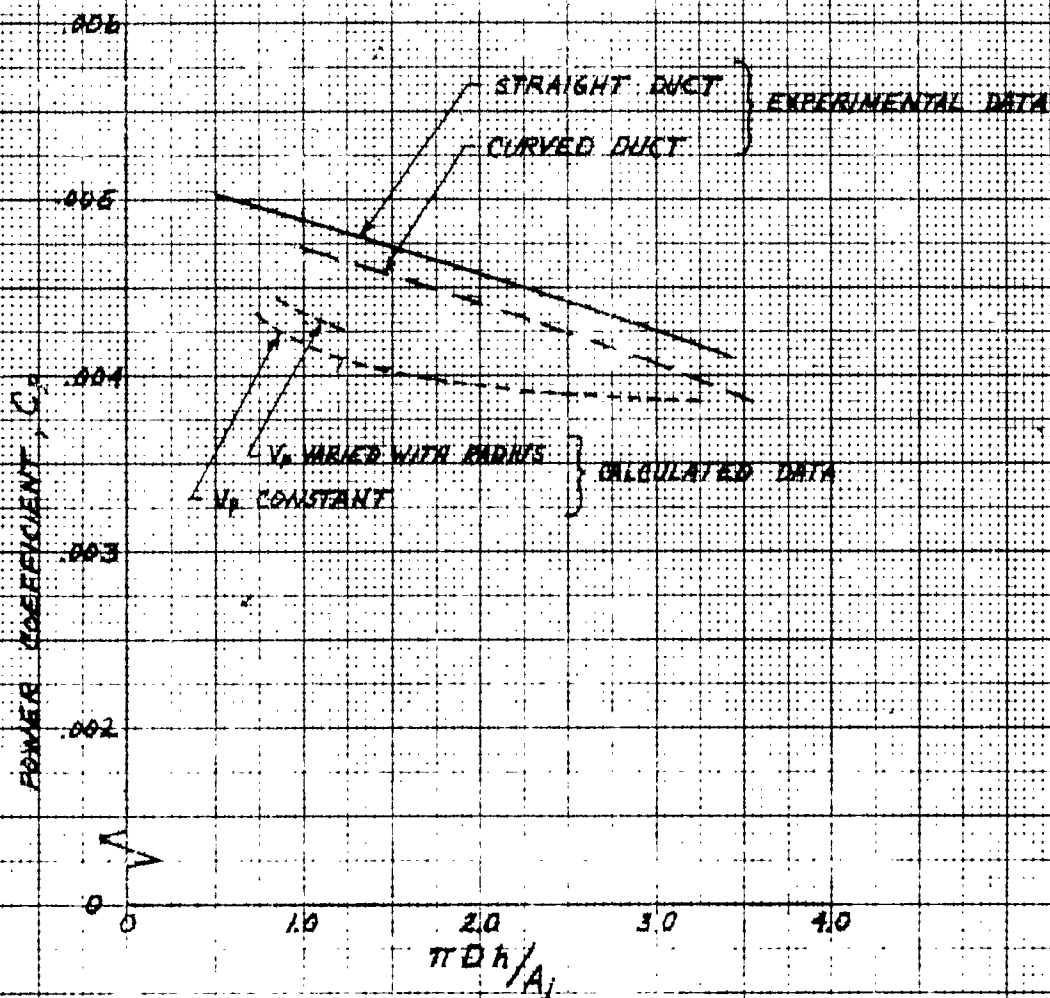


FIGURE 38: COMPARISON OF THEORETICAL AND EXPERIMENTAL PROPELLER THRUST DATA

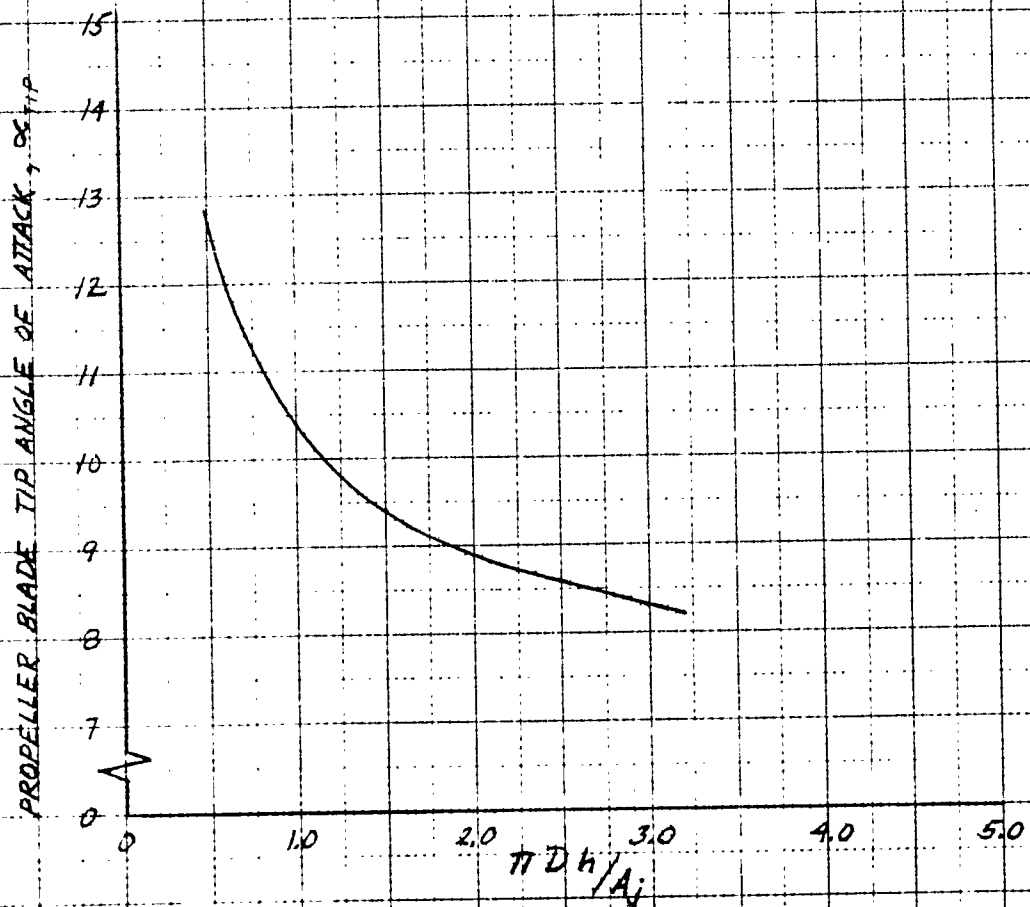


FIGURE 39: PROPELLER BLADE TIP ANGLE OF ATTACK FOR THE CURVED AND STRAIGHT DUCT CONFIGURATIONS

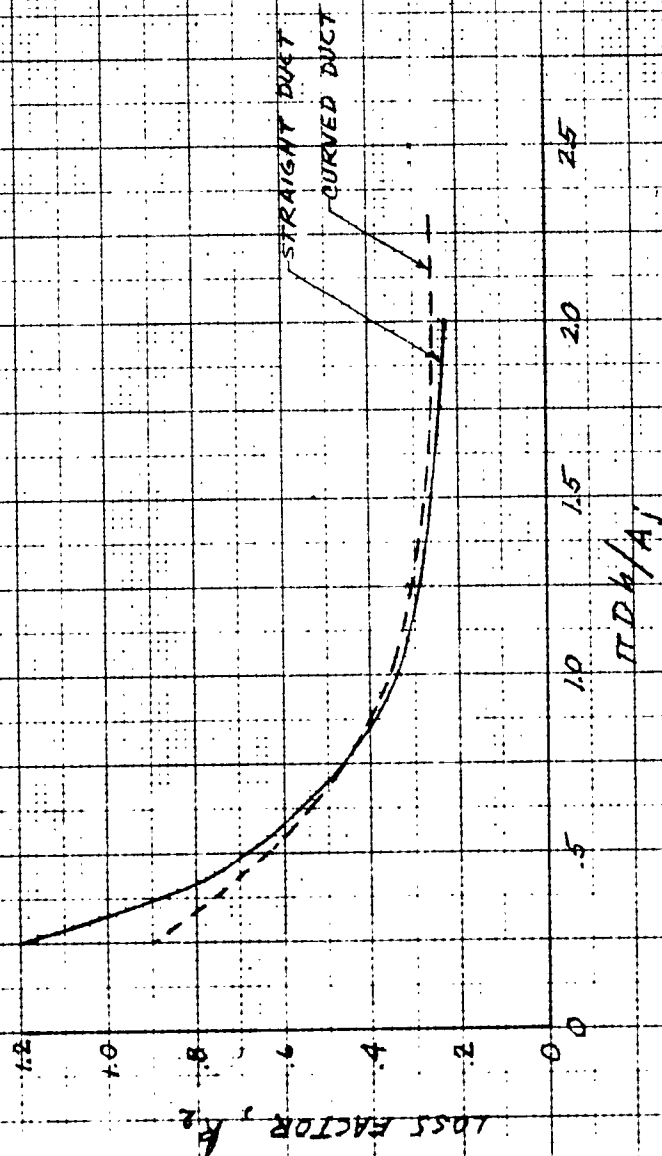


FIGURE 40: LOSS FACTOR, K_2 FOR THE CURVED AND STRAIGHT DUCTS

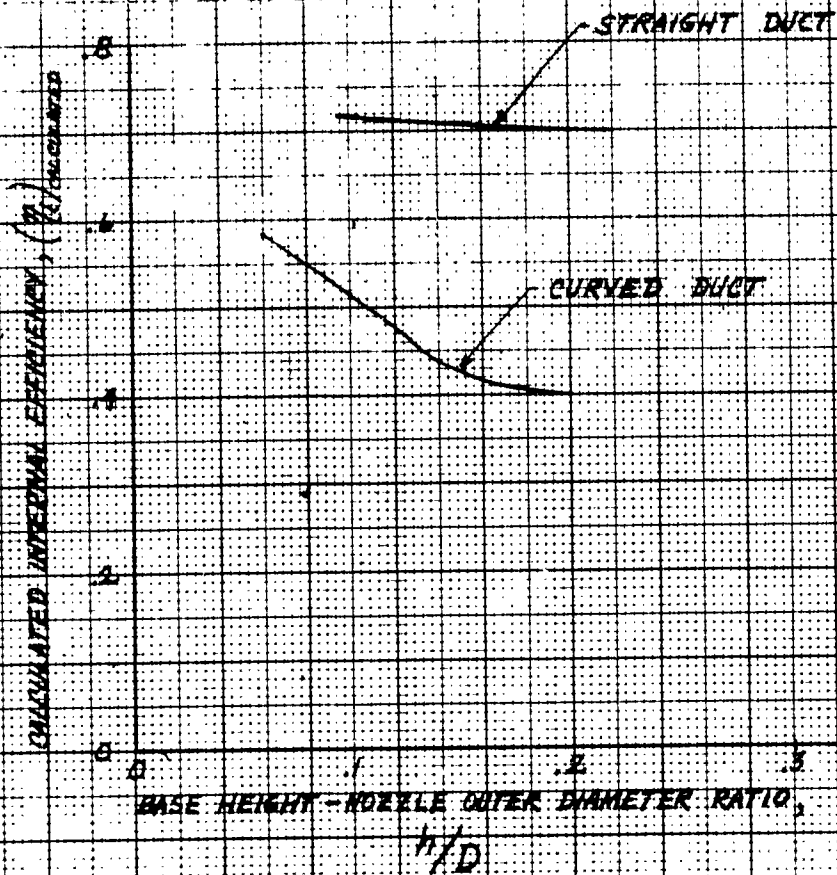


FIGURE 41: CALCULATED INTERNAL EFFICIENCY OF THE CURVED AND STRAIGHT DUCT TEST UNITS BASED ON THEORY OF REFERENCE 6

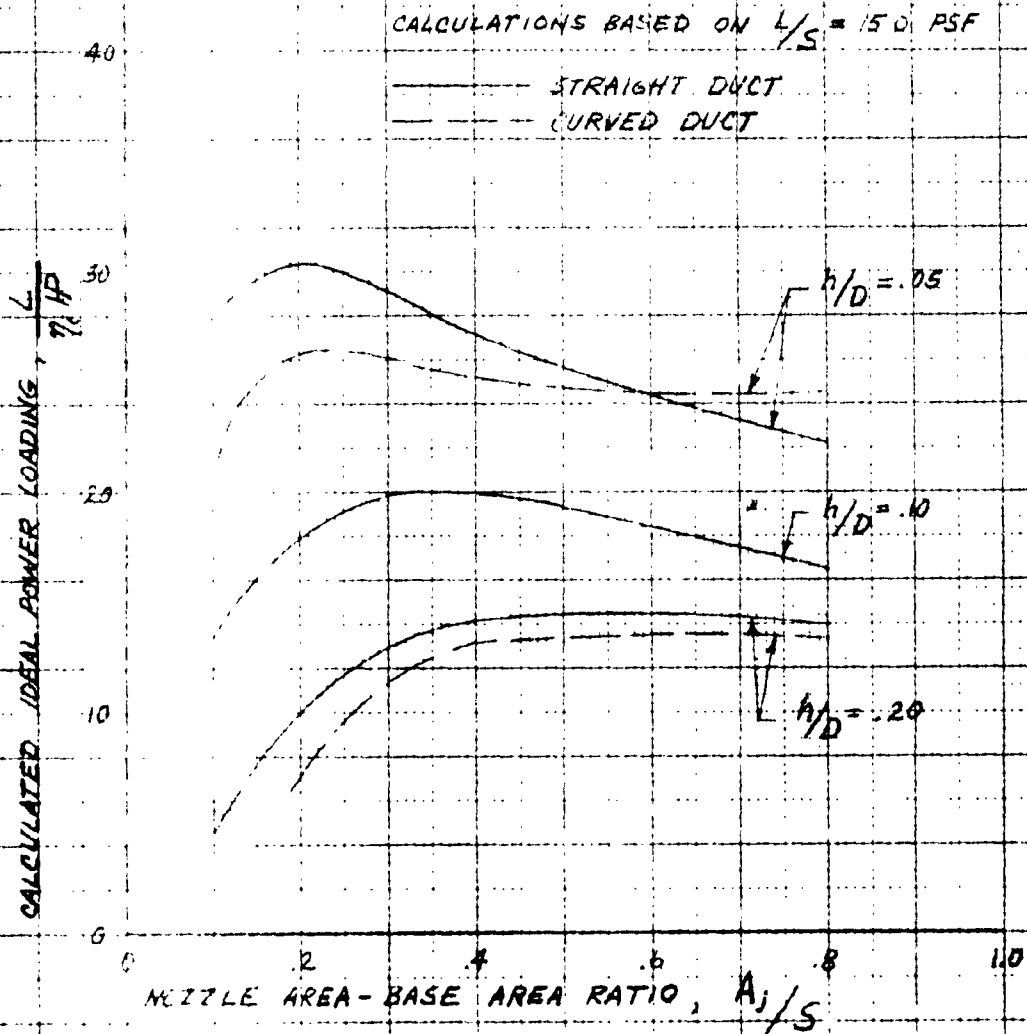


FIGURE 4.2. EXTRAPOLATION OF NOZZLE AND BASE PRESSURE TEST DATA TO SHOW THE EFFECT OF NOZZLE-BASE AREA RATIO ON ANNULAR JET PERFORMANCE.

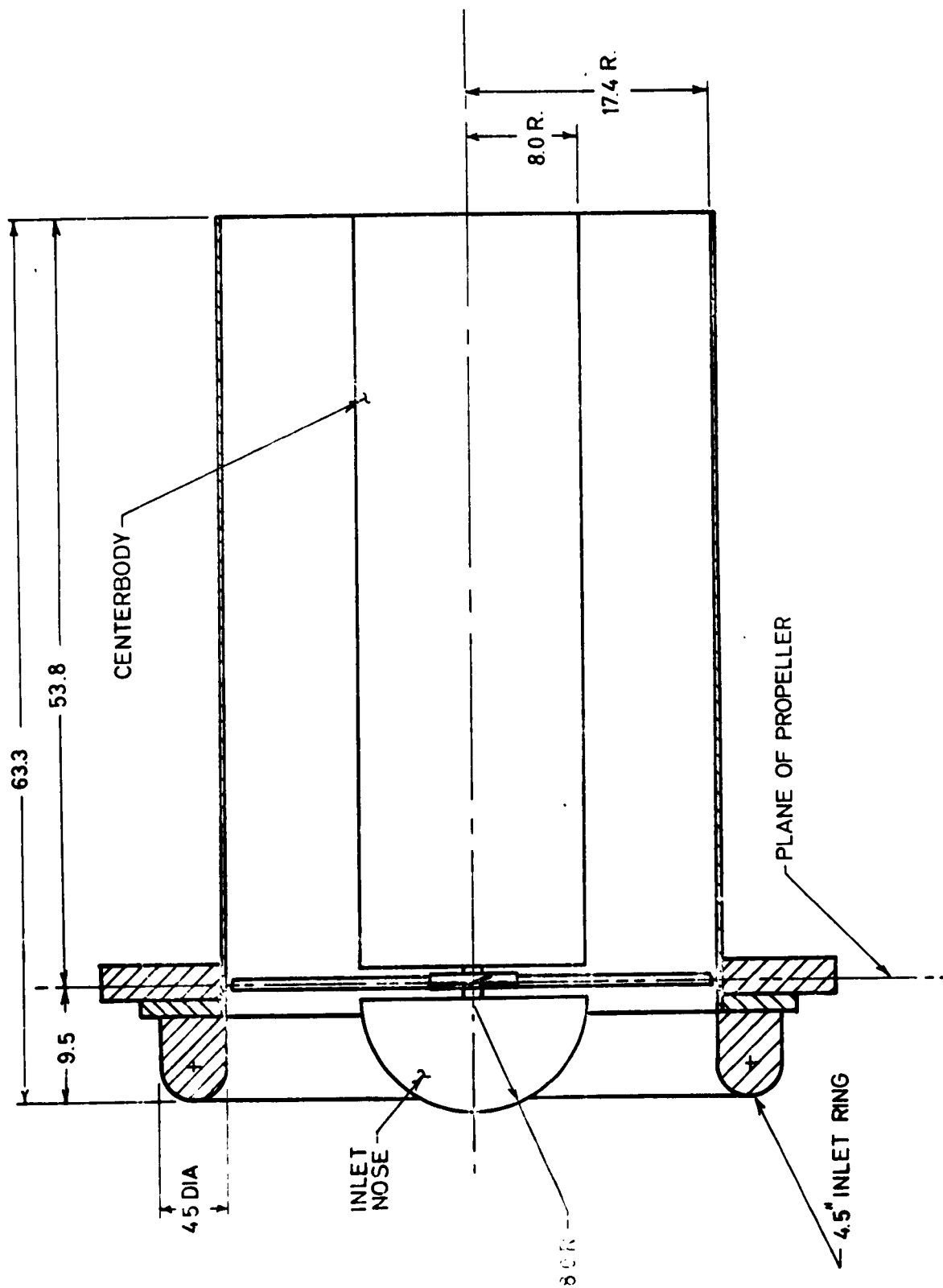


FIGURE 13: PORT STRAIGHT DUCT CONFIGURATION WITH 4.5 INCH DIAMETER INLET RING

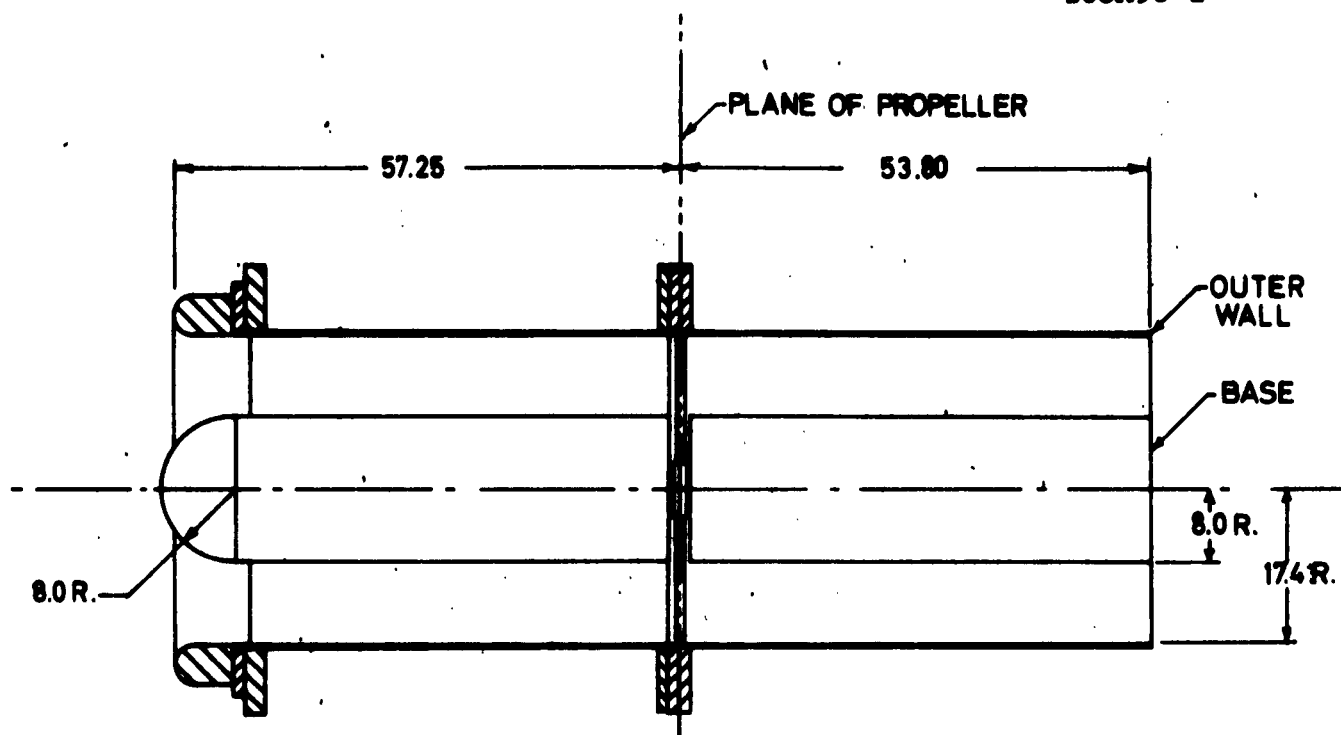


FIGURE 44: SHORT DUCT WITH LONG INLET, 4.5 INCH INLET

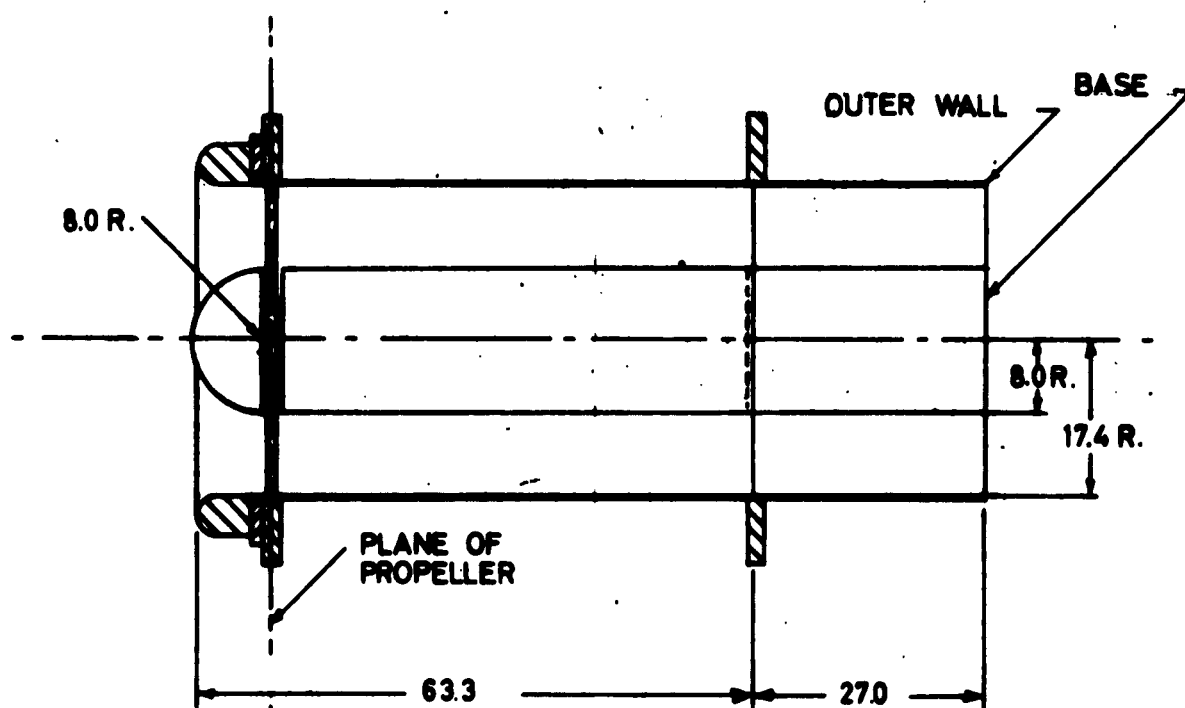
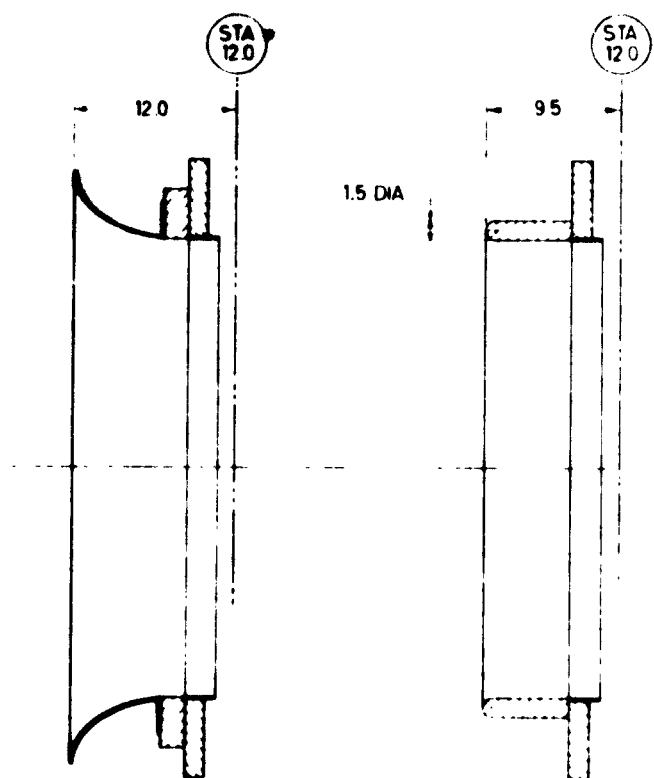


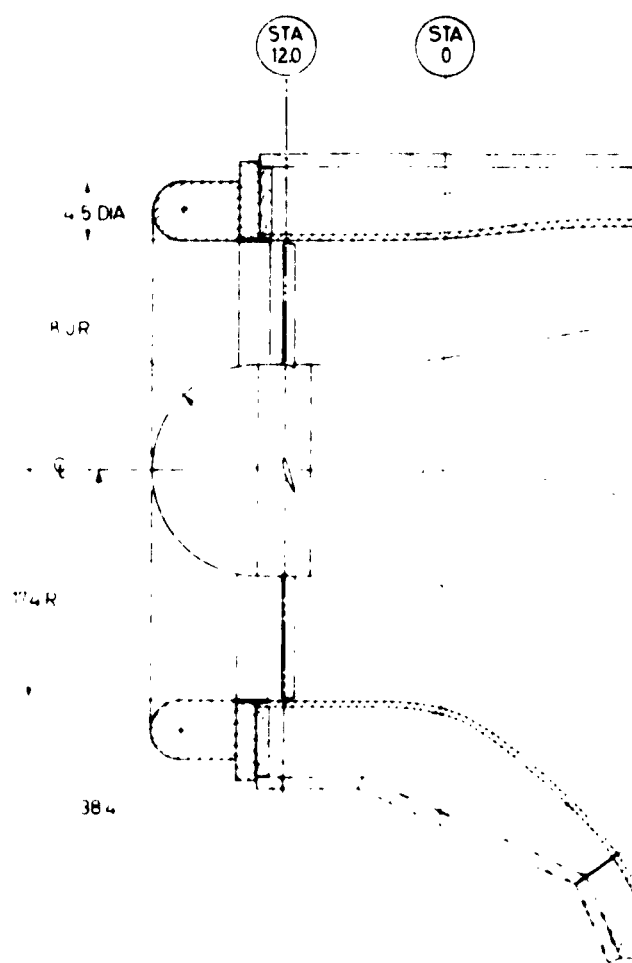
FIGURE 45: SHORT DUCT WITH NOZZLE EXTENSION DUCT, 4.5 INCH INLET RING



QUARTER ELLIPTIC
INLET RING

15 INCH INLET
RING

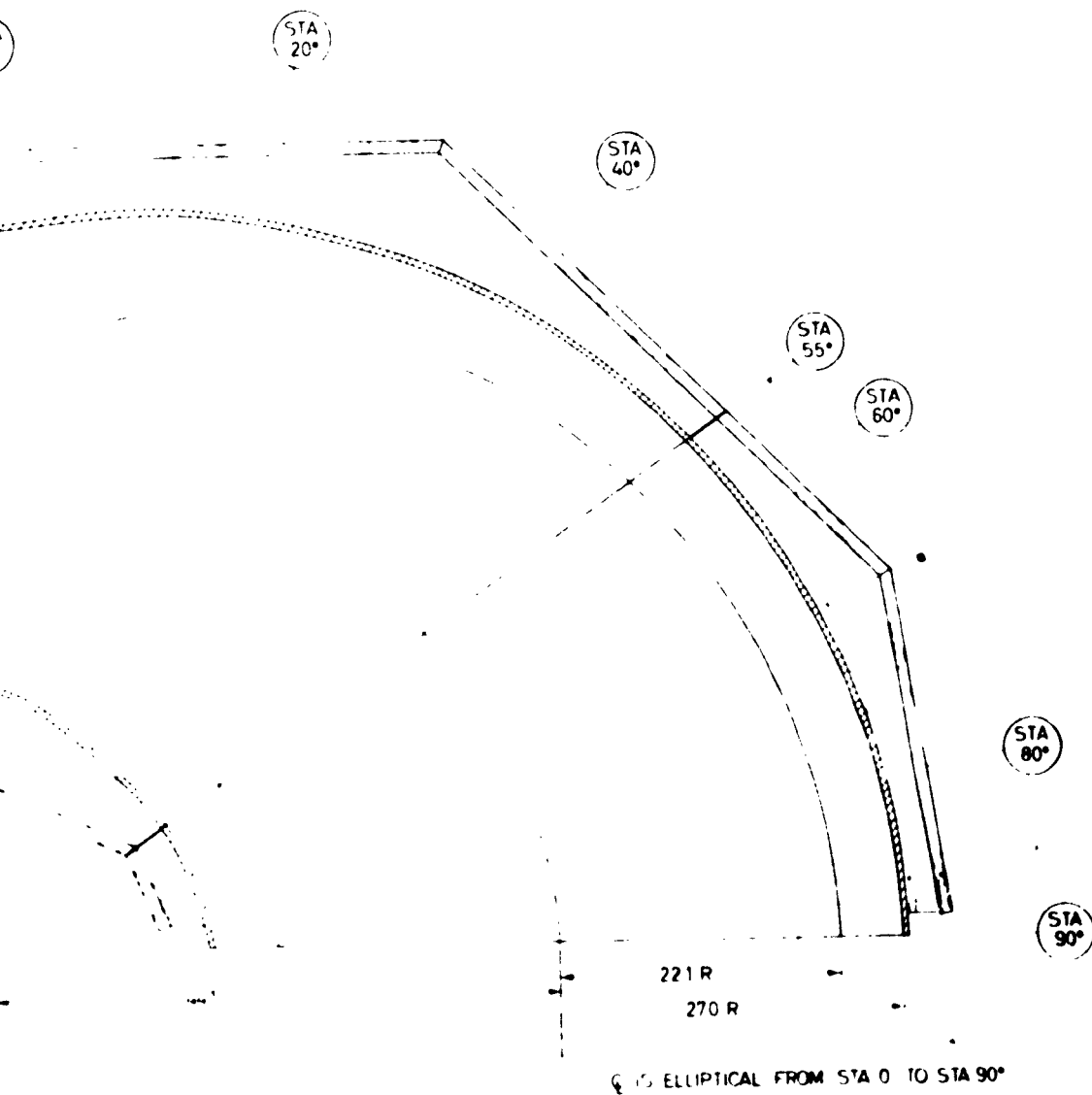
NOTE ALL DIMENSIONS ARE IN INCHES



CURVED D
INLE

FIGURE 46

CURVED DUCT AND IN



2

CURVED DUCT WITH 45 INCH
INLET RING INSTALLED

ED DUCT AND INLET RING GEOMETRY

KELLETT AIRCRAFT CORP
WILLOW GROVE, PA





FIGURE 4-3 SHORT STRAIGHT DUCT WITH 4.5 INCH INLET RING



FIGURE 10 SHORT STRAIGHT DUCT WITH QUARTER ELLIPTIC JET RING

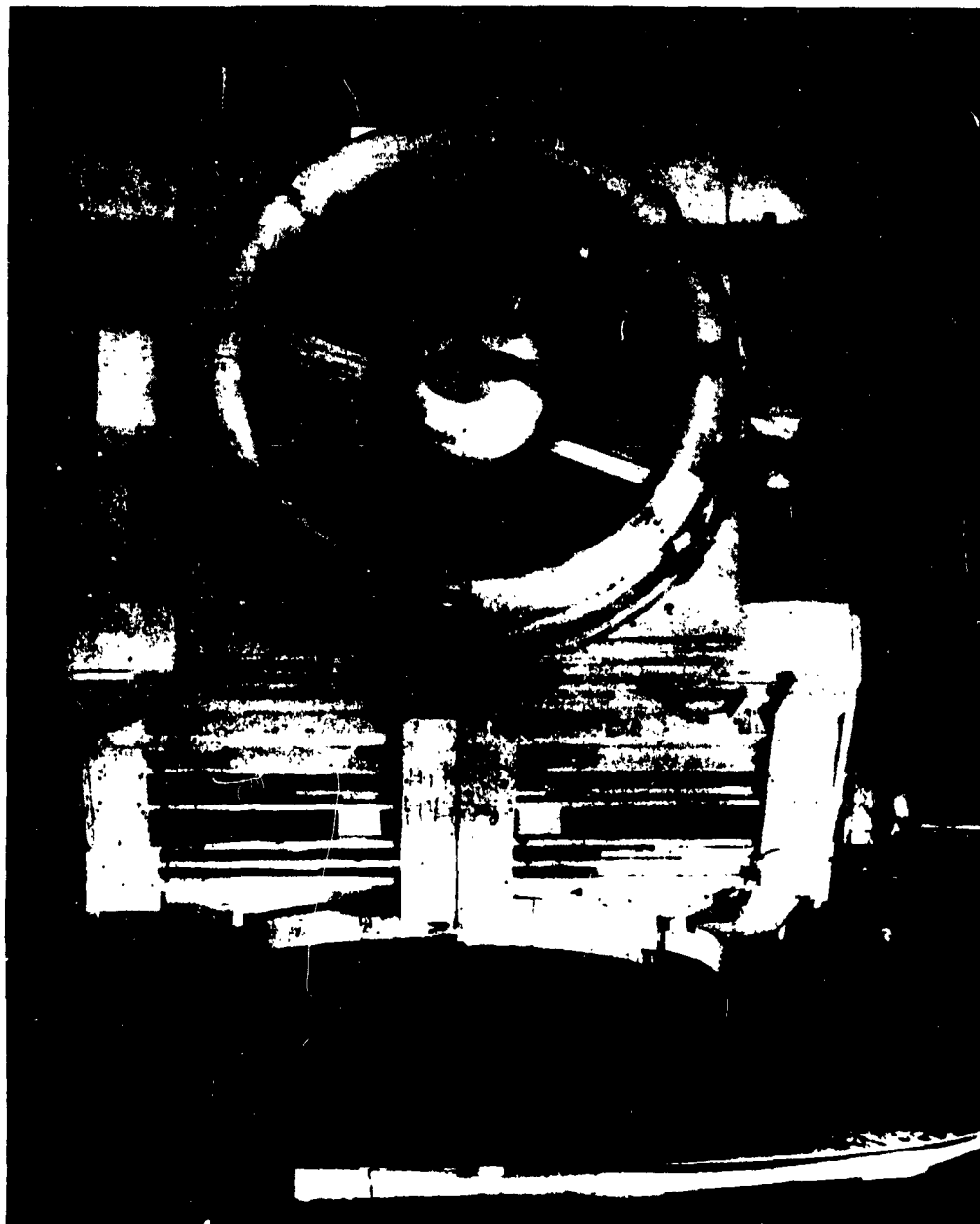
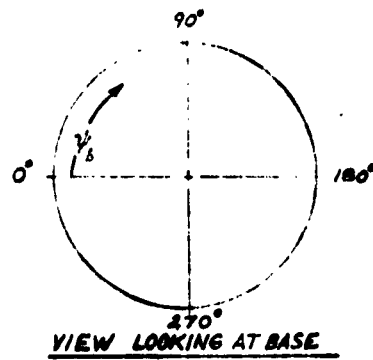
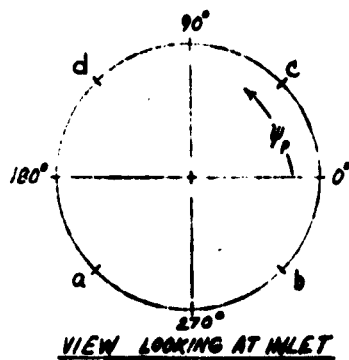
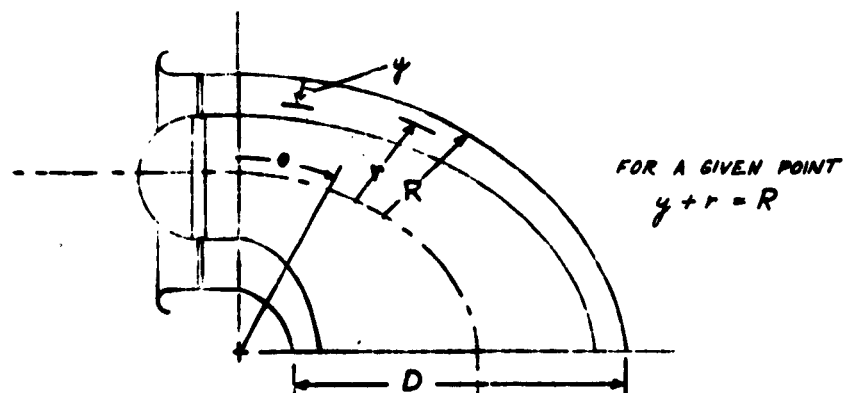


FIGURE 50: CURVED DUCT WITH 4.5 INCH INLET RING

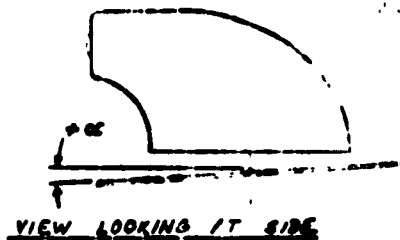


AZIMUTH ANGLES

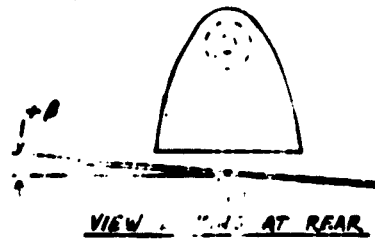


DUCT CURVATURE ANGLE θ , AND RADIAL DISTANCES r , ψ , AND R

α IS ANGLE OF PITCH



β IS ANGLE OF ROLL



GROUND BOARD INCLINATION

FIGURE 51: DEFINITION OF CURVED DUCT GEOMETRIC PARAMETERS



FIGURE 32: CURVED DUCT WITH GUIDE VANE INSTALLED

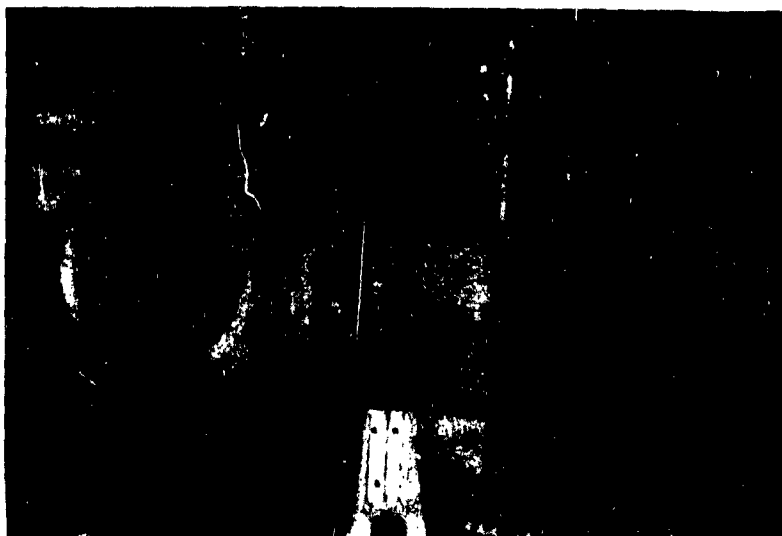


FIGURE 53: CURVED DUCT WITH PLENUM
CHAMBER (INLET VIEW)

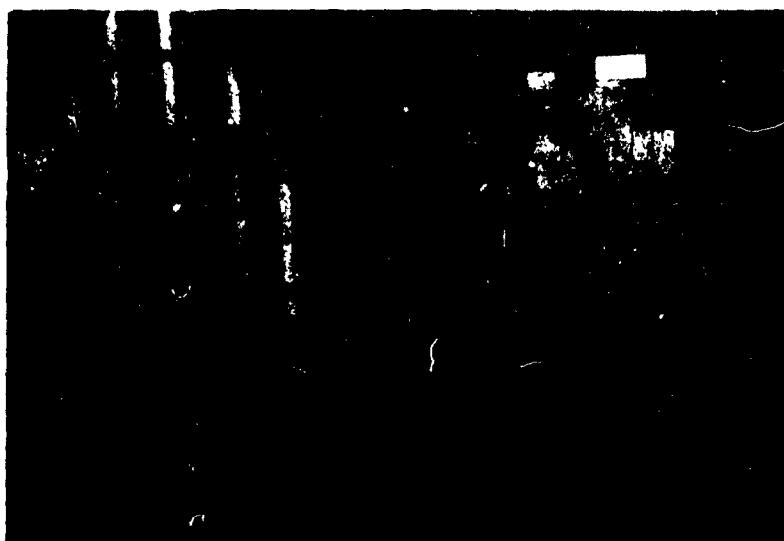


FIGURE 54: CURVED DUCT WITH PLENUM
CHAMBER AND GROUND BOARD
(BASE VIEW)

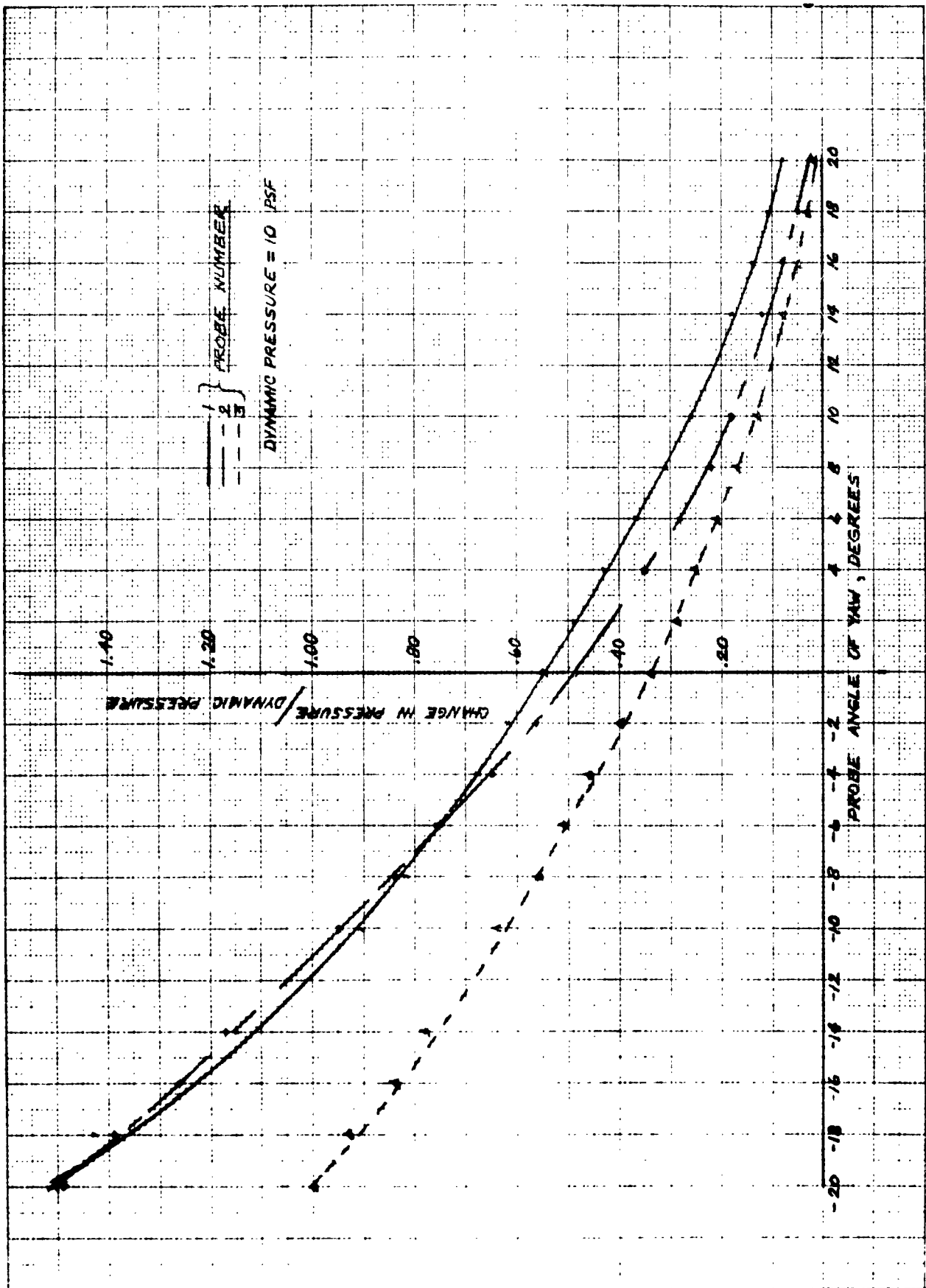


FIGURE 55: PROBE RAKE CALIBRATION WITH ANGLE OF YAW FOR 6 TUBE RAKE

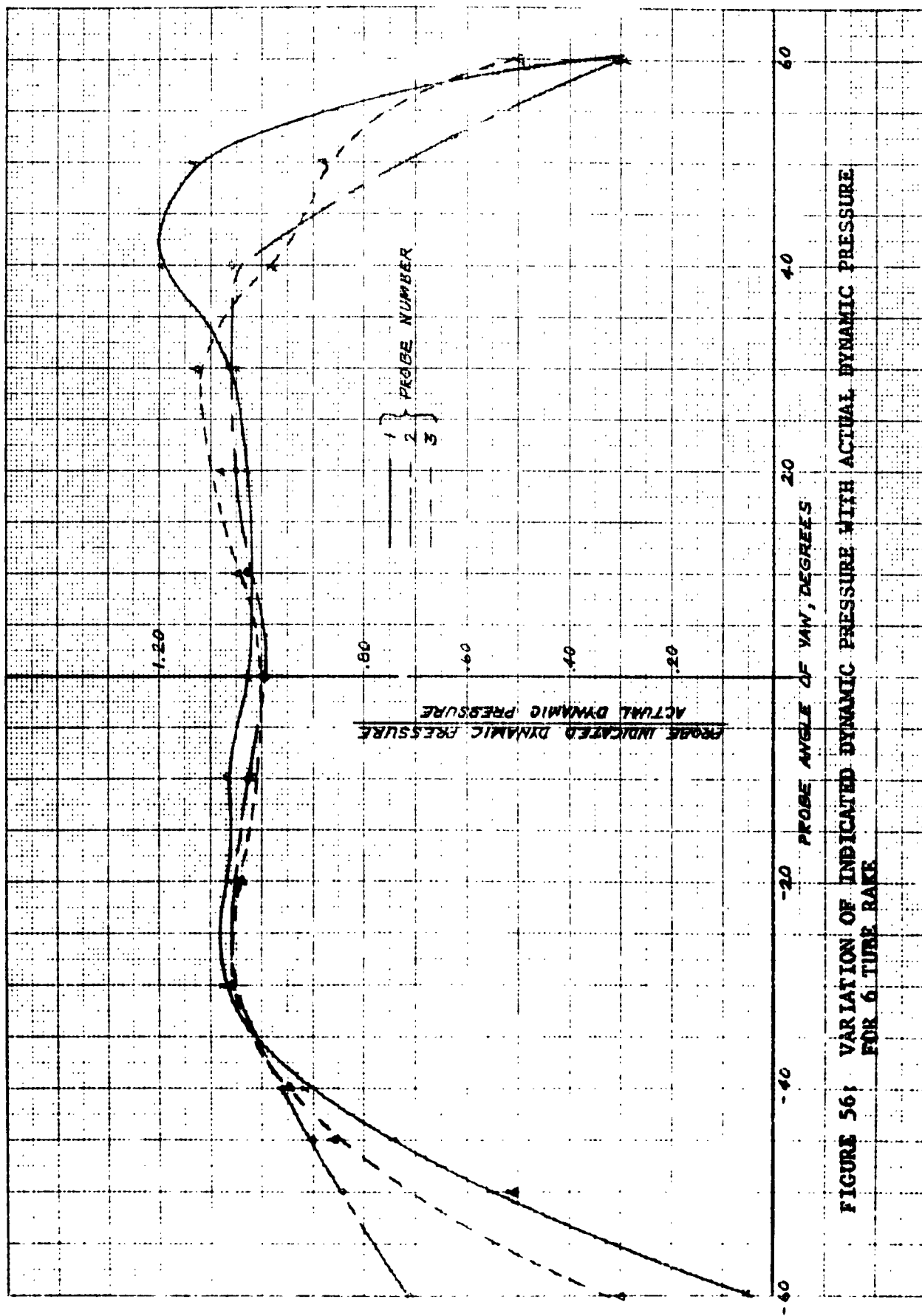


FIGURE 56: VARIATION OF INDICATED DYNAMIC PRESSURE WITH ACTUAL DYNAMIC PRESSURE FOR 6 TUBE RAKE

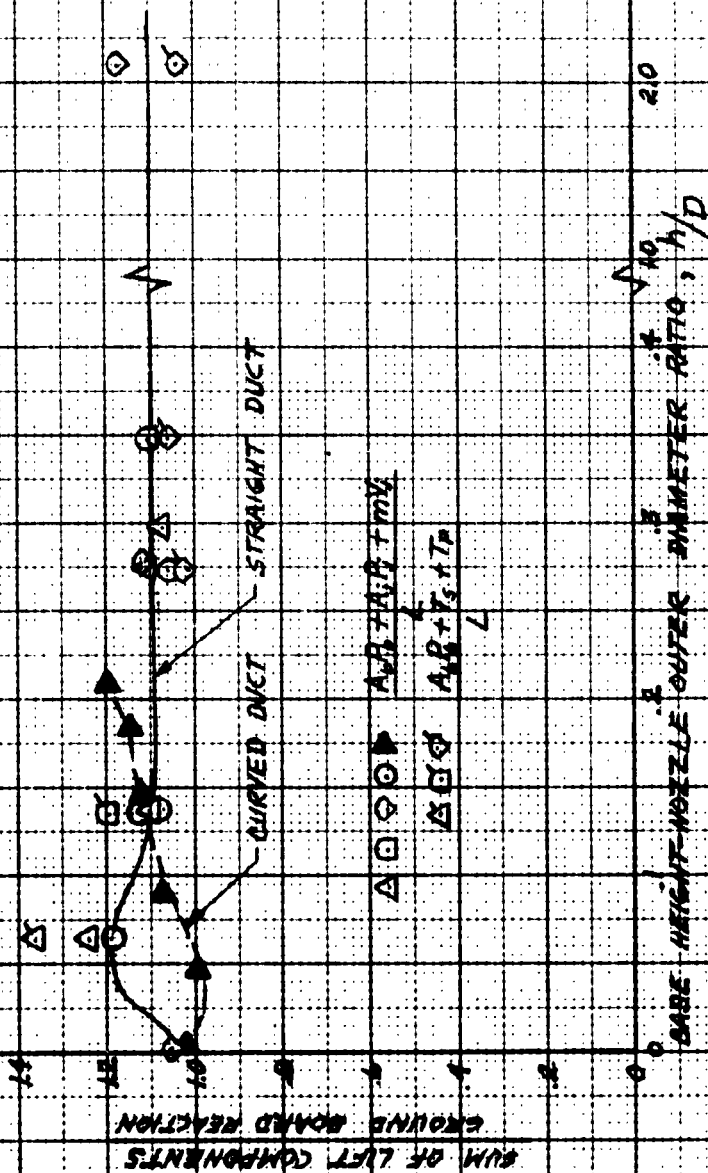


FIGURE 57: COMPARISON OF SUMMATION OF INDIVIDUAL THRUSTS WITH TOTAL FORCE VS. FOR THE CURVED AND STRAIGHT DUCT CONFIGURATIONS.

UNCLASSIFIED

UNCLASSIFIED